Detection of Quercetin using Polymer Coated Quartz Crystal Microbalance and the Modification of á-Zirconium Phosphate to Develop a Sorbent for Organic Pollutant Removal

Darlington Mlambo
Marquette University

DETECTION OF QUERCETIN USING POLYMER COATED QUARTZ CRYSTAL MICROBALANCE AND THE MODIFICATION OF α-ZIRCONIUM PHOSPHATE TO DEVELOP A SORBENT FOR ORGANIC POLLUTANT REMOVAL

by

Darlington Mlambo, BS, MS

A Dissertation Submitted to the Faculty of the Graduate School,
Marquette University,
in Partial Fulfillment of the Requirements for
the Degree of Doctor of Philosophy

Milwaukee, Wisconsin

December 2010

ABSTRACT

DETECTION OF QUERCETIN USING POLYMER COATED QUARTZ CRYSTAL MICROBALANCE AND THE MODIFICATION OF α-ZIRCONIUM PHOSPHATE TO DEVELOP A SORBENT FOR ORGANIC POLLUTANT REMOVAL

Darlington Mlambo

Marquette University, 2010

Sorption processes involve physical and chemical interactions of sorbents with analytes. These may involve the physical and/or chemical processes in which a substance is accumulated at an interface between two phases, or the intermixing of a substance with the matrix of a second phase. The two processes are referred to as adsorption and absorption respectively. The sorption capacities of different classes of sorbents have many potential and demonstrated applications such as sensor development, water treatment, environmental remediation and chromatographic separations.

The goal of this work is to explore the sorption capacity of polymers as well as nanodimensional layered materials for use in developing chemical sensors and materials that can be used for removing pollutants from aqueous solution. Chapter 1 gives a general introduction of polymeric and layered nanodimensional sorbents as well as providing a literature review of the applications of the two types of sorbents utilized in this study. Emphasis is put on the use of polymers to develop coatings for quartz crystal microbalances as well as layered zirconium phosphate for developing sorbents for organic pollutant removal. In Chapter 2, a brief summary of the analytical techniques used in this study, as well as preparation methods for the sorbents, is presented. Chapter 3 presents an investigation of the potential use of polyepichlorohydrin (PECH), polyisobutylene (PIB) and polycaprolactone (PCL) as sorbents for adsorbing quercetin to develop coatings for detecting quercetin using a quartz crystal microbalance sensor (QCM). BisphenolA-hexamethyltrisiloxane (BPA-HMTS) was synthesized and found to increase the sensitivity of QCM sensor for quercetin compared to the other polymers. The sensitivity of the different polymers is evaluated using diffusion coefficients as well as sensor response times.

The modification of layered zirconium phosphate using a tertiary amine in order to make the layered material hydrophobic is presented in Chapter 4. A detailed analytical and spectroscopic characterization of the compound is presented. Chapter 5 presents the application of organically modified layered zirconium phosphate as a sorbent for 4-chlorophenol. The efficacy of the sorbent is evaluated using adsorption isotherms and sorption kinetics models. The proposed future studies are described in Chapter 6

ACKNOWLEDGEMENTS

Darlington Mlambo

My sincere gratitude goes to my research and academic advisor, Prof. Jeanne M. Hossenlopp for her unwavering support throughout this research project. Her scientific guidance and patience is greatly appreciated. I would also like to thank Prof. Chieu Tran and Prof. Scott Reid for affording time out of their schedules to serve on my research committee. I am also thankful to the National Science Foundation and the US Department of Agriculture for providing the financial support for this work, Dr. Frank Holger Foersterling for help with solid state NMR experiments, Dr.Zhu for help with TEM experiments. I would also like to thank Arnold Mensah-Brown for help with sensor experiments. I am grateful to have a loving family constantly showering encouragements. My dearest Sheilah, you are a pillar of support.

Dedication

This work is dedicated to my parents, Samuel and Jessica Mlambo

TABLE OF CONTENTS

ACKNOWLEDGEMENTS i
LIST OF TABLES vi
LIST OF FIGURES vi
1 INTRODUCTION 1
1.1 Sorptive Polymeric Materials for Chemical Sensors 2
1.2 Acoustic wave sensors 6
1.2.1 Acoustic wave propagation modes 7
1.2.2 Bulk wave sensors 8
1.2.3 Selection of polymer coatings for acoustic wave sensors 9
1.2.4 Attenuated total reflectance Fourier transform infrared spectroscopy 11
1.3 Sorbents for water and wastewater treatment 13
1.3.1 Layered zirconium phosphate 15
1.4 Motivation of the study 17
2 EXPERIMENTAL METHODS 19
2.1 Attenuated total reflectance Fourier transform spectroscopy 19
2.2 Quartz crystal microbalance (QCM) 21
2.3 X-ray diffraction 23
2.4 Thermogravimetric Analysis (TGA) 24
2.5 Transmission Electron Microscopy (TEM) 24
2.6 UV-Visible spectroscopy 25
2.7 Nuclear Magnetic Resonance (NMR) spectroscopy 25
2.8 Preparation of Materials 26
2.8.1 Polymer films and analyte preparation 26
2.8.2 Preparation of α zirconium phosphate 28
3 DETECTION OF QUERCETIN USING A POLYMER COATED QUARTZ CRYSTAL MICROBALANCE 30
3.1 Introduction 30
3.1.1 Beneficial health effects of quercetin 32
3.1.2 Analytical Methods for detecting quercetin 33
3.2 Experimental 34

3.2.1 Time resolved ATR-FTIR 35
3.2.2 Quartz crystal microbalance 35
3.3 Results and Discussion 36
3.3.1 Characterization of the Infrared bands of quercetin 36
3.3.2 ATR-FTIR spectra of quercetin-ethanol solution. 39
3.3.3 Interaction of quercetin solution with polymer films 42
3.3.4 Diffusion of quercetin in polymer films 43
3.3.5 Estimation of Diffusion coefficients 50
3.3.6 Detection of quercetin using PECH and PIB coated QCM sensors 56
3.4 Conclusions 68
4 SYNTHESIS AND CHARACTERIZATION OF TERTIARY AMINE INTERCALATED A-ZIRCONIUM PHOSPHATE 70
Introduction 70
4.1.1 Intercalation of alkylamines in α-zirconium phosphate 70
4.2 Experimental 73
4.2.1 Materials 73
4.2.2 Analytical Techniques 73
4.3 Results and Discussion 74
4.3.1 X-ray diffraction analysis of Intercalation of tertiary amines in α-ZrP 74
4.3.2 Spectroscopic characterization of alkylamine intercalation 82
4.3.3 Transmission Electron Microscopy 87
4.3.4 Thermogravimetric Analysis of zirconium phosphate and intercalation products. 89
4.4 Conclusions 95
5 ADSORPTION OF 4-CHLOROPHENOL BY DIMETHYL-HEXADECYLAMINE MODIFIED LAYERED A-ZIRCONIUM PHOSPHATE 96
5.1 Introduction 96
5.2 Experimental 98
5.2.1 Materials 98
5.2.2 Sorption Isotherms and Kinetics 98
5.2.3 Analytical Techniques 99
5.3 Results and Discussion 100
5.3.1 Powder X-Ray Diffraction Analysis 100
5.3.2 Adsorption Kinetics 101

5.3.3 Adsorption Isotherms 112
5.3.4 XRD analysis 121
5.3.5 ATR-FTIR analysis 130
5.3.6 Regeneration of ZrP-DHDA 131
5.3.7 Conclusions 132
6 PROPOSED FUTURE WORK 133
6.1 Chemical Sensor Development 133
6.2 Intercalation of chlorophenol in ZrP-DHDA 134
6.3 Prospects and Challenges for ZrP-DHDA application 134
REFERNCES 141
APPENDICES 150
APPENDIX A 150
APPENDIX B 151
APPENDIX C 156

LIST OF TABLES

Table 2.1. Characteristics of the ZnSe horizontal ATR crystal used for diffusion experiments 19
Table 3.1 Infrared absorption band assignments 39
Table 3.2 Summary of the bands that show red-shifting as a result of dissolving quercetin in ethanol 41
Table 3.3 Parameters for the exponential fit for the diffusion of quercetin in PECH 47
Table 3.4 Parameters for the exponential fit for the diffusion of quercetin in PCL 48
Table 3.5 Parameters for the exponential fit for the diffusion of quercetin in PIB 50
Table 3.6 Estimated equilibrium absorbance and n values for Fickian diffusion 51
Table 3.7 calculated diffusion coefficients of quercetin solution in the polymer films used in this study 53
Table 3.8 LSER regression coefficients for PECH and PIB at 25°C 54
Table 3.9 Calculated diffusion coefficients of ethanol in the polymer films 55
Table.3.10 Time constants for sorption of quercetin onto PECH coated QCM devices 60
Table 3.11 Time constants for sorption of quercetin onto PIB coated QCM sensor 61
Table 4.1 Calculated alkylamine sizes and proposed interlayer arrangement of alkylamines in ZrP interlayer spaces 77
Table 5.1 Kinetic and statistical parameters of the pseudo-first order kinetic model 105
Table 5.2 Kinetic and statistical parameters of the pseudo-second order kinetic model 106
Table 5.3 Kinetic and statistical parameters of the modified multiplex model 107
Table 5.4 Kinetic and statistical parameters of the double exponential model 108
Table 5.5 Kinetic and statistical parameters of the pseudo-second order kinetic model for concentration dependent experiment 112
Table 5.6 BET parameters for the adsorption of 4-chlorophenol onto ZrP-DHDA at various temperatures 119

LIST OF FIGURES

Figure 1.1 Hydrosilation polymerization reaction 5
Figure 1.2 Thickness shear mode resonator 8
Figure 1.3 Schematic representation of total internal reflection. 11
Figure 1.4 Schematic representation of α-ZrP. 15
Figure 2.1 FTIR spectroscopy experimental set up 20
Figure 2.2. A complete QCM 200 set up. 21
Figure 2.3 Chemical Structures of the commercial polymers used in this study 26
Figure 2.4 Chemical structures of the monomers used to synthesize BPA-HMTS 27
Figure 3.1 Chemical structures of major flavonoids 30
Figure 3.2 Chemical structures of quercetin showing the numbering of its carbon atoms 31
Figure 3.3 Infrared absorption spectrum of quercetin powder. 37

Figure 3.4 Fingerprint region (1800-940 cm^{-1}) of the IR absorption spectrum of quercetin 38
Figure 3.5 ATR-FTIR spectrum of ethanol 40
Figure 3.6 Infrared spectra of quercetin in PCL (a) PECH (b) PIB (c). 42
Figure 3.7 Temporal changes of the ATR-FTIR spectra of quercetin-ethanol solution in PECH . 44
Figure 3.8 Temporal changes of the ATR-FTIR spectra of quercetin-ethanol solution in PECH 45
Figure 3.9 Temporal changes of the 1608 cm^{-1} band of quercetin solution in PECH..... 46
Figur 3.10 Temporal changes of the 1608 cm^{-1} absorption band of quercetin solution in PCL 48
Figure 3.11 Temporal changes of the intensity of the 1601 cm^{-1} quercetin peak 49
Figure 3.12 Linear plots of equation 5 for the diffusion of quercetin in a) PCL, b)PECH c) PIB. 52
Figure 3.13 Measured Frequency shifts in the detection of 76 ppm to 304 ppm quercetin..... 57
Figure 3.14 Measured resistance shifts in the detection of 75 ppm to 304 ppm quercetin 58
Figure 3.15 Resistance and Frequency shifts (insert) of a PIB coated QCM..... 59
Figure 3.16 Resistance shifts as a function of concentration 63
Figure 3.17. Measured frequency shifts in the detection of 5 ppm - 30 ppm quercetin 64
Figure 3.18 Measured frequency shift in the detection of 5 ppm -30 ppm quercetin 65
Figure 3.19 Measured frequency shifts in the detection of 15 ppm 66
Figure 3.20 Measured frequency shifts in the detection of 5 - 30 ppm quercetin..... 67
Figure 3.21 Frequency shifts versus quercetin concentrations 68
Figure 4.1 chemical structures of amines used in this study..... 72
Figure 4.2 Powder X-ray diffraction patterns of ZrP (a), ZrP-BA (b) ZrP-Octyl (c) ZrP-DtDA (d) ZrP-DHDA (e) ZrP-HDA (f). 75
Figure 4.3 Planar view of a methyl group..... 78
Figure 4.4 Schematic representation of ZrP-DHDA..... 79
Figure 4.5 Schematic representation of ZrP-BA..... 80
Figure 4.6 X-ray diffraction patterns for the intercalation of DHDA in ZrP..... 82
Figure 4.7 ATR FTIR spectra of ZrP (a) DHDA (b) ZrP-DHDA (c). 83
Figure 4.8 ATR-FTIR spectrum of ZrP (a) Butylamine (b) ZrP-BA (c). 84
Figure 4.9 ^{31}P solid state NMR spectrum of ZrP (a) and ZrP-DHDA (b)..... 85
Figure 4.10 ^{31}P solid state NMR spectrum of ZrP (a) and ZrP-BA (b)..... 86
Figure 4.11 TEM images of ZrP at a resolution of 200 nm (a) and 50 nm (b) 88
Figure 4.12 TEM images of ZrP-DHDA at a resolution of 100 nm (a) 20 nm (b)..... 89
Figure 4.13 Thermogravimetric analysis curves..... 90
Figure 4.14 X-ray diffraction pattern of the final product of thermal degradation of ZrP..... 91
Figure 4.15 TGA-DTG-FTIR for the degradation of ZrP..... 92
Figure 4.16 TGA-DTG curves for ZrP-DHDA 93
Figure 5.1 Powder X-ray diffraction pattern of α-ZrP (a) ZrP-DHDA (b). 101
Figure 5.2 Amount of chlorophenol adsorbed by 0.1 g of ZrP-DHDA as a function of time 104
Figure 5.3 Amount of chlorophenol adsorbed by 0.1 g of ZrP-DHDA as a function of time 106
Figure 5.4 Amount of chlorophenol adsorbed by 0.1 g of ZrP-DHDA as a function of time 107
Figure 5.5 Amount of chlorophenol adsorbed by 0.1 g of ZrP-DHDA as a function of time 108
Figure 5.6 Amount of 4-chlorophenol adsorbed by 0.1 g of ZrP-DHDA as a function of time . 110
Figure 5.7 Amount of 4-chlorophenol adsorbed by 0.1 g of ZrP-DHDA in 30 ml of solution ... 111

Figure 5.8 Equilibrium Sorption isotherms for 4-chlorophenol onto Zirconium phosphate 113
Figure 5.9 Adsorption isotherm for chlorophenol onto ZrP at 26 ^{0}C. Initial concentrations of chlorophenol ranged from 0 to 800 mg/L 116
Figure 5.10 S-type adsorption isotherms for 4-chlorophenol onto ZrP-DHDA at different temperatures. 118
Figure 5.11 Adsorption of 4-chlorophenol onto ZrP-DHDA in the 0 to 2000 mg/L chlorophenol concentrations.. 120
Figure 5.12 XRD patterns of the phases obtained after adsorption of 4-chlorophenol 121
Figure 5.13 X-ray diffraction patterns for ZrP-DHDA 123
Figure 5.14 X-ray diffraction patterns for ZrP-BA 124
Figure 5.15 Powder XRD patterns for different isomers of chlorophenol. 125
Figure 5.16 Adsorption kinetics of 3 isomers of chlorophenol by ZrP. 127
Figure 5.17 powder XRD patterns for ZrP-DHDA 129
Figure 5.18 ATR-FTIR spectra of phases obtained after adsorption of 4-chlorophenol. 130
Figure 5.19 XRD patterns of ZrP-DHDA intercalated with 4-chlorophenol 131
Figure 6.1 X-ray diffraction pattern of a film of ZrP deposited on a glass slide 136
Figure 6.2 X-ray diffraction pattern of ZrP-BA powder (a) film (b) deposited on a glass slide 137
Figure 6.3 X-ray diffraction pattern of ZrP film (a)and ZrP-PEI (b) deposited on a glass slide 138
Figure 6.4 Tapping mode AFM image of ZrP-PEI film (a) and height profile of the film (b) 139
Figure 8.1 Experimental (blue) and calculated (black sticks) spectrum of quercetin. 154
Figure 8.2 Amount of 4-chlorophenol adsorbed by 0.1 g of ZrP-DHDA as afunction of time 159
Figure 8.3 Amount of 4-chlorophenol adsorbed by 0.1 g of ZrP-DHDA as a function of time .. 160
Figure 8.4 Amount of 4-chlorophenol adsorbed by 0.1 g of ZrP-DHDA as a function of time .. 160
Figure 8.5 Amount of 4-chlorophenol adsorbed by 0.1 g of ZrP-DHDA as a function of time .. 161

1 INTRODUCTION

The sorption of analytes by two types of sorbents has been studied in this work. The first type utilizes the sorptive capacity of polymers to absorb and concentrate an analyte within their matrix. This property of polymers has been utilized to develop partially selective coatings for surface acoustic wave chemical sensors.[1,2] Polymer coatings for surface acoustic wave devices increase the sensitivity and selectivity of these devices for chosen analytes by concentrating the analytes on the device surface.[3] The potential of polyepichlorohydrin (PECH), polyisobutylene (PIB) and polycaprolactone (PCL) to adsorb and concentrate quercetin within their matrix was studied in order to use these polymers as coatings for a quartz crystal microbalance sensor that can be used for detecting quercetin. PECH and PIB have been used as polymer coatings on shear horizontal surface acoustic wave (SH-SAW) devices.[4]

The second class of sorbent utilizes the sorptive capacity of layered nanodimensional zirconium phosphate for adsorbing organic pollutants from aqueous solution. Layered inorganic materials have been extensively applied as sorbents for anionic pollutants,[5,6] heavy metals[7] and organic pollutants[8] from aqueous solution. In most of these studied the removal of the pollutants involves both adsorption and absorption processes. Adsorption is the physical or chemical process in which a substance is accumulated at an interface between two phases, while absorption involves the intermixing of a substance with the matrix of a second phase.[9] The substance being removed from one phase is the sorbates, while sorbent refers to the phase onto or into which the accumulation occurs.[10] In physical adsorption the forces of attraction between

the sorbent and the sorbates are generally weak van der Waals forces. The extent of physical adsorption is smaller at higher temperatures.[11,12] Equilibrium in physical adsorption is generally achieved rapidly and is readily reversible. When adsorption involves the formation of chemical bonds, the process is referred to as chemisorption.[13] Chemisorption may result in strong bonds such that the process may not be reversible. Since chemisorption involves the formation of chemical bonds, it may not occur at low temperatures if the reaction has an activation energy barrier. Chemisorption is therefore typically characterized by rates that increase with increasing temperature.[9,13]

1.1 Sorptive Polymeric Materials for Chemical Sensors

The sorbent property of commercial polymers is utilized to develop films that can absorb compounds. These films are used to coat acoustic wave devices for developing sensors. Chemical sensors based on surface acoustic wave transducers have been coated with sorptive polymers to improve sensitivity and selectivity.[3,4,14-17] Sensitivity is determined from the magnitude of the output signal that is produced in response to some concentration of a target analyte, whereas selectivity refers to the ability of the sensor to discriminate between the analyte of interest and other species.[18] While the polymer film collects and concentrates the analyte molecules, the device on which it has been applied transduces the presence of the sorbed molecules into an analytical signal. Other materials such as self-assembled monolayers, dendrimers, lipids and cavitands such as cyclodextrin have also been used as selective layers on acoustic wave sensors.[15,17] The choice of

material depends on the extent to which it enhances the sensitivity and selectivity of the sensors, at the same time affording reversibility and reproducibility.

Polymers are widely used as coatings on acoustic wave devices because they offer many advantages including their low cost, ease of fabrication, and their ability to be spin coated on the sensor devices.[1,18] Other usable characteristics of polymers for sensor development are that chemical properties may be modified by altering specific functional groups[15,19] and their physical properties may also be easily modified to change the selectivity and sensitivity of the sensor.[18] For detection in liquid phases, the polymer coating must be stable in water or the solvent in which the analyte is dissolved. While the chemical properties influence the selectivity, the physical properties influence other aspects of the sensor such as response time.[14] Polymer films that are widely used as coatings for acoustic wave sensors such as quartz crystal microbalance and surface acoustic wave resonators are normally of very low glass transition temperature[20] and are permeable,[21] allowing analytes to be immobilized and concentrated for subsequent detection.[22] The glass transition temperature, Tg, of a polymer is defined as the temperature at which the polymer softens because of the onset of long-range coordinated molecular motion.[23] Below Tg, a polymer will be in its glassy state and tends to be rigid. Above Tg, a polymer exhibits a rubbery elastic state and the polymer chains are able to experience large, reversible deformations. Rapid response in acoustic wave sensors is promoted by polymers with Tg values below the operating temperature of the sensor.[1] The response times of sensors with glassy polymers are typically much slower than those based on rubbery polymers.[14]

Many polymers with low glass transition temperatures are commercially available and have been tested as sensing layers for acoustic wave sensors. Polyepichlorohydrin (PECH), poly(isobutylene) (PIB) and polydimethylsiloxane (PDMS) have been applied on shear horizontal surface acoustic wave sensors for detecting toluene, nitrobenzene and xylenes in water.[4] Siloxane based polymers that have low glass transition temperatures have been used in acoustic wave sensors for gas sensing.[15,24-26] Although commercial polymers such as PECH, PIB and PDMS have good properties for coating acoustic wave devices, it is difficult to combine the desired chemical interactive properties with the necessary physical properties for performance as thin films on sensors. However, an approach based on hydrosilation reaction has been developed for designing and synthesizing sorptive polymers that would afford predictable chemical selectivity and physical properties, while allowing a diversity of materials to be prepared.[27] The hydrosilation reaction adds Si-H bonds across C-C double bonds in the presence of a metal catalyst such as platinum. This reaction is selective for reaction with C-C bonds in the presence of many other functional groups. Fig.1.1 shows the use of hydrosilation reaction to make carbosiloxane polymers.

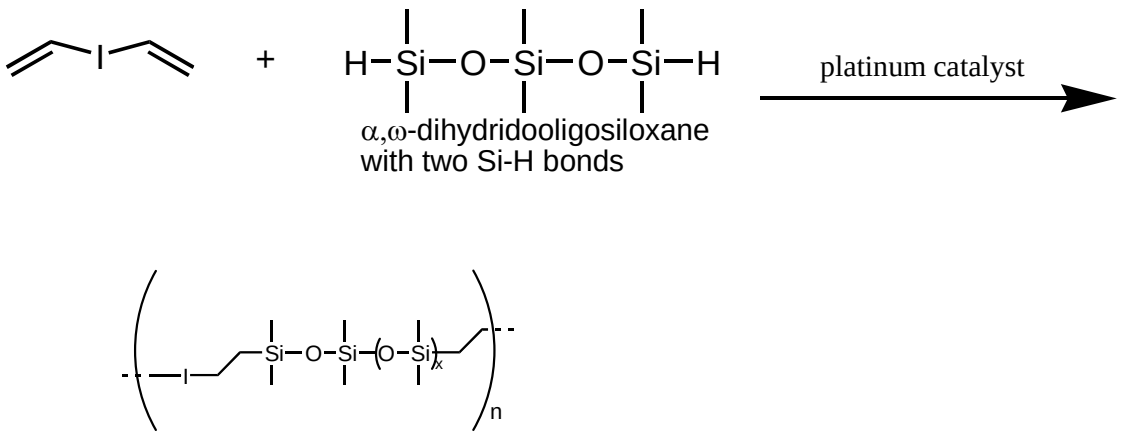

Figure 1.1 Hydrosilation polymerization showing a monomer with two C=C bonds and a second monomer that is an, ω-dihydridooligosiloxane with Si-H on each end. The monomer with two C=C bonds has the interactive (I) properties of choice for chemical selectivity as a sensing material. (This scheme was adapted from reference 27)

The use of oligosiloxane segments in polymers often leads to low glass transition temperatures, as noted previously. This approach also affords the synthesis of diverse polymers with various functional groups, and the resulting polymers should exhibit low glass transition temperature.[28] It has also been reported that another very desirable property of the hydrosilation approach is that the bond forming reaction does not bias the selectivity of the resulting material, since it produces only silicon-carbon bonds without introducing any polar functionalities in the final material.[14]

1.2 Acoustic wave sensors

Acoustic wave sensors utilize a mechanical wave as the sensing mechanism. As the acoustic wave propagates through or on the surface of the material, any changes to the characteristics of the propagation path affect the velocity and/or amplitude of the wave. Changes in velocity can be monitored by measuring the frequency, phase or amplitude characteristics of the sensor and can then be correlated to the corresponding physical quantity that is being measured.

Piezoelectric materials are used to generate acoustic waves for acoustic wave sensors. Piezoelectricity is defined as the production of electrical charges by the application of mechanical stress.[29] There are several piezoelectric substrate materials that may be used for acoustic wave sensors and devices. The most common are quartz (SiO_2) and lithium tantalate ($LiTaO_3$), and to a lesser degree, lithium niobate ($LiNbO_3$).[30] Each material has specific advantages and disadvantages, which include cost, temperature dependence, attenuation, and propagation velocity.[30] A device with higher wave propagation velocity will be more sensitive to perturbation than a device with a lower wave propagation velocity. The temperature dependence of the piezoelectric device will affect its application in environments that have high temperature variations.

1.2.1 Acoustic wave propagation modes

Acoustic wave devices are described by the mode of wave propagation through or on a piezoelectric substrate. Acoustic waves are distinguished primarily by their velocities and displacement directions. The interdigital transducer (IDT) of each sensor provides the electrical field necessary to displace the substrate to form an acoustic wave. The wave propagates through the substrate where, it is converted back to electric field at the other IDT.[30] Transverse, or shear, waves have particle displacements that are normal to the direction of wave propagation and can be polarized so that the particle displacements are parallel or normal to the sensing surface. Shear horizontal wave motion indicates transverse displacements polarized parallel to the sensing surface, whereas shear vertical motion indicates transverse displacements normal to the surface.[31] If the wave propagates through the substrate, the wave is called a bulk wave. The most commonly used bulk acoustic wave (BAW) devices are the thickness shear mode (TSM) resonator and the shear-horizontal acoustic plate mode (SH-APM) sensor.[30] If the wave propagates on the surface of the substrate, it is known as a surface wave. The most commonly used surface wave devices are the SAW sensor and the shear-horizontal surface acoustic wave (SH-SAW) sensor, also known as the surface transverse wave (STW) sensor.[32,33]

1.2.2 Bulk wave sensors

The best known, simplest and oldest TSM resonator is the quartz crystal microbalance.[34] A quartz crystal microbalance is a small, thin disk of AT-cut quartz with parallel circular metal electrodes bonded on both sides to make electrical connections. An AT-cut crystal is a thin piece of quartz with two parallel or slightly convex surfaces.[35] The metal electrodes are used to induce an oscillating electric field perpendicular to the surface of the wafer. The application of a voltage causes the AT crystal to move sideways internally in thickness shear movement as shown in Fig.1.2

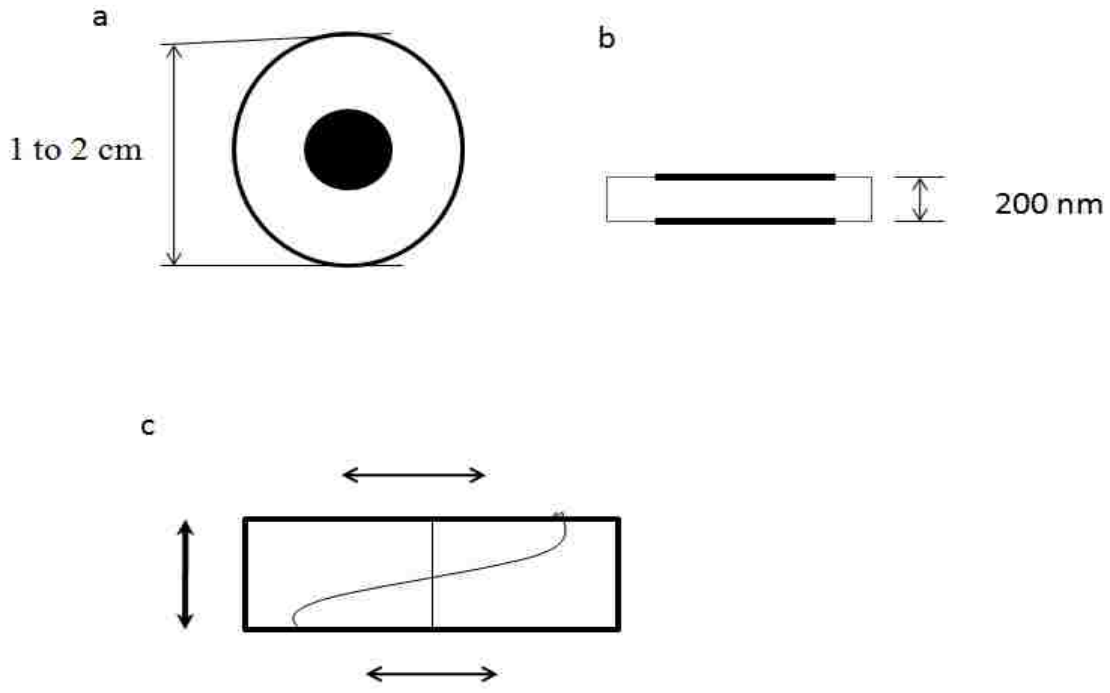

Figure 1.2 Thickness shear mode resonator, top view (a) showing the metal electrode, side view (b) showing the crystal thickness and shear deformation of the crystal (c) during oscillation at fundamental frequency. Side arrows show the direction of wave propagation

The sensor is typically used in an oscillator circuit, where the oscillation frequency tracks the crystal frequency and indicates mass accumulation on the device. The TSM is simple to manufacture, withstands harsh environments, is temperature stable, and is applicable for liquid phase sensing because the shear acoustic wave is not affected by liquid damping effect. Typical TSM resonators operate between 5–30 MHz.[30]

1.2.3 Selection of polymer coatings for acoustic wave sensors

One of the challenges in using commercial polymers for coating acoustic wave device is the method of choosing the most sensitive and selective polymer coating. Infrared spectroscopy studies have been reported to provide physical and chemical information on the interaction of polymer coatings with analytes of interest.[4, 36, 37] This information provides a basis for choosing the most appropriate polymer coating for a given analyte. When molecules sorb or partition into a polymer coating they establish a dynamic equilibrium between the polymer coating and the solvent medium. This equilibrium is referred to as the partition coefficient, K_p.[4] This equilibrium constant has been extensively utilized in gas phase sensing to describe the selectivity of a polymer coating to a given analyte .[14,15,38] In all of the studies utilizing the partition coefficient as the screening tool, K_p is modeled using regression analysis of experimental data with linear solvation energy relationship (LSER) shown in equation 1.1

$$LogK_p = c + rR_2 + s\pi_2^H + a\alpha_2^H + b\beta_2^H + ILogL^{16} \qquad 1.1$$

where $LogK_p$ is the log of the gas-polymer partition coefficient, K_p, and relates to a series of vapors for one solvent or polymer. K_p is a measure of the strength of the solute-solvent interactions. In this definition, solvent refers to the polymer coating and the solute is the analyte of interest. The variables $R_2, \pi_2^H, \alpha_2^H \beta_2^H$ in equation 1.1 are solute parameters that model polarizability from non-bonding and π electrons, the dipolarity, the hydrogen bond acidity, and the hydrogen bond basicity respectively. L^{16} is the gas-liquid partition coefficient on n-hexadecane. Parameters r, s, a, b and I are the corresponding solvent (polymer) parameters. However, use of LSER to model the partition coefficient is limited by the following: [1]

- Many solutes interact by only one or two of the five interactions presented in the LSER model.
- Regression models used to predict partition coefficients with LSER have large regression constants indicating residual unexplained components of the overall vapor-polymer interactions
- Partition coefficients obtained from gas chromatography, which forms the basis of LSER determination, may not accurately predict the gravimetric component of acoustic wave sensor response.

However, other methods such as spectroscopic and computational chemistry can be used to evaluate the sensitivity of polymers for use as coatings in acoustic wave sensors.[4]

1.2.4 Attenuated total reflectance Fourier transform infrared spectroscopy

ATR-FTIR spectroscopy has been used as a screening tool for polymer coatings for QCM devices. [4,39] Infrared spectroscopy is an excellent tool for this goal because spectral features can be used to identify molecular species in a sample, determine the concentration of a specific analyte given appropriate calibration, and also provide insight into the chemical and physical interactions between analytes and coatings.[40]

The ATR-FTIR consists of a crystalline prism with a refractive index higher than the lower and upper interfaces of the crystal. The crystalline prisms is referred to as the internal reflection element (IRE) or the denser medium, while the sample, is referred to as the rarer medium, because of its lower refractive index. Electromagnetic radiation I_o, diffusing in the crystal with an angle of incident θ, greater than the 'critical angle' θ_c is totally reflected. The beam then travels inside the ATR crystal and finally exits from the other side of the face as I. Fig. 1.3 shows a schematic representation of a horizontal ATR crystal with 10 reflections.

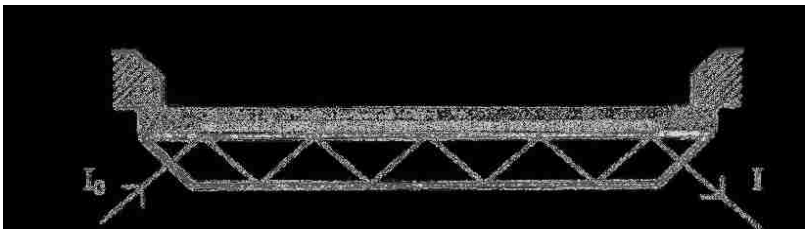

Figure 1.3 Schematic representation of total internal reflection. The shaded region shows the sample placed in contact with top surface of the IRE

The radiation penetrates the interface before being reflected into the denser medium and this creates an 'evanescent field' along the axis of the crystal. The depth of penetration of the evanescent wave into the rarer medium,d_p, depends on the wavelength, the refractive indices of the two media and the angle of incidence at the interface as expressed in equation 1.2[37] below:

$$d_p = \frac{\lambda}{2\pi n_1 \sqrt{(\sin\theta)^2 - (\frac{n_2}{n_1})^2}} \qquad 1.2$$

Where λ= the incident IR radiation

n_1=the refractive index of the ATR crystal

n_2=the refractive index of the sample.

θ=the angle of incident IR radiation to the crystal

If an absorbing surface uniformly covers the upper surface of the ATR crystal, the 'evanescent wave' will be attenuated, (hence the name attenuated total reflection) and appropriate conversion yields a spectrum very similar to the conventional transmission spectrum. The ATR-FTIR technique is attractive as a characterization tool for various reasons, including its simplicity and non destruction of the sample. In addition, the penetration depth is appropriate for designing experiments to study diffusion kinetics.[37] In a study on the diffusion of methanol in polystyrene and in polymethylmethacrylate, Fieldson and Barbari[41] reported that any change within the 'evanescent wave' penetration depth due to diffusion in the polymer can be monitored *in situ* provided the compound has distinguishable IR absorption bands.

1.3 Sorbents for water and wastewater treatment

In water and wastewater treatment the sorption generally involves the removal of contaminants, such as metal ions and organic compounds from water by solids or semi-solid sorbent particles. Two main driving forces are responsible for the sorption of compounds by such sorbents in water: the hydrophobic character of the sorbates and/or the affinity of the sorbates for the sorbent.[9] Solid materials such as activated carbon as well as biopolymers are widely used to absorb liquids or gases in water treatment[42-44] as well as wastewater treatment.[45] Phenol based organic pollutants have been successfully adsorbed from water using activated carbon.[46,47] Synthetic resin sorbents such as polymer-supported amino-bis(cispropane2,3-diol) and the commercially available Lewatit M610 anion exchange resins are used in a variety of industrial applications such as purification processes in the food and drug industry, odor control, and industrial wastewater treatment.[5] They have also been used in a number of groundwater remediation applications (e.g., removal of halogenated organic compounds) and landfill leachate purification.[48] Biodegradable biopolymers such as chitosan have been applied for the removal of dyes from aqueous solutions.[49]

The large surface area, micro-porous character and the chemical nature of their surfaces have made activated carbon materials of interest as potential adsorbents for the removal of heavy metals from industrial wastewater. Organic compounds such as methyl tert-butyl ether (MTBE), an additive in fuel for improving combustion efficiency, has been effectively removed from water using granular activated carbon.[50] The major disadvantage of activated carbon in its application as a sorbent is that it requires high regeneration costs. Compared to activated carbons, synthetic resins are easily

regenerated and because the manufacturing of synthetic resins is a controlled process, they can be manipulated to optimize their performance for specific functions.

Two dimensional nanostructured layered inorganic or inorganic/organic compounds have been developed and applied in catalysis,[51] fire retardancy,[52] ion exchangers, [53] as well as adsorbents for water purification.[54] Layered double hydroxides (LDH) with positively charged metal sheets counter-balanced by interlayer anions which are exchangeable for anions in water have been extensively studied as potential adsorbents for anionic contaminants such as 2.4-dichlorophenoxyacetate,[6,55] arsenate[6] and arsenite.[56] The expandable interlayer spaces for layered double hydroxides and hydroxyl double salts are a favorable characteristic for use as adsorbents.

Use of layered inorganic materials as adsorbents for organic pollutants can be achieved by exchanging the interlayer inorganic anions with surfactants such as dodecylsulfate,[57] hexdecylatimethylammonium[58] and certylpyridinium.[59] For example, inorganic/organic layered double hydroxides have been shown to exhibit higher affinity for chlorophenol when compared to the unmodified layered double hydroxide.[57] Natural clays such as vermiculite, illite and smectites have been modified, using the organic cation hexadecyltrimethlyammonium (HDTMA), to remove nonionic organic compounds (NOC) .[58] The sorption process was reported to be similar to the dissolution of NOCs in a bulk organic solvent such as hexane octane.[58] The main disadvantage of using layered double hydroxide- based sorbents is that they are unstable under acidic conditions because the metal hydroxide layers are soluble under low pH values.

1.3.1 Layered zirconium phosphate

α-Zirconium bis (monohydrogen phosphate) monohydrate, α-$Zr(HPO_4)_2.H_2O$ (abbreviated α-ZrP) is a well known layered inorganic ion exchanger with an interlayer distance of 7.6 Å. Each layer consists of a plane of zirconium atoms sandwiched between two phosphate groups. Each Zr (IV) ion is surrounded by six oxygen atoms in an octahedral symmetry such that each phosphate group is coordinated to three zirconium ions. The free hydroxyl group of each phosphate is oriented perpendicular to the metal phosphate layers.[60] Such an arrangement makes the α-ZrP acidic because of the ionizable hydroxyl group. The interlayer spacing in α-ZrP can be expanded to accommodate cationic as well as neutral guests. Fig.1.4 is a schematic representation of α-ZrP.

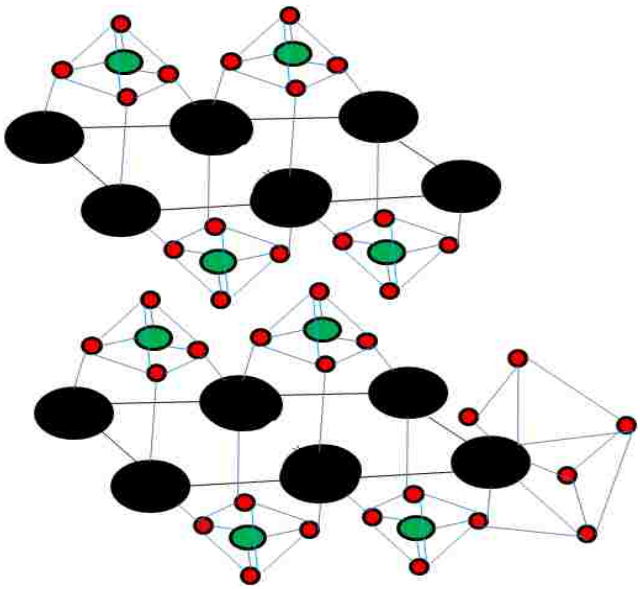

Figure 1.4 Schematic representation of α-ZrP. Black circles represent zirconium atoms, green circles represent phosphorus atoms and red circles represent oxygen atoms. Hydrogen atoms and water molecules are not shown

α-ZrP can easily be organically modified using alkylamines. Intercalation of alkylamines in α-ZrP has long been studied.[60-62] Amines, which possess a Brønsted basic character, have a high affinity for the Brønsted acidic P-OH groups and are easily adsorbed. Electrostatic attraction between the polar head groups of the protonated alkylamines and the negatively charged phosphate surface drives the intercalation reaction, even though the organization of the chains is not entropically favored.[63] Primary alkylamines have been shown to form bilayer conformations in the zirconium phosphate gallery spaces.[64-66] It has been reported that the free area surrounding each phosphate group in zirconium phosphate is 24 $Å^2$.[67] The cross-sectional area of *trans-trans* alkyl chain has been reported to be 18.6 $Å^2$.[68] This suggests that there is just enough room for one alkyl chain for every P-OH group, assuming the chains are oriented perpendicular to the zirconium phosphate layer. Amines intercalated at over 50% saturation cannot interpenetrate into the layer already present and a bilayer is obtained. At full saturation, all the crystal sites available for intercalation are occupied and phases of composition $Zr(PO_4)_2.2.C_nH_{2n-1}NH_3.nH_2O$ are formed. The arrangement of alkylamines in the gallery space of α-ZrP was derived from the analysis of the correlation between the interlayer distance and the number of carbon atoms in the alkylamine chain.[68] The organically modified α-ZrP can be used as an adsorbent of organic compounds in aqueous solutions. Butylamine intercalated zirconium phosphate was reported to effectively remove phenols from aqueous solution.[69]

1.4 Motivation of the study

In order to design effective sorbents for a particular use, a thorough understanding of the interactions between the sorbent material and the sorbates is very important. Polymers that are used for coating quartz crystal microbalances in developing chemical sensors have specific functional groups that can interact favorably with the analyte of interest. Key properties of chemical sensors based on quartz crystal microbalance are that they are portable, inexpensive and have the ability to provide real-time analysis.

Quercetin is a flavonoid of widespread importance in human health including its anticancer activity. [70] Chromatographic techniques that are mainly used for detecting quercetin are very expensive, require long analytical time and are not suitable for real-time analysis. The use of layered materials such as layered double salts for organic pollutants is hampered by their hydrophilicity. Surfactants have been used to modify layered inorganic materials to make them more suitable for organic pollutant removal. However, most layered double hydroxides are unstable in acidic medium. Layered zirconium phosphate is readily synthesized from simple starting materials. It is thermally stable and chemically inert in neutral/acidic medium. The primary objectives of the work described in this dissertation are:

1. *To develop a simple and affordable method for the detection of quercetin based on quartz crystal microbalance sensor*. The potential use of commercially available PECH, PIB and PIB as coatings for a QCM sensor to detect quercetin is studied using attenuated total reflectance Fourier transform infrared spectroscopy (ATR-FTIR) spectroscopy. The selection of the most suitable polymer is based on

the sorption rates which are represented by diffusion coefficients. Hydrosilation reaction is utilized to synthesize a hybrid inorganic/organic polymer that can potentially interact with quercetin through hydrogen bonding and π-π interactions. This provides an alternative coating that is more sensitive to quercetin than the commercial polymers utilized in this study.

2. *To develop a sorbent for removal of organic pollutants from aqueous solution.* The use of a tertiary amine to organically modify layered zirconium phosphate in order to increase its affinity for organic pollutants is explored. Basic characterization of the compound will be discussed using X-ray diffraction, Fourier transform infrared (FTIR), nuclear magnetic (NMR) spectroscopy, thermogravimetric analysis (TGA), transmission electron microscopy (TEM) and elemental analysis. The effectiveness of the organically modified layered zirconium phosphate to remove 4-chlorophenol as a model pollutant is evaluated using parameters experimentally determined from sorption kinetic studies and equilibrium adsorption isotherms.

2 EXPERIMENTAL METHODS

2.1 Attenuated total reflectance Fourier transform spectroscopy

In this study ATR-FTIR spectroscopy was used to investigate the diffusion of quercetin in polymer films and characterization of zirconium phosphate and alkylamine intercalated zirconium phosphate powders. The ATR crystal or internal reflection element (IRE) used in this study is a zinc selenide (ZnSe) crystal obtained from PIKE Technologies. The ATR crystal used for studying the sorption of quercetin in polymer films is a horizontal trough plate that is 80 mm long, 10 mm wide and 4 mm thick. These dimensions result in 10 reflections of the infrared energy in the crystal. A single reflectance ATR accessory was used for studying the infrared absorption spectra for powder samples. The characteristics of the ZnSe crystal used in this study are summarized in Table 2.1

Table 2.1. Characteristics of the ZnSe horizontal ATR crystal used for diffusion experiments

Refractive index at 1000 cm^{-1}	2.4
Spectral range (cm^{-1})	20000-675
Operational pH range	5-9
Penetration depth for a sample with a refractive Index of 1.4 at 1000 cm^{-1} with a 45^0 angle of incidence	1.66

Fig.2.1 shows the experimental set up for studying the sorption of quercetin in the polymer films using ATR-FTIR. The experiments were performed on a Nicolet Magna-IR 560 spectrometer operated at 2 cm^{-1} resolution in the 4000 -650 cm^{-1} region.

Figure 2.1 FTIR spectroscopy experimental set up for studying sorption of quercetin in polymer films. Polymer films were deposited on the Horizontal ATR prism shown in the picture

FTIR spectra of powder samples were obtained using a Perkin Elmer Spectrum 100 FTIR spectrometer equipped with a single reflectance ATR crystal.

2.2 Quartz crystal microbalance (QCM)

The sensing mechanism of a QCM also known as a Thickness shear mode (TSM) resonator was described in Chapter 1. The QCM200 apparatus used in this study was purchased from Stanford Research Systems. The components of a QCM200 system are shown in Fig.2.2.

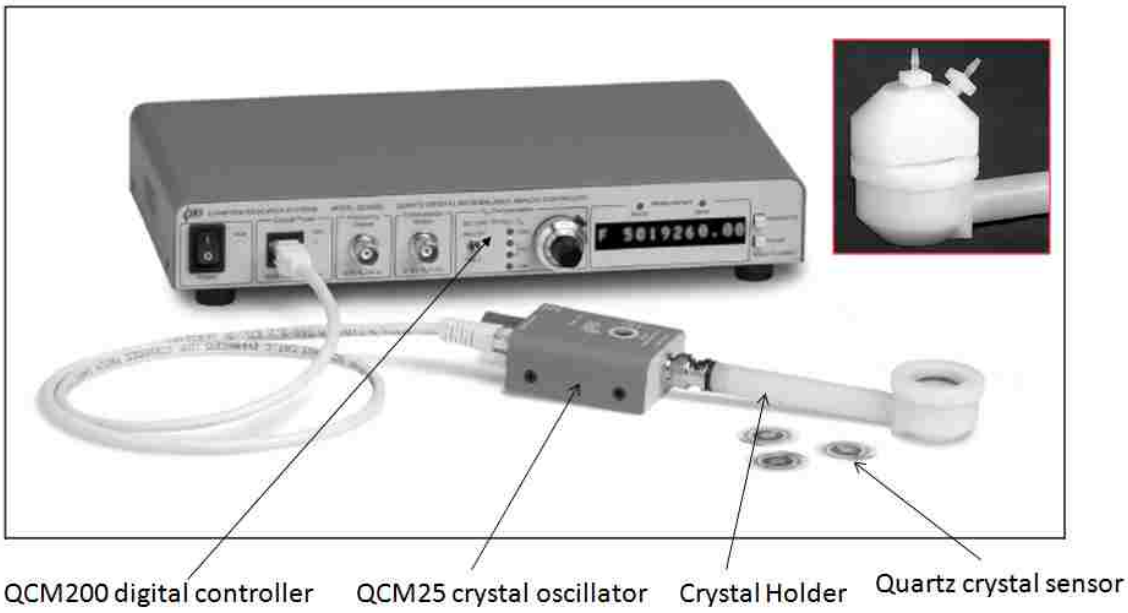

Figure 2.2. A complete QCM 200 set up. The insert shows a flow through cell used for measuring liquids. (Adapted from the manual of QCM 200 from Stanford Research Systems)

The quartz crystal sensors shown in Fig.2.2 are 2.54 cm (1 inch) in diameter. They consist of thin disks of 5 MHz, AT-cut, α-quartz with circular electrodes patterned on both sides. The two electrodes are coated with gold/platinum. The crystal holder

consists of a chemically resistant material, Kynar®, an O-ring and a 50-ohm BNC connector that connects the crystal sensor to the oscillator. Frequency measurements can be monitored using the digital controller connected to the crystal oscillator. The digital controller can measure the series resonance frequency at 0.1 s, 1 s and 10 s gate times with resolutions of 1.0 Hz, 0.1 Hz and 0.01 Hz respectively. Series resonance resistances are also monitored using the digital controller. The resolution of resistance measurements varies with the operational resistance; for resistance, $R< 100\ \Omega$, the resolution is 0.001 Ω, for $100 <R<1000$ the resolution is 0.01 Ω and for $1000\ \Omega < R< 5000\ \Omega$, the resolution is 0.1 Ω. For most of the measurements done in this study, the resistances ranged from 360 Ω to 650 Ω. 10 s and 1 s gate widths were used depending on the noise level observed during sensor conditioning.

A number of crystal sensor cleaning protocols are recommended by the manufacturer depending on the nature of the solutions analyzed. A piranha solution (3:1 mixture of sulphuric acid and 30 % hydrogen peroxide) was used to clean sensor crystals. Piranha solutions are widely used to remove organic residues from substrates. The crystals were cleaned using a piranha solution under sonication for 30 minutes. After rinsing with deionized water, the crystals were sonicated in a 3:1 v/v mixture of ethanol and chloroform for another 30 minutes before being rinsed with deionized water and then dried under a stream of nitrogen gas. The cleaning process was done at room temperature. The cleaned crystals were stored in a desiccator. Polymer solutions were spin coated using a Speciality Coating System (SCS P6078). The spinning speed and time varied with the desired film thickness. A film thickness of 1 μm was achieved by spinning at 3000 rpm for 33 s.

2.3 X-ray diffraction

The atomic planes of a crystal can cause an incident beam of X-rays to interfere with one another as they leave the crystal. This phenomenon is known as X-ray diffraction (XRD). This technique can be used for a number of applications including; identifying crystalline phases and orientation, determine structural properties such as lattice parameters, grain sizes and phase compositions.

Powder X-ray diffraction patterns were obtained using a Rigaku Miniflex II diffractometer operated in para-focusing Bragg-Bretano configuration, with a 1.25º divergence slit (DS),1.25º scatter slit (SS), 0.3 mm receiving slit (RS), 0.15 mm monochromator receiving slit (MRS), and a Cu K_α (λ=1.54 Å) radiation source operated at 30 kV and 15 mA. Data acquisition was performed using step widths of 0.036º. Powder samples were mounted on a glass sample holder supplied by the manufacture. The sample holder did not show any diffraction pattern. Peak positions in the low 2 theta angles were used to characterize the interlayer spaces. Interlayer spaces were estimated using Bragg's law[71] expressed by equation 2.1

$$n\lambda = 2d\sin\theta \qquad 2.1$$

where λ is the wavelength of the radiation source, 1.54 Å , d is the interlayer space between the planes in the atomic lattice and θ is the angle between the incident ray and the scattering planes.

2.4 Thermogravimetric Analysis (TGA)

TGA measures weight changes in a material as a function of temperature or time under a controlled atmosphere. Its primary uses include measurement of a material's thermal stability and, when coupled with other analytical methods, composition. Thermogravimetric analysis was performed on a NETZSCH TG 209 F1 thermogravimetric instrument using Al_2O_3 crucibles. Samples were heated from 50 ^{0}C to 800 ^{0} C in air at a heating rate of 10 K/min with samples sizes of 15 ± 1 mg. The flow rate of the air was 85 ± 5 min/L. Samples were analyzed in triplicate. The NETZSH TG 209 F1 TGA instrument was coupled to a Fourier Transform infrared spectroscopy instrument that is capable of analyzing the infrared absorption bands of the gases evolved during sample heating. Thermogravimetric measurements were used to estimate composition of zirconium phosphate and the intercalation products

2.5 Transmission Electron Microscopy (TEM)

TEM experiments were performed by Dr. Zhu of the Department of Energy, Environmental and Chemical Engineering at Washington University in St. Louis. TEM images were captured with a Tecnai G2 Spirit Twin electron microscope operated at 120 kV (FEI, Hillsboro, OR). Samples were dissolved in ethanol and dropped onto a piece of carbon-coated copper grid (Ted Pella, Inc.). Ethanol was evaporated before taking measurements.

2.6 UV-Visible spectroscopy

A Perkin Elmer Lambda 35 UV-Vis spectrometer was used to acquire UV-VIS absorption spectra of liquid samples. The spectrometer use deuterium and tungsten prealigned lamp source with automatic switch over in the 190-1100 nm range operated at 2 nm resolution. Samples were collected in the scanning mode using quartz cuvettes with a path length of 1 cm.

2.7 Nuclear Magnetic Resonance (NMR) spectroscopy

Solution ^{1}HMR and ^{13}CMR experiments were performed on a Varian 400 MHz spectrometer using $CDCl_3$ solvent. Solid state NMR experiments were performed by Dr. Foersterling of the Department of Chemistry and Biochemistry at the University of Wisconsin –Milwaukee. All solid state NMR experiments were performed on a Bruker DRX500 NMR spectrometer equipped with a Doty DSI-210 CP-MAS probe. Spinning speeds were between 8.5 - 9 kHz. P-31 spectra were acquired both with one-pulse excitation and with $^{1}H/^{31}P$ cross polarization (CP). The one-pulse P-31 spectra were acquired with 256 scans and proton decoupling during acquisition. For the CP experiment, 128 scans were acquired. Hartmann Hahn match conditions[72] were optimized using a sample of $ZrPO_4$ at the same spinning speed. Phosphorous NMR chemical shifts are referenced against 85% H_3PO_4 as 0 ppm using $NH_4H_2PO_4$ as secondary reference (1 ppm).

2.8 Preparation of Materials

2.8.1 Polymer films and analyte preparation

Polyepichlorohydrin (PECH) (M_w=700,000; density=1.36g/cm^3; refractive index=1.54), polycaprolactone (PCL) (M_w=80,000; density=1.15 g/cm^3; refractive index=1.48) and polysiobutylene (PIB) (M_w=4,200,000; density=1.51 g/cm^3 refractive index=1.51) Quercetin dehydrate (M_w=338.26, 98+%) dichloromethane (99%) ethanol (95%), 2,2'-diallybisphenol A (BPA), 1,1,3,3,5 hexamethyltrisiloxane (HMTS), Platinum(0)-1,3-divinyl-1,1,3,3-tetramethyldisiloxane (Pt-DVTMDS) complex solution in xylene (Pt ~2 %),were purchased from Sigma-Aldrich. Fig. 2.3 shows the chemical structures of the monomers of the commercial polymers used in this study.

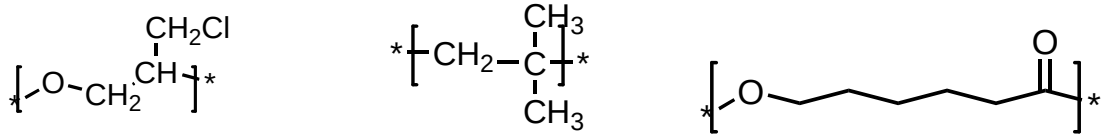

polyepichlorohydrin polyisobutylene polycaprolactone

Figure 2.3 Chemical Structures of the commercial polymers used in this study

1% w/v polymer solutions were prepared by dissolving 0.25 gram of the polymer in 25 ml of dichloromethane. The mixtures were stirred overnight to ensure complete dissolution of the polymers. Desired concentrations of quercetin were achieved by dissolving quercetin in ethanol to achieve target concentrations.

A hybrid organic/inorganic copolymer, bisphenol A hexamethyltrisiloxane (BPA-HMTS) was synthesized according to a literature method[27]. Briefly, (0.882 g, 0.00286 mol) of BPA (M_w = 308.41 g/mol) was dissolved in 10 mL of toluene in a vial. This mixture was stirred for about 5 min. until a homogeneous mixture was obtained. To this solution, 0.566 g (0.00271 mol) of HMTS (M_w = 208.48 g/mol) was added to give a mole ratio for reacting functional groups, r = [SiH]/[CH2=CH], of 0.95. 10 mL of toluene was added to this solution, stirred for about 1 min, and the presence of the Si-H (2125 cm^{-1}) group monitored by FTIR. Two drops (~ 0.02 g) of Pt-DVTMDS were added and the solution was heated and stirred at 110-115 °C in an oil bath. After 20 minutes, all of the Si-H at 2125 cm^{-1} had been consumed. This was confirmed by the disappearance of the Si-H group in the FTIR spectra (See Appendix A). Subsequently, 0.17 g (for a total of 0.736 g, 0.00353 mol, r = 1.23) of HMTS was added to the reaction mixture until excess Si-H was detected in the FTIR spectra. Five drops (~ 0.058 g) of the catalyst were added in order to terminate the polymer with vinyl groups. Polymerization took place in a three-neck round-bottom flask using a reflux set-up in an oil bath at 100-110 °C for 2 hours while stirring. At the end of the reaction, the solvent was evaporated on a rotary evaporator and the sample was dried under vacuum at 60 ^{0}C. The chemical structures of the monomers used in synthesizing BPA-HMTS are shown in Fig.2.3

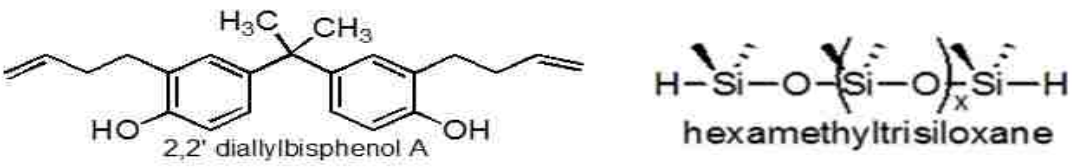

Figure 2.4 Chemical structures of the monomers used to synthesize BPA-HMTS

Spectroscopic characterization of the polymer was obtained on a Perkin Elmer Spectrum 100 FTIR spectrometer and Varian 400 NMR spectrometer. Differential Scanning Calorimetry (DSC) was performed under nitrogen on a DSC 822e Mettler Toledo Inc (Columbus Ohio) instrument. The glass transition temperature $T_{g,}$ is reported as the inflection point in the DSC trace (See Appendix A)

BPA-HMTS density was estimated using a 1 mL volumetric flask. Briefly, a 2.8 %wt BPA-HMTS in chloroform was prepared. The empty flask with the stopper was then weighed (W_1) and partially filled (50%) with BPA-HMTS solution. The flask was placed in an oven and heated at 50 °C for 24 hrs to remove the solvent. Afterwards, the flask with the lid and just the polymer was weighed (W_2). The flask was then filled with deionized (DI) water to the 1 mL and weighed (W_3). The density of the film (ρ_f), in g/cm^3, was then estimated using the relation

$$\rho_f = \frac{Mass}{Volume} = \frac{W_2 - W_1}{1 - V_1}$$

where V_1, the volume of water, is given by W_3-W_2 since the density of water is 1 g/cm^3.

2.8.2 Preparation of α zirconium phosphate

Zirconium (IV) chloride (99.5 %), phosphoric acid (85 % w/v) and N,N dimethylhexadecylamine (95 %), N,N dimethyltetradecylamine (95 %), butylamine (99 %), octylamine (95 %), hexadecylamine (95 %) were purchased from Alfa Aesar. Reagents were used without further purification. Zirconium phosphate (α-ZrP) was prepared using a literature synthesis.[61] Thirty grams of zirconium chloride were dissolved in 100 ml of deionized water. The zirconium chloride solution was mixed with

12 M phosphoric until a gel was formed. The gel was then refluxed in excess phosphoric acid at 110 ^{0}C for 72 hrs. The resulting precipitate was filtered, washed several times with water until the pH of the filtrate was neutral and then dried at 50 ^{0}C under vacuum. The intercalation of alkylamines in zirconium phosphate is described in Chapter 4

3 DETECTION OF QUERCETIN USING A POLYMER COATED QUARTZ CRYSTAL MICROBALANCE

3.1 **Introduction**

Polyphenols have a number of biological functions in plants, including signaling, fertility, and protection against UV-light and phytopathogens.[73] Polyphenols show a great diversity of structures, ranging from rather simple molecules (monomers and oligomers) to polymers.[74] They can be divided into four major classes, according to the nature of their carbon skeleton, i.e. phenolic acids, flavonoids, stilbenes and lignans. Flavonoids are the most abundant polyphenols in our diet.[75] They consist of a three-ring structure and can be divided into several classes, depending on the degree of oxidation of the heterocyclic ring (also called ring C): flavones, flavonols, isoflavones, anthocyanins, flavonols, and flavanone.[76] The major classes of flavonoids are depicted in Fig. 3.1

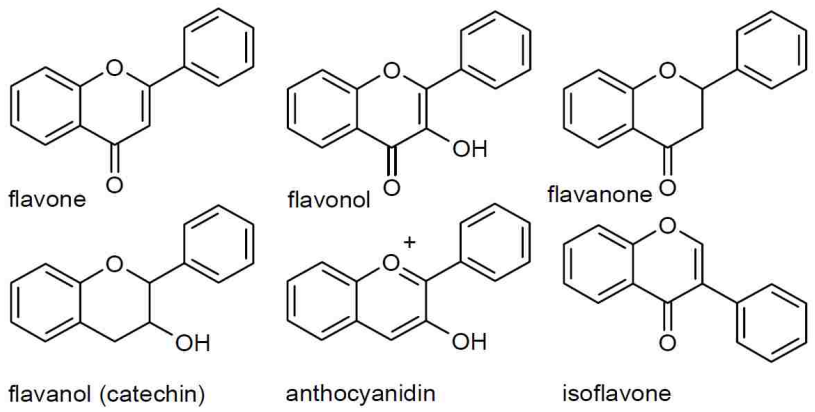

Figure 3.1 Chemical structures of major flavonoids

Quercetin (Fig. 3.2 A) is the main flavonol present in human diet.[3] In a study carried out by Hertog *et al.*[77] in seven countries, the average daily intake of flavonoids varies from approximately 3 mg/day in West-Finland to 68 mg/day in Japan. Quercetin represents 40 to 100 % of this total intake. Due to its interesting chemical and biological properties, [78] quercetin has been one of the most studied flavonoids. Quercetin occurs mainly as the glycoside[79] (Fig 3.2B) in a wide variety of fruits, vegetables and beverages.

In plants, different types of sugars, including glucose, galactose, rhamnose, rutinose or xylose, are bound to the hydroxyl groups of the aglycone (the non-sugar part) by glycosidic bonds. As an example, Fig. 3.2 B shows the structure of quercetin-*4`*-β-*D*-glucoside.

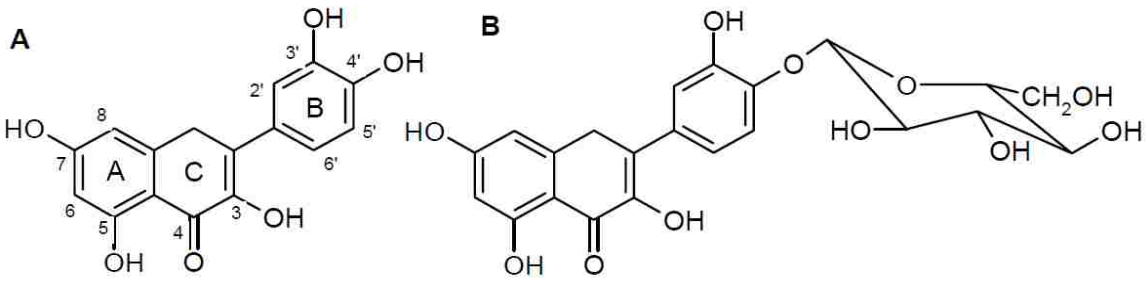

Figure 3.2 Chemical structures of quercetin showing the numbering of its carbon atoms and rings and quercetin-4-β-D-glucoside (B)

3.1.1 Beneficial health effects of quercetin.

There is a considerable amount of epidemiological evidence associating rich diets in fresh fruits and vegetables with lower risks of suffering cardiovascular conditions and certain types of cancer.[80-82] Some flavanoids have been reported to possess a variety of biological activities, including antiallergic, anti-inflammatory, antiviral and antiproliferative activities.[83] In a large number of *in vitro* studies, flavonoids have been characterized as good antioxidants. [70,84,85] Structural features attributed to the antioxidant properties of flavonoids include a C_2=C_3-double bond, a C_4-keto group, a C_3-hydroxyl group and an *ortho*-diphenolic structure, also called catechol group, in the B-ring.[70] Quercetin possesses all these structural elements (see Fig.3.2A), and the potent ability of quercetin to scavenge reactive oxygen species,[86-88] singlet oxygen,[89] in addition to radicals of different origin has been confirmed in various *in vitro* systems.[90,91] These features have led to the application of quercetin as an ingredient of functional foods and food supplements.[92] In health shops and on the Internet, a large number of quercetin supplements are sold as potential cures and/or preventive agents for a large variety of physical discomforts, including hay fever, cataract, bruises, and prostate problems.[93,94] The beneficial health effects of quercetin make it imperative for continuous search of quality control and detection methods that are fast and affordable.

3.1.2 Analytical Methods for detecting quercetin

A number of analytical and spectroscopic methods have been used for the separation of quercetin in flavonoid mixtures found in plant samples.[95] High performance liquid chromatography (HPLC)[76,96] capillary electrophoresis (CE),[95] gas chromatography(GC),[97] have been effectively used for the separation, coupled with various detection techniques such as UV spectrophotometry, mass spectrometry, electrochemical detection and chemiluminescence.[98] Other hybrid methods such as HPLC coupled with calorimetric detection of the antioxidant activity of flavonoids were reported to achieve separation and detection of quercetin and rutin in plant extracts such as *Sophora japonica* and *Morus alba*.[99] The coupling of these techniques may provide high selectivity of the analytes, but they also have some disadvantages of high operational costs and time consuming protocols. It has been reported that application of HPLC in analysis of traditional Chinese medicine often has short column time due to contamination.[98]

The objective of this study is to develop an affordable technique of detecting quercetin. Chemical sensors have been reported to have the advantage of real-time analysis. In this study, a chemical sensor based on quartz crystal microbalance (QCM) is developed. QCMs are known to provide very sensitive mass measuring because their resonance frequency decreases upon an increase of a mass on the QCM up to the nanogram level.[33] Mass sensitive sensing is a popular method as it has the great advantage that mass is the most fundamental physical property of any analyte, thus the resulting sensors can in principle be universally applied.[100,101]

However, one of the challenges of using quartz crystal microbalances is the need

to develop coatings that are selective to the analyte of interest because with QCM any substance that can cause a mass change on the device can be detected. This chapter discusses the use of attenuated total reflectance Fourier transform infrared (ATR-FTIR) spectroscopy as a tool to select polymer coatings that can be used on a QCM sensor for detecting quercetin. The screening method utilizes diffusion coefficients of quercetin in polyepichlorohydrin (PECH), polyisobutylene (PIB) and polycaprolactone (PIB) obtained from monitoring the infrared absorption bands of quercetin in the polymer film as a function of time. The sensor response results of a QCM device coated with PECH and PIB are presented. Although PCL showed the highest diffusion coefficients, the quality of adhesion of the PCL film on a QCM device was poor; to that end the results will not be presented. The response of a QCM coated with BPA-HMTS polymer that was synthesized using the hydrosilation is also discussed in this Chapter. This polymer showed higher sensitivity to quercetin than PIB and PECH.

3.2 Experimental

Quercetin dihydrate, ethanol (95%) and dichloromethane (Sigma-Aldrich) were used as received from the manufacturer. Polyepichlorohydrin (PECH), polyisobutylene (PIB) and polyepichlorohydrin (Sigma-Aldrich) were used to prepare polymer coatings. 1 % (w/v) polymer solutions were prepared as described in Chapter 2. The chemical structures of PECH, PIB, PCL and the monomers used for the synthesis of Bisphenol A-hexamethyltrisiloxane (BPA-HMTS) hybrid polymer are shown in Fig.2.3 and Fig.2.4 respectively

3.2.1 Time resolved ATR-FTIR

For each experiment, 1 ml of the 1 % (w/v) polymer solution in dichloromethane was cast onto an ATR prism with dimensions (80 mm x 10 mm x 6 mm). The solvent was evaporated in an oven at 50 ˚C for 24 hours under vacuum to form a polymer film on the ATR prism. Film thicknesses were estimated using published polymer densities and the dimensions of the ATR prism. The polymer-coated ATR prism was placed on a Nicolet Magna 560 FTIR spectrometer. An uncoated ATR prism was used to collect background spectrum. A 1 ml solution of quercetin (10 mM) in ethanol was spread over the coated prism, covered with a volatiles cover, and the ATR-FTIR spectra were collected at different time intervals to study the diffusion process of quercetin solution. Spectra were averaged over forty scans at a resolution of 2 cm^{-1}.

3.2.2 Quartz crystal microbalance

1 % (w/v) polymer solutions were spin coated on the crystals as described in section 2.2. The coated device was mounted on a crystal holder with an O-ring. The coated side of the crystal was exposed to a flowing solution using a 1.5 ml flow-through cell connected to a peristaltic pump. Ethanol solution was first flowed through the polymer coated device to obtain a stable baseline for frequency measurements at room temperature. The average time to achieve a stable baseline was 3 hours at a flow rate of 0.24 ml/min. After the stability of the frequency of the QCM electrode in ethanol was confirmed, different concentrations of the quercetin ethanol were introduced. Between exposures to different concentrations of quercetin, the device was flushed with ethanol to return the response to the baseline. Frequency changes were monitored using a frequency

counter (model QCM200 SRS) connected to a computer with LabView software for data acquisition. To study the concentration dependence of the sensor response, PIB and PECH coated sensors were exposed to four different concentrations ranging from 75 -300 ppm. The BPA-HMTS coated device was exposed to five different concentrations ranging from 2 ppm – 30 ppm. Assuming a uniform, rigid, thin film coating the Sauerbrey equation[102] can be used to relate frequency changes to adsorbed mass as shown in equation 3.1:

$$\Delta f = -C_f \Delta m \qquad 3.1$$

where

Δf = observed frequency change in Hz

Δm = the change in mass per unit are, in g/cm^2

C_f = sensitivity factor for the crystal (56.6 Hz μg^{-1} cm^2 for a 5 MHz crystal at room temperature)

3.3 Results and Discussion

3.3.1 Characterization of the Infrared bands of quercetin

In this section the principal bands of a solid sample of quercetin are first determined for comparison with the ATR spectrum of quercetin-ethanol solutions. Infrared correlation charts as well as band assignments by Cornard *et al.*[103] were used to assign the spectra. Fig.3.3 shows the IR spectrum of quercetin in the wavenumber range 3600 cm^{-1}

to 940 cm^{-1}. The spectrum shows a typical profile of the phenolic polymerization[104] with a broad band centered at 3300-3400 cm^{-1}.

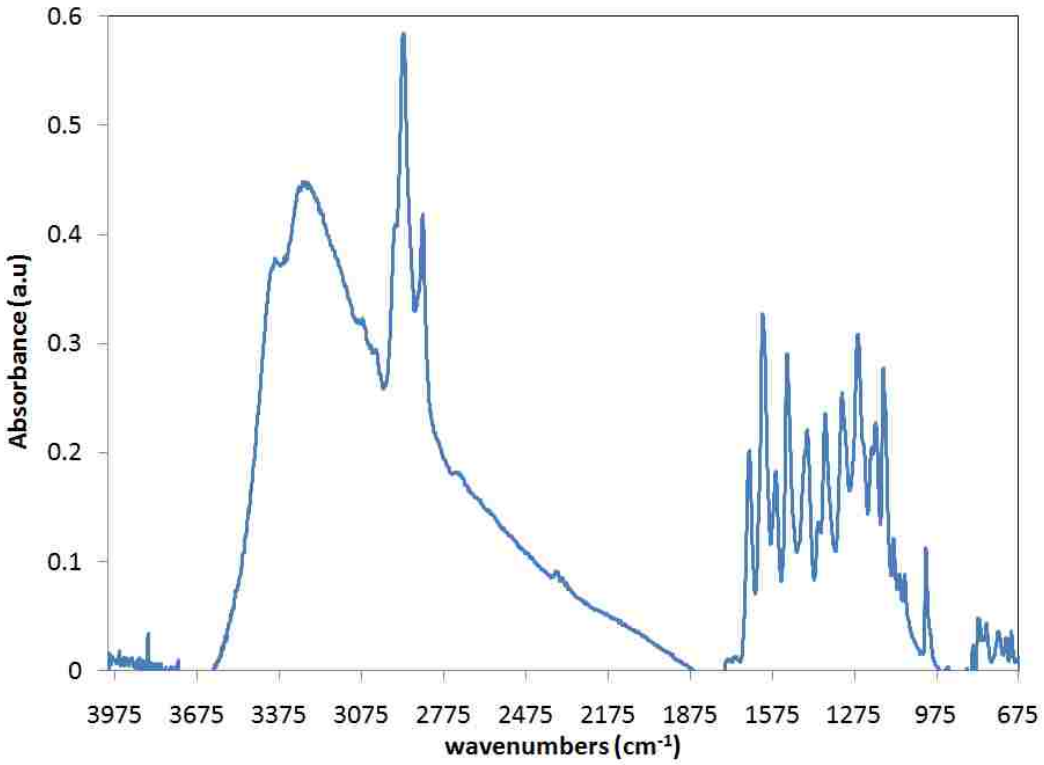

Figure 3.3 Infrared absorption spectrum of quercetin powder. Spectrum was taken using a single reflectance ATR cell.

Fig.3.4 shows the 1700-900 cm^{-1} region of the spectrum shown in Fig.3.3. The full assignment of the bands for the spectrum is given in Table 3.1. Marked bands in Fig.3.4 represent quercetin bands that were used to monitor the diffusion process. Solimani[104] reported that the carbonylic stretching appearing at 1666 cm^{-1} is an expected value for cyclic, conjugate (and planar) systems such as benzopyranic-4-one structure.

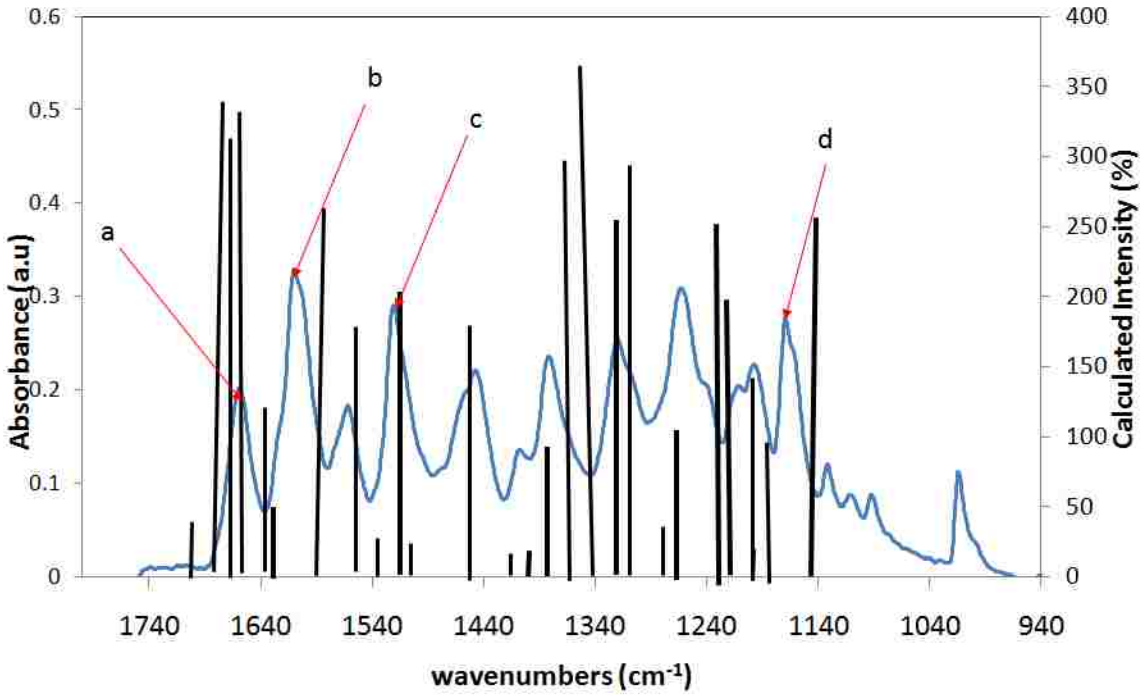

Figure 3.4 Fingerprint region (1800-940 cm^{-1}) of the IR absorption spectrum of quercetin powder on a single ATR cell showing a) carbonyl peak at 1666cm^{-1}, b) C=C peak at 1610cm^{-1} c) benzene ring vibration absorption peak at 1520 cm^{-1} and d) C-O-C antisymmetric stretch at 1197cm^{-1}. The stick spectrum represents the gas phase calculation of the Infrared spectrum in the range 1800 cm^{-1} to 940 cm^{-1}

In Table 3.1, the first column represents the peak positions for quercetin that were observed from ATR-FTIR spectroscopy. The second column represents calculated gas-phase Infrared absorption bands. The geometry of quercetin was optimized using DFT theory with a B3LYP/6-311 G(d,p) method using Gaussian 03. The band assignments were adopted from Cornard and coworkers.[103] The bond lengths of the optimized geometry are presented in Table 1 in Appendix B.

Table 3.1 Infrared absorption band assignments

Observed	Calculated	Assignment (reference 103)
3278	3490	*v*(O7-H7) *v*(O5-H5) *v*(O3-H3) *v*(O15-H15)
2971	3100	*v*(C6-H6), *v*(C8-H8)
2851	3152	*v*(C16-H16) *v*(C13-H13)
1662	1659	*v*(C=O)
1611	1637	*v*(C2=C3)
1562	1553	8b(B), 8a(A)
1520	1509	8a(A), 8b(B)
1447	1453	*v*(C7-OH) 19a(A)
1381	1308	σ (C3-OH), *v*(O1-C2), *v*(C3-C4)
1263	1268	14(B), *v*(O1-C2), *v*(C3-O3) *v*(C3-C4)
1197	1188	14(A),), *v*(O1-C2), **Δ(**C2-C3-C4), **Δ(**C2-C3-C4),

3.3.2 ATR-FTIR spectra of quercetin-ethanol solution.

Fig. 3.5 shows the spectrum of ethanol and quercetin obtained by averaging 40 scans at a resolution of 2 cm^{-1}. Trace (a) shows the spectrum of ethanol solution obtained on a

single reflectance ATR cell. Trace (b) shows the result of subtracting the spectrum of quercetin-ethanol solution subtracted from an ethanol background spectrum. The concentration for quercetin in ethanol was $8x10^{-3}$ M.

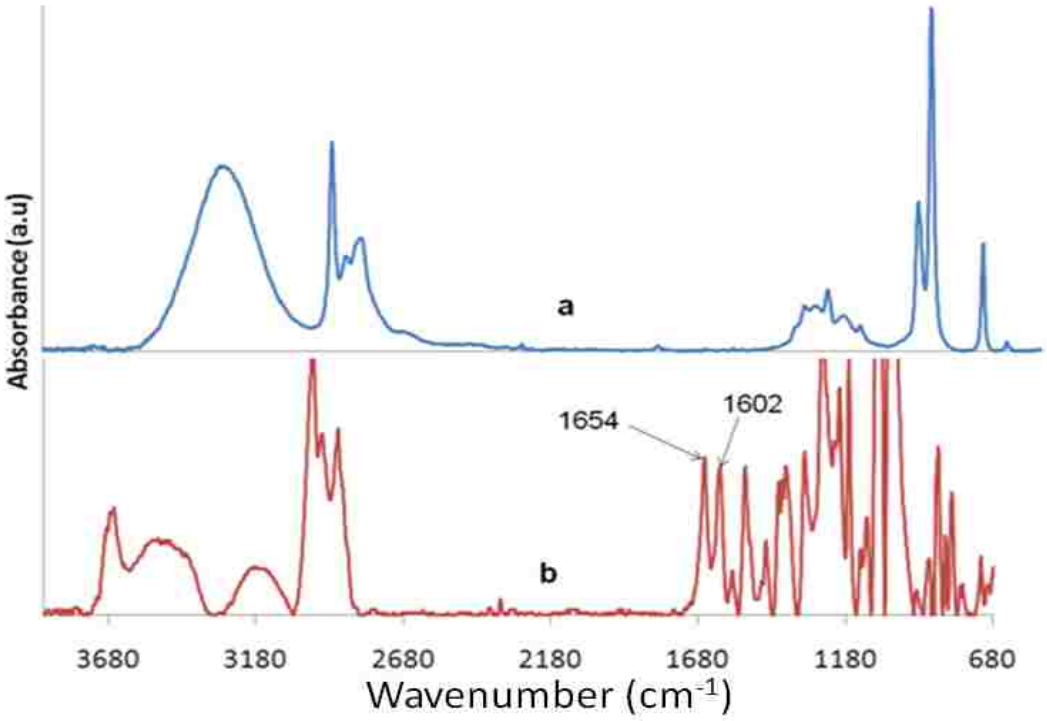

Figure 3.5 ATR-FTIR spectrum of ethanol (a) obtained using a bare ATR as the background and quercetin solution (b) obtained using ethanol as the background.

Trace (a) in Fig 3.5 shows that ethanol is infrared-transparent in the 1700 -1500cm^{-1} region. This suggests that quercetin infrared bands at 1654 cm^{-1} and 1602 cm^{-1} can be observed without interference from the solvent bands. Spectrum b shows a broad absorption band centered at 3150 cm^{-1}, which has been assigned to polymeric O-H band of the flavonol, whereas the broad band at 3500 cm^{-1} is attributed to a dimeric association

of quercetin.[104] In general the spectral profile of the 'fingerprint' region in trace (b) presents, as expected, red-shifted bands for the quercetin-ethanol solution with respect to the quercetin powder spectrum in Fig. 3.4. This observation is summarized in Table 3.2

Table 3.2 Summary of the bands that show red-shifting as a result of dissolving quercetin in ethanol

Band	Quercetin powder (Fig 3.4)	Quercetin-ethanol solution (Fig 3.5)
v(C=O)	1666 cm^{-1}	1654 cm^{-1}
v(C2=C3)	1610 cm^{-1}	1602 cm^{-1}
v(O7-H7) *v*(O5-H5) *v*(O3-H3)	3263 cm^{-1}	3157 cm^{-1}
8a(B) 8a(A)	1560 cm^{-1}	1560 cm^{-1}
8a(A), 8b(B)	1517 cm^{-1}	1517 cm^{-1}

Table 3.2 shows that the solution carbonyl and hydroxyl bands show significant shift from the powder bands presumably due to hydrogen bonding with the solvent. There is no significant shift of the benzene vibration modes at 1560 cm^{-1} and 1517 cm^{-1}.

3.3.3 Interaction of quercetin solution with polymer films

The polymer systems chosen for evaluating the diffusion of quercetin solution had very little absorbance in the region between 1500 and 1700 cm^{-1}. This allows unambiguous identification of the carbonyl as well as the C=C bond stretching frequency for quercetin around 1658 cm^{-1} and 1610 cm^{-1} respectively. Fig.3.6 shows the spectrum of quercetin in polymer films in the range 1800 cm^{-1} to 950 cm^{-1}.

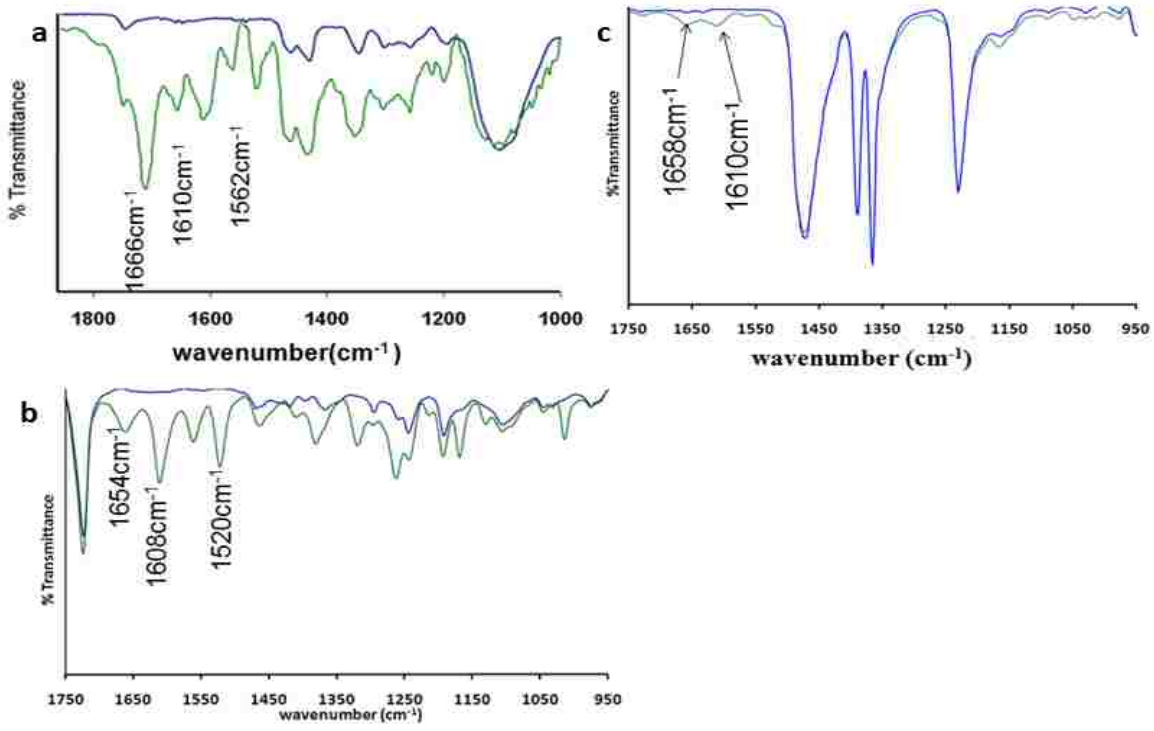

Figure 3.6 Infrared spectra of quercetin in PCL (a) PECH (b) PIB (c). The spectrum for quercetin is shown in green. The spectra for the polymers are shown in blue. Labeled peaks represent quercetin peaks that do not interfere with polymer infrared bands. The labeled peaks were used to identify quercetin in polymer films.

Traces (a) to (c) indicate that the bands for quercetin in the range 1650 cm^{-1} to 1450 cm^{-1} can be unambiguously assigned to quercetin in the polymer films. This observation, along with results in Fig. 3.5 suggest that infrared spectroscopy can be used to monitor the diffusion of quercetin-ethanol solution in PECH, PIB and PCL using the absorption bands at 1604 cm^{-1} or 1650 cm^{-1}. The glass transition temperatures, Tg, of PECH, PIB and PCL are -22 ^{0}C, -76 ^{0}C, -60 ^{0}C respectively as reported by the manufacture. When the operating temperature is above the Tg, polymers are in their rubbery state. The diffusion experiments were performed at room temperature. This means that at the experimental temperatures the polymers are rubbery and amorphous allowing faster diffusion. Small molecules have been reported to diffuse faster in rubbery amorphous polymers than in glassy crystalline polymers.[105]

3.3.4 Diffusion of quercetin in polymer films

The diffusion of quercetin solution into polymer films was monitored using ATR-FTIR spectroscopy. Fig. 3.7 shows the time resolved infrared absorption spectra of quercetin-ethanol solution in a PECH film. It can be observed that the OH stretching band in centered at 3300 cm^{-1} shows distinct absorbance increases with time indicating the sorption of quercetin-ethanol solution in PECH. However, due to overlap of the quercetin bands and ethanol bands in this region, the region between 1500 cm^{-1} and 1700 cm^{-1} was used to monitor the diffusion of quercetin into the film.

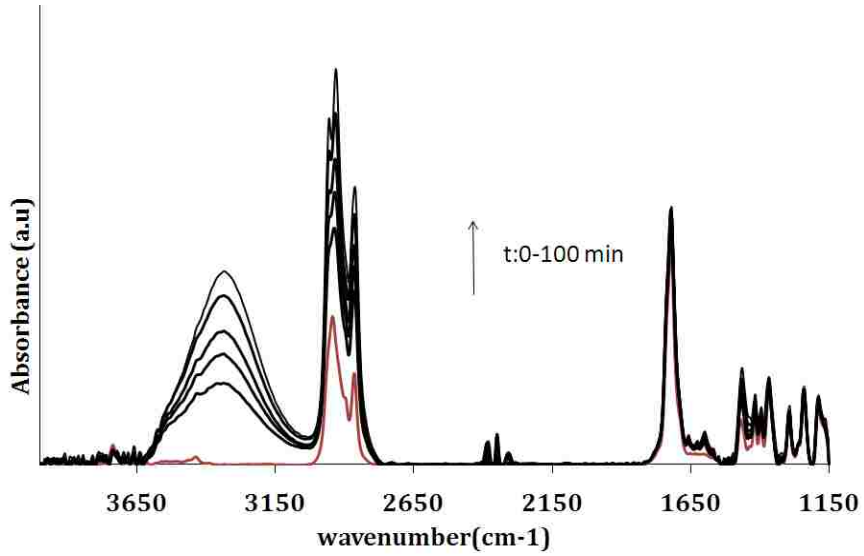

Figure 3.7 Temporal changes of the ATR-FTIR spectra of quercetin-ethanol solution in PECH film in the wavenumber range 400-1150 cm^{-1} during the sorption process. Only spectra collected at 10 minute intervals are shown for clarity. The bottom trace (in red) represents PECH spectrum and the black traces represent quercetin solution in PECH film at different times

Fig. 3.8 is an expanded view of the spectral region between 1650 cm^{-1} and 1490 cm^{-1} shown in Fig. 3.7. In this region the quercetin infrared bands can be unambiguously distinguished from both the PECH bands and ethanol bands.

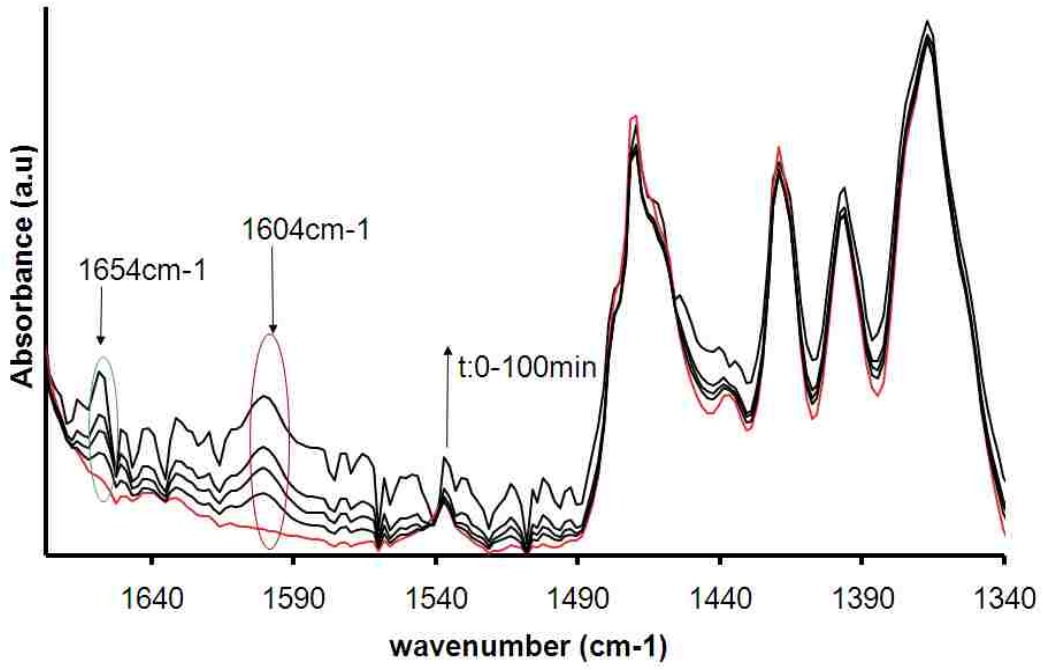

Figure 3.8 Temporal changes of the ATR-FTIR spectra of quercetin-ethanol solution in PECH film in the wavenumber range 1650-1340 cm^{-1} during the diffusion process. The red circle shows the temporal changes of the C_2=C_3 stretching frequency for quercetin at 1604 cm^{-1} and the green oval represents the temporal changes of C=O band of quercetin at 1654 cm^{-1}

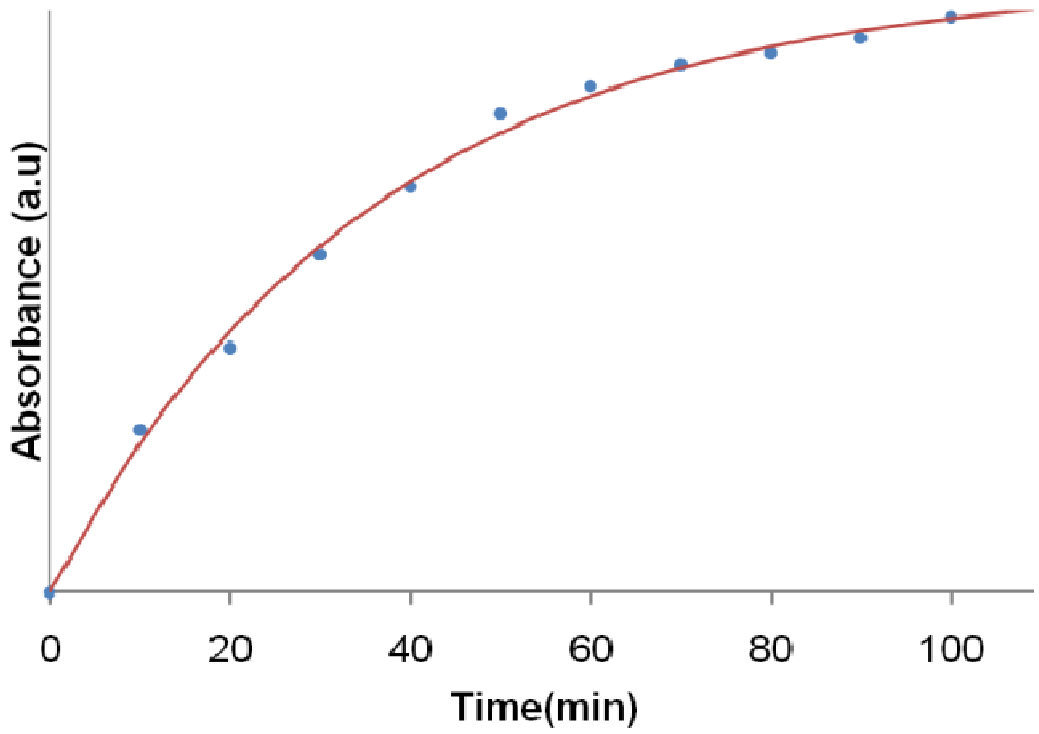

Figure 3.9 Temporal changes of the 1608 cm^{-1} band of quercetin solution in PECH. Solid line represents an exponential fit to the experimental data.

A plot of the absorption intensity as a function of time for the band at 1604 cm^{-1} in Fig.3.8 is shown in Fig. 3.9. It can be observed from Fig. 3.9 that during the sorption process, the band intensity increase steadily until it reaches a steady-state, presumably when the film is saturated with quercetin solution. Similar trends were obtained for the diffusion of quercetin solution in PIB and PCL and a typical absorption process in all three polymer films lasted for a period between 80 and 100 minutes. Fig. 3.9 to Fig. 3.11 shows the temporal changes of the absorbance of quercetin in PECH, PCL and PIB. The time dependent intensity plots were fit to exponential growth equations.

The parameters for the exponential equation used to fit the data in Fig. 3.9 are summarized in Table 3.4 y_0 represents the absorbance at equilibrium, t_1 is the time constant for the exponential curve.

Table 3.3 Parameters for the exponential fit for the diffusion of quercetin in PECH

Equation	$y = A_1 * \exp(-x/t_1) + y_0$		
χ^2	1.52×10^{-3}		
R^2	0.998		
	Parameter	Value	Standard Error
	y_0	0.125	0.002
	A_1	-0.126	0.001
	x_1	12.01	0.04

Fig.3.10 shows time dependent intensities of the 1608 cm^{-1} absorption band of quercetin in a PCL film on an ATR prism.

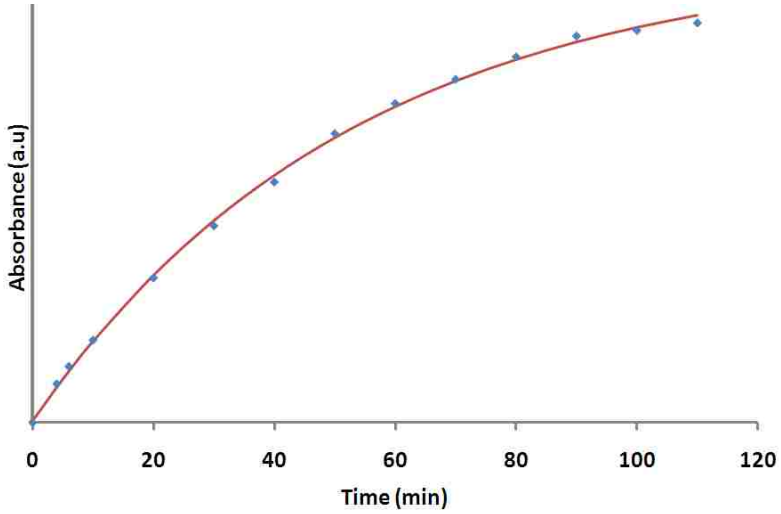

Figur 3.10 Temporal changes of the 1608 cm $^{-1}$ absorption band of quercetin solution in PCL. The solid line represents an exponential fit to the experimental data used to estimate the absorbance at equilibrium, A_∞

The parameters for the exponential equation used to fit the experimental data for the sorption of quercetin in PCL are summarized in Table 3.4.

Table 3.4 Parameters for the exponential fit for the diffusion of quercetin in PCL

Equation	$y = A_1 * \exp(-x/t_1) + y_0$		
χ^2	1.328×10^{-4}		
R^2	0.999		
	Parameter	Value	Standard Error
	y_0	0.166	0.001
	A_1	-0.156	0.03
	x_1	24.23	0.08

The time dependent variation of the 1601 cm^{-1} absorption band for quercetin in PIB is shown in Fig.3.11

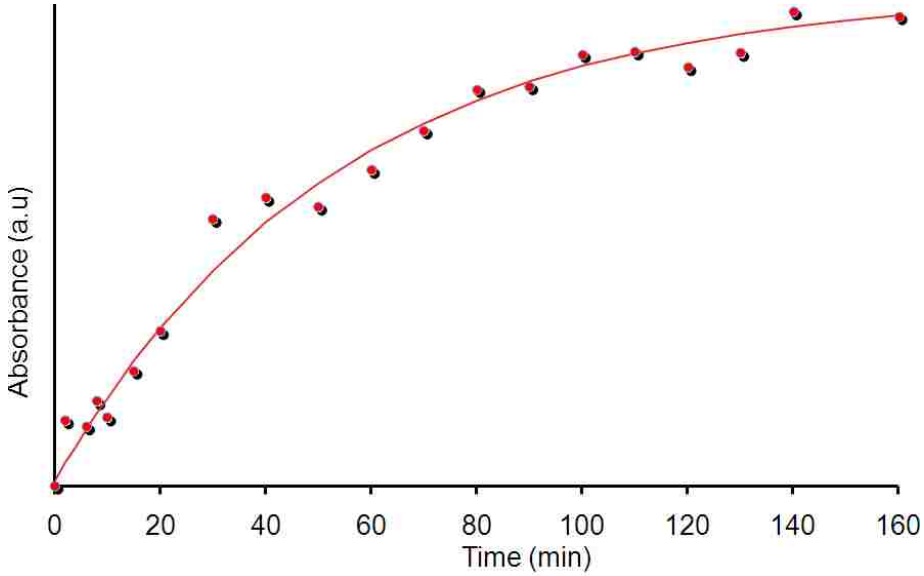

Figure 3.11 Temporal Changes of the intensity of the 1601 cm^{-1} quercetin peak during the diffusion in PIB. Solid line represents exponential fit to experimental data

The parameters for the exponential equation used to fit the experimental data for the diffusion of quercetin in PIB are summarized in Table 3.5.

Table 3.5 Parameters for the exponential fit for the diffusion of quercetin in PIB

Equation	$y = A_1 * \exp(-x/t_1) + y_0$		
χ^2	1.3281×10^{-6}		
R^2	0.982		
	Parameter	Value	Standard Error
	y_0	0.0728	0.0002
	A_1	-0.0715	0.0003
	t_1	7.89	0.01

3.3.5 Estimation of Diffusion coefficients

ATR-FTIR spectroscopy has been widely used to study the molecular diffusion in polymer.[106-111] The diffusion of small molecules in polymer films is classified into three types.[112] These types are distinguished by the shapes of the plots of $\frac{A_t}{A_\infty} = f(t)$ where A_t is the absorbance at time *t* and A_∞ is the absorbance at equilibrium. The linear portions of these plots can be fit to an empirical equation $\frac{A_t}{A_\infty} = kt^n$ where equilibrium *k* is a structural characteristic of the polymer chains, and *t* is time while *n* is used to determine the mode of the penetrant transport. The diffusion mode is classified as case I if $n \leq 0.5$, case II if n=1 and case III if $0.5<n<1$. The diffusion process is considered to be case I when the rate of polymer relaxation is faster than the rate of molecular diffusion, while case II occurs when the rate of diffusion occurs faster than the rate of polymer relaxation

during the diffusion. The diffusion process is considered to be case III if the rate of polymer relaxation is comparable to the rate of molecular diffusion.[105] As a general rule case I occurs in elastomeric polymers while case II occurs with glassy polymers.[40,105,113] The experimental data for the 3 polymer films were fit to the empirical equation $\frac{A_t}{A_\infty} = kt^n$. Table 3.6 summarizes the *n* values obtained from fitting the experimental data to the empirical equation.

Table 3.6 Estimated equilibrium absorbance and n values for Fickian diffusion

	Parameter	
Polymer	A_∞	n
Polyepichlorohydrin (PECH)	0.125	0.28 ± 0.02
Polycaprolactone (PCL)	0.166	0.48 ±0.04
Polyisobutylene (PIB)	0.0728	0.50±0.01

In Table 3.6, A_∞ values from the experimental data to exponential curves as explained in section 3.3.4. Errors in *n* values represent regression error analysis. Values of *n* are ≤ 0.5 confirming case I (Fickian) mode of diffusion. Diffusion coefficients for quercetin in PECH, PCL and PIB were estimated using the equation derived by Fieldson and Barbari[113] for the diffusion of small molecules in polymers shown in equation 3.2 below

$$\ln(1-\frac{A_t}{A_\infty}) = \ln(\frac{4}{\pi}) - \frac{D\pi^2}{4L^2}t \qquad 3.2$$

Where A_∞, A_t and t were defined earlier, L is the film thickness, and D is the diffusion coefficient. A plot of $\ln(1-\frac{A_t}{A_\infty})$ versus time, t results in a linear plot with slope $\frac{-D\pi^2}{4L^2}$.

Fig.3.12 shows linear plots of equation 10 used for estimating the diffusion coefficients.

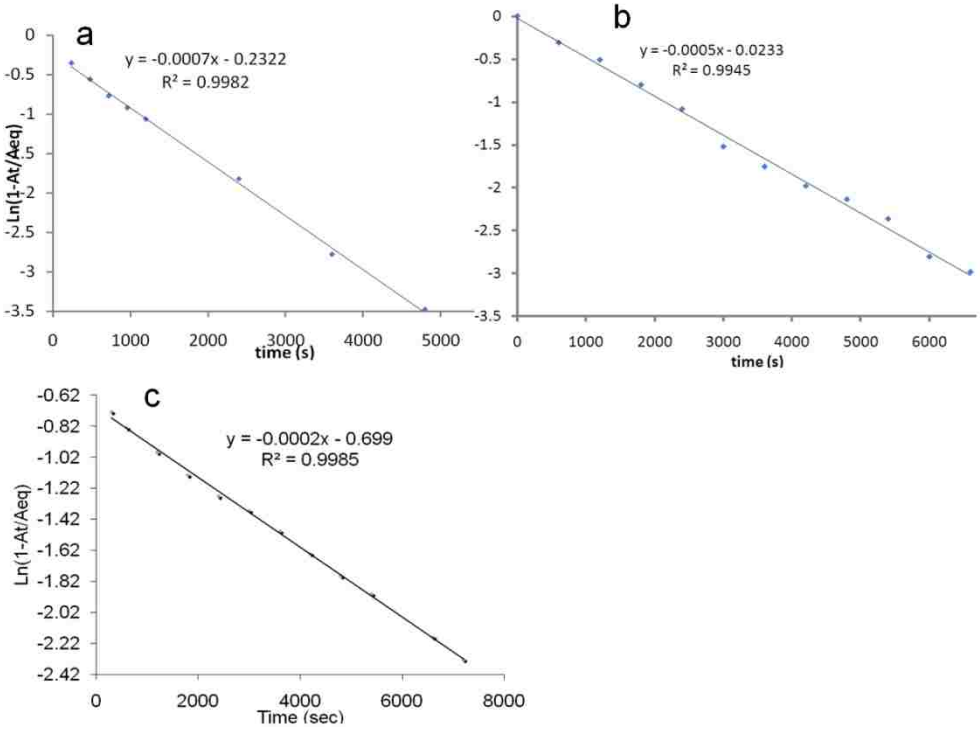

Figure 3.12 Linear plots of equation 5 for the diffusion of quercetin in a) PCL, b)PECH c) PIB. The R^2 values close to unity show goodness of fit. Slope values are used to calculate D.

Table 3.7 calculated diffusion coefficients of quercetin solution in the polymer films used in this study

	PCL	PECH	PIB
D (x 10^{-9} cm^2/s)	2.145±0.003	0.027±0.005	0.009±0.008
[1]A_∞	0.166±0.002	0.125±0.001	0.0728±0.0002
[2]L (cm)	0.00275	0.00115	0.00034

[1] values obtained by fitting experimental data to an exponential equation.

[2] L, thickness was calculated using published polymer density data and the dimensions of the ATR prism

Calculated diffusion coefficients in Table 3.7 suggest that the sorption rate is fastest in PCL, followed by PECH and slowest in PIB. It is postulated that the differences in polarity among the functional groups in PECH, PIB and PCL have a significant contribution in the differences in diffusion of quercetin solution in these polymers. The chemical structures of the monomers of PECH, PIB and PCL are shown in Fig. 2.3. It can be assumed that the carbonyl group in PCL as well as the oxygen atom may participate in hydrogen bonding with quercetin resulting in a faster diffusion than what is observed in PIB or PECH. Dipolar and hydrogen bonding interactions between the hydroxyl group of quercetin and the Cl-C-H segment of PECH are also expected to increase the diffusion of quercetin into PECH.

The diffusion coefficient of quercetin solution is also affected by the interaction of the solvent used to dissolve quercetin with the polymer films. To this end the diffusion of ethanol (95 %), the solvent used to dissolve quercetin, was studied using literature

linear solvation energy relationships (LSER) as well as experimental observation from time dependent FTIR experiments. Grate and coworkers[15] have characterized a group of polymers (including PECH and PIB) using LSER. Table 3.8 shows LSER regression coefficients for PECH and PIB. The solute vapor parameters for a number of vapors including ethanol (which was used as the solvent in this work), have been reported. [1, 15] We used these literature parameters reported in Table 3.8 to estimate the partition coefficient of ethanol in PECH and PIB.

Table 3.8 LSER regression coefficients for PECH and PIB at 25°C (adapted from ref 15)

Polymer	Constant c	Polarizability r	Dipolarity s	Hydrogen-bond basicity, a	Hydrogen-bond acidity	Dispersion and cavity, I
PECH	-0.75	0.10	1.63	1.45	0.71	0.83
PIB	-0.77	-0.08	0.37	0.18	0.00	1.02

The size and magnitude of all the coefficients are used to identify polymers with high selectivity and sensitivity as coatings for chemical sensors. The difference between PIB and PECH in Table 3.8 is in r, s, a and b which represent the polarizability, dipolarity, hydrogen bond basicity and acidity of the polymers. The observed differences in diffusion coefficients between PECH and PIB reported in Table 3.7 could be attributed to the LSER coefficients differences shown in Table 3.8. Based on these values and solute

vapor solvation parameters for ethanol

($R_2 = 0.246, \pi_2^H = 0.42, \alpha_2^H = 0.37, \beta_2^H = 0.48, LogL^{16} = 1.485$) reported by McGill and coworkers,[13] we calculated the Log K_p values for ethanol in PECH and PIB. The calculated Log Kp values are 2.069 and 0.947 for PECH and PIB respectively. Although these values are for the vapor phase, we can infer that for equivalent concentrations, ethanol solution will partition much more strongly in PECH than in PIB. The calculated diffusion coefficients for ethanol in PCL, PECH and PIB obtained in this study using the same procedure as for quercetin reported earlier are summarized in Table 3.9. The diffusion of ethanol was monitored using the OH stretching band at 3350 cm^{-1}.

Table 3.9 Calculated diffusion coefficients of ethanol in the polymer films

	PCL	PECH	PIB
D (x 10^{-9} cm^2/s)	4.3(±0.3)	3.22(±0.03)	1.4(±0.5)
$^1A_\infty$	0.32(±0.04)	0.54(±0.01)	0.175(±0.003)
^2L (cm)	0.00275(±0.00002)	0.00115(±0.00001)	0.00034(±0.00003)

The diffusion coefficients in Table 3.9 show the same trend as for the diffusion of quercetin presented in Table 3.7.

The calculated Log Kp values for ethanol correlate well with the diffusion coefficients obtained for the sorption of ethanol in PECH and PIB found in this study. It

can be inferred from the Kp values obtained for ethanol in PECH and PIB that the partition coefficient of quercetin dissolved in ethanol will be higher for PECH than for PIB. We could not calculate the LSER parameters for quercetin because the experiments involved are beyond the scope of this study. Molecular dynamic simulations would be useful in characterizing the polymer/quercetin interactions.

3.3.6 Detection of quercetin using PECH and PIB coated QCM sensors

A 5 MHz quartz crystal microbalance was used to study the response of PECH and PIB coated device to the concentration of quercetin in ethanol. The results of the ATR-FTIR diffusion experiments showed that quercetin diffuses faster in PECH than in PIB. Based on the ATR-FTIR results it was assumed that the sensitivity of a PECH coated device to quercetin solution would be greater than for a PIB coated device for the same quercetin concentration.

Fig. 3.13 shows sensor response (frequency shift) for a QCM sensor coated with 0.8 μm thick PECH film exposed to 76 to 304 ppm quercetin-ethanol solution. The reversible nature of sensor response indicates that analyte/coating interaction is reversible. As a result, the present sensor will be reusable. The baseline drift for the data shown in Fig.3.13 was corrected by connecting the points where analyte absorption starts, with a straight-line.

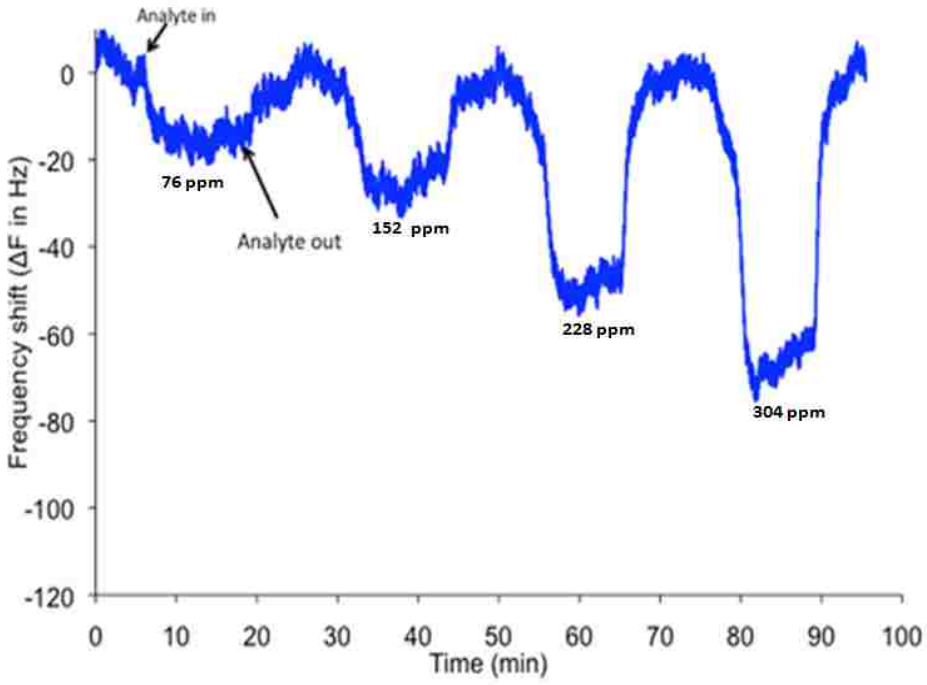

Figure 3.13 Measured Frequency shifts in the detection of 76 ppm to 304 ppm quercetin using a 0.8 µm thick PECH film on a QCM sensor. The flow rate of quercetin solution was 0.24 ml/minute. The response and recovery times were 54 and 58 seconds respectively

The corresponding resistance change of the QCM is shown in Fig.3.14. Resistance change represents the ohmic resistance that occurs inside the metal electrodes as a result of the change in the frequency of the acoustic wave. It is interesting to note that the resistance change shown in Fig.3.14 is complementary to the Frequency shift shown in Fig.3.13. This suggest that these two parameters can be used to transduce the changes occurring on the device to a signal that can be related to the analyte concentration

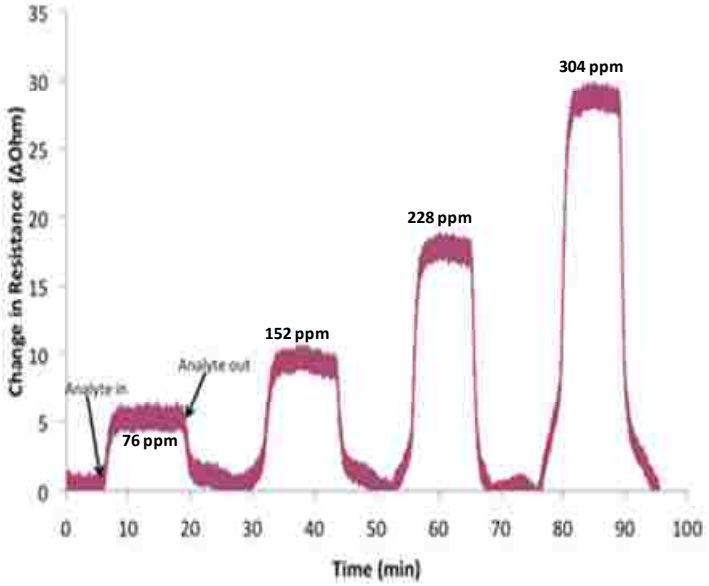

Figure 3.14 Measured resistance shifts in the detection of 75 ppm to 304 ppm quercetin solution using a 0.8 μm thick PECH film on a QCM device sensor. The flow rate of quercetin solution was 0.24 ml/minute. The response and recovery times were 54 and 58 seconds respectively

The sensor response time is defined as the time it takes for the associated change (resistance or frequency) to reach 90 % of the steady-state value. Within the concentration range shown in Fig. 3.13 and 3.14, the response time was about 1 minute. The sensor response of a 0.8 μm PIB coated device is shown in Fig.3.15.

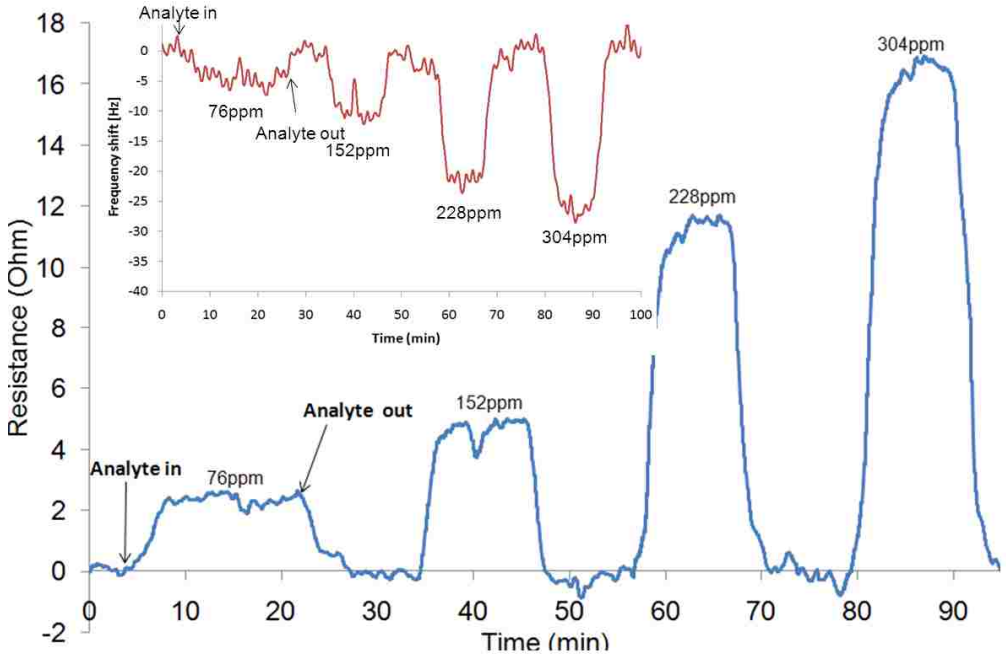

Figure 3.15 Resistance and Frequency shifts (insert) of a PIB coated QCM upon exposure to varying quercetin concentration indicated. Film thickness was 0.8 μm. Gate interval was 1 s. Solution flow rate = 0.2ml/min.

Fig.3.13 to Fig.3.15 shows that both resistance shift and frequency shifts can be used to detect for the presence of quercetin in solution. This can allow for development of a sensor that is capable of multi-parameter analysis. The amount of analyte absorbed within a given time on a PECH coated QCM is twice the amount adsorbed by a PIB coated device. This can be observed if we consider for example the frequency shift associated with a quercetin concentration of 228 ppm. The change in frequency for a PECH coated device is 53 Hz while for a PIB coated device the change is 28 Hz. The same trend is observed in resistance shifts.

The time-dependent response of QCMs is characteristic of specific analyte-polymer coating interactions. Frequency-time response profiles shown in Fig.3.14 and Fig.3.15 are evaluated with respect to rise time constant and decay time constant.[31] Time constants (τ) are obtained from fitting the data to exponential functions shown in equation 3.3.and 3.4. The minimized function is the sum of squared difference between the experimental data and the theoretical values at the same time. The optimization parameters for the response times are the baseline value (A_0) of the response, the relative response value i.e the steady state frequency value (A_1) and the time constant τ

Exponential growth fitting: $y = A_o + A_1(1 - e^{-t/\tau})$ 3.3

Exponential decay fitting $y = A_1 e^{-t/\tau}$ 3.4

The calculated time response for the sensor responses for data in Fig.3.14 and Fig.3.15 are presented in Table 3.10 and Table 3.11.

Table 3.10 Time constants for sorption of quercetin onto PECH coated QCM devices

Concentration (ppm)	Rise time (seconds)	Decay time (seconds)
76	58.4±2.1	55.6±4.8
152	56.3±3.2	58.6±5.3
224	56.3±2.4	68±3
304	54.5±3.8	76±4

The average rise time constants in Table 3.10 indicate a general decrease with increasing concentration. This is consistent with a sorption process that is driven by a concentration gradient. As the concentration increases the sorption rate increases and the rise time is expected to decrease. The decay times, which represent the time it takes to remove the quercetin from the film, increase with the initial concentration of quercetin. This indicates that at higher concentrations more quercetin would have been adsorbed and it takes more time to remove the quercetin from the film. The time constants for the sorption of quercetin onto a PIB coated QCM are presented in Table 3.11. The average rise time constants decrease with increasing quercetin concentration. The decay time constants increase with increasing quercetin concentration, suggesting that it takes more time to remove the quercetin at higher concentration.

Table 3.11 Time constants for sorption of quercetin onto PIB coated QCM sensor

Concentration (ppm)	Rise time (seconds)	Decay time (seconds)
76	62±1.5	54±3
152	63±4	61±5
224	57.8±3.2	64±3
304	59.5±2.9	68.2±4.2

The rise times presented in Table 3.10 and Table 3.11 show that on average the sorption process is faster on a PECH coated device than on a PIB coated device. These time constants are consistent with what was reported for the diffusion of quercetin in section 3.3.5, where the diffusion coefficient of quercetin in PECH was an order of magnitude higher than in PIB. However, the desorption rate as represented by the decay times in Table 3.10 and Table 3.11, is faster in PIB than in PECH. This suggests that it is easier to desorb quercetin from a PIB film than from PECH film. The rise times provide means of evaluating the relative sensitivities of the polymer coatings.

The sensitivity of the analyte can be evaluated using the slope from the plot of the sensor response such as frequency shift or resistance shift as a function of the analyte concentration, $\Delta R/\Delta C$[114] where ΔR is the change in resistance and ΔC is the change in analyte concentration. The change in resistance as a function of quercetin concentration for PIB and PECH coated QCM sensors is shown in Fig.3.16.

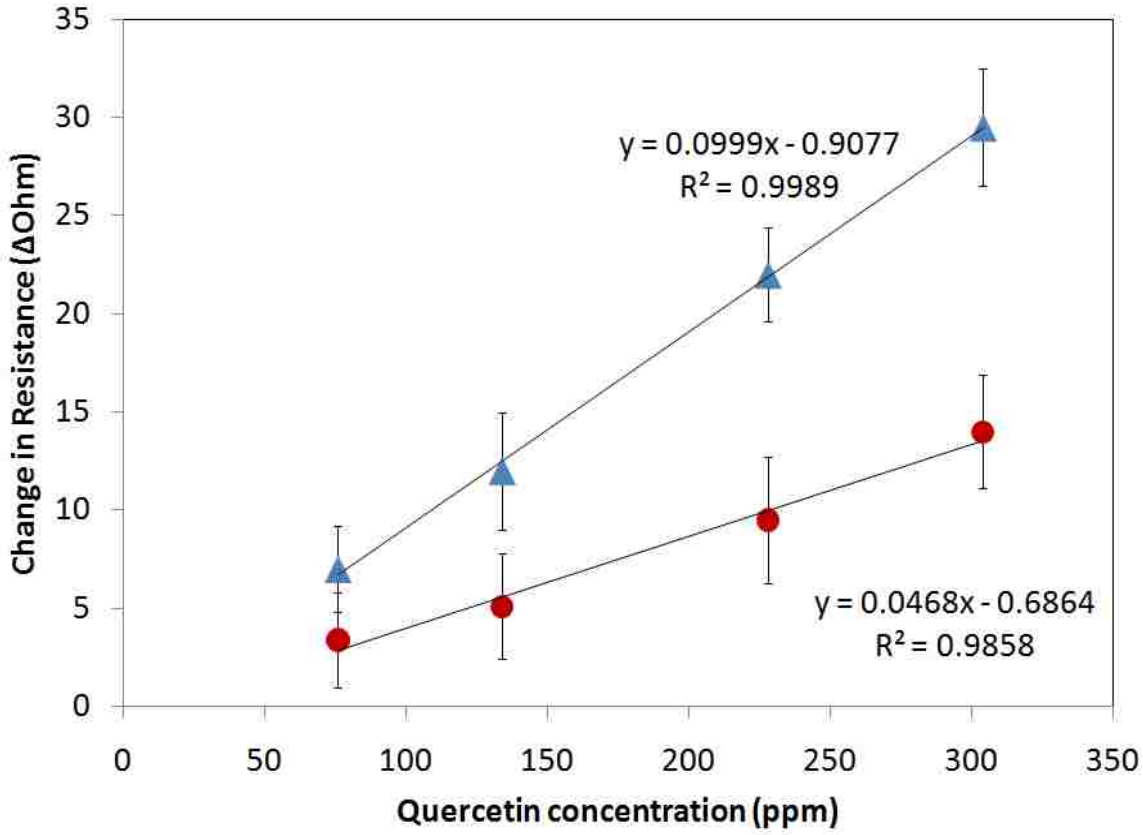

Figure 3.16 Resistance shifts as a function of concentration for PECH (blue triangles) and PIB (red circles)

The slopes of the plots shown in Fig.3.16 indicate that the PECH coated device is more sensitive to quercetin than a PIB coated device. The trend in sensitivity values is in reasonable agreement with the trend in rise times for both PECH and PIB. The slope for PIB coated device suggests that the resistance changes by about 0.1 Ohm for one ppm of quercetin adsorbed on the device. The resistance changes by 0.05 Ohm for every 1 ppm of quercetin adsorbed when the device is coated with PIB film. These resistance changes suggest that the two polymers are not suitable for detecting quercetin concentrations below the concentration ranges shown in Fig.3.16.

In order to improve the sensitivity of the sensor we used a Bisphenol A-

hexamethyltrisiloxane (BPA-HMTS) polymer that we synthesized using a published procedure.[27] In choosing this polymer we considered the potential hydrogen bonding and π-π interactions between the Bisphenol A monomer and quercetin. These interactions would improve the sensitivity of the QCM sensor if coated with BPA-HMTS. The sensor response of a 0.5 µm-thick BPA-HMTS film on a QCM device is shown in Fig. 3.17.

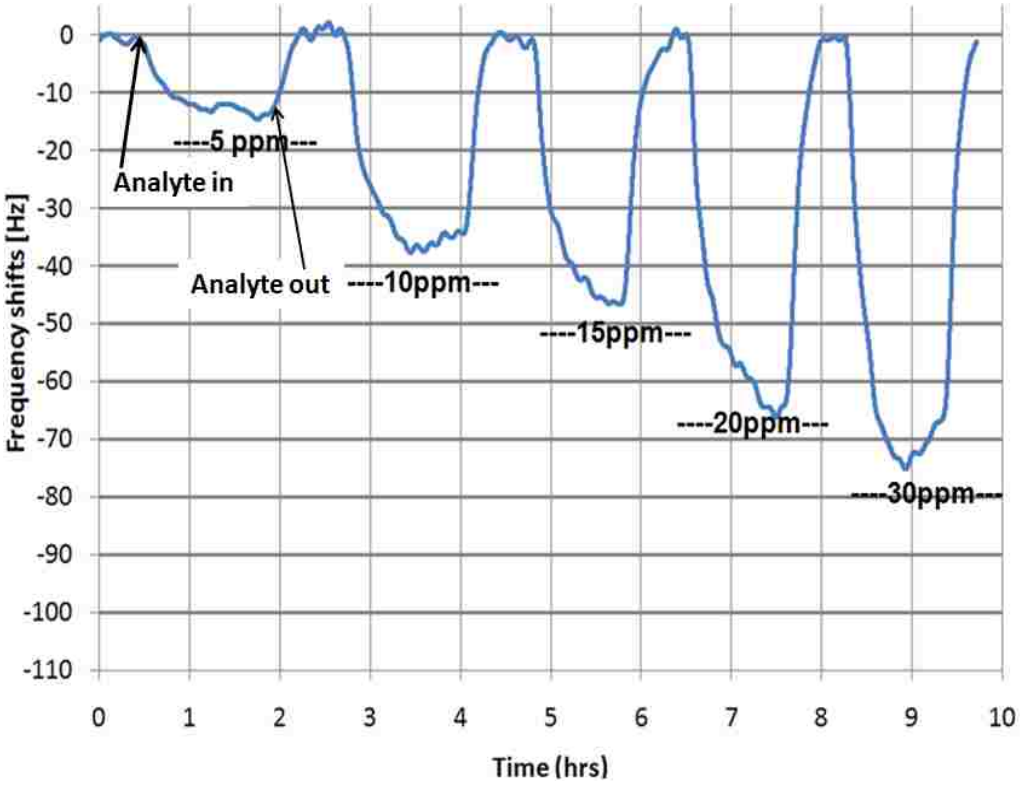

Figure 3.17. Measured frequency shifts in the detection of 5 ppm - 30 ppm quercetin using 0.5 µm thick BPA-HMTS on a QCM device

The reversible nature of sensor response indicates that analyte/coating interaction is reversible. As a result, the present sensor will be reusable. Within the measured range, the frequency shift (Δf) is linear with varying analyte concentration. Increasing the film

thickness resulted in increase in the frequency shifts for the same concentration range. Fig. 3.18 shows sensor responses (frequency shift) for a QCM sensor coated with 1 µm-thick BPA-HMTS exposed to various concentrations of quercetin (5–30 ppm)

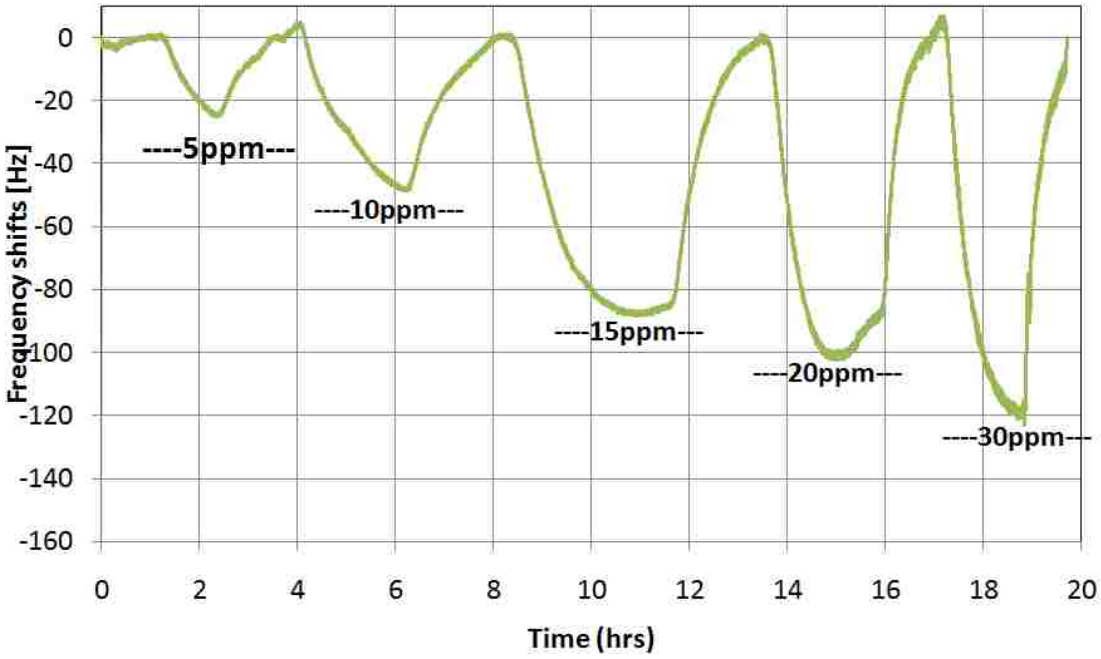

Figure 3.18 Measured frequency shift in the detection of 5 ppm -30 ppm quercetin using a 1 m thick BPA-HMTS on a QCM device

The increase in frequency shift upon increasing film thickness suggests that with a thicker film the detection limit of a given sensor platform can be improved. However, as shown in Fig.3.18, increasing the film thickness results in increase in response time. As an example Fig. 3.19 compares the response time and the frequency shift of a QCM device coated with BPA-HMTS films of different film thicknesses.

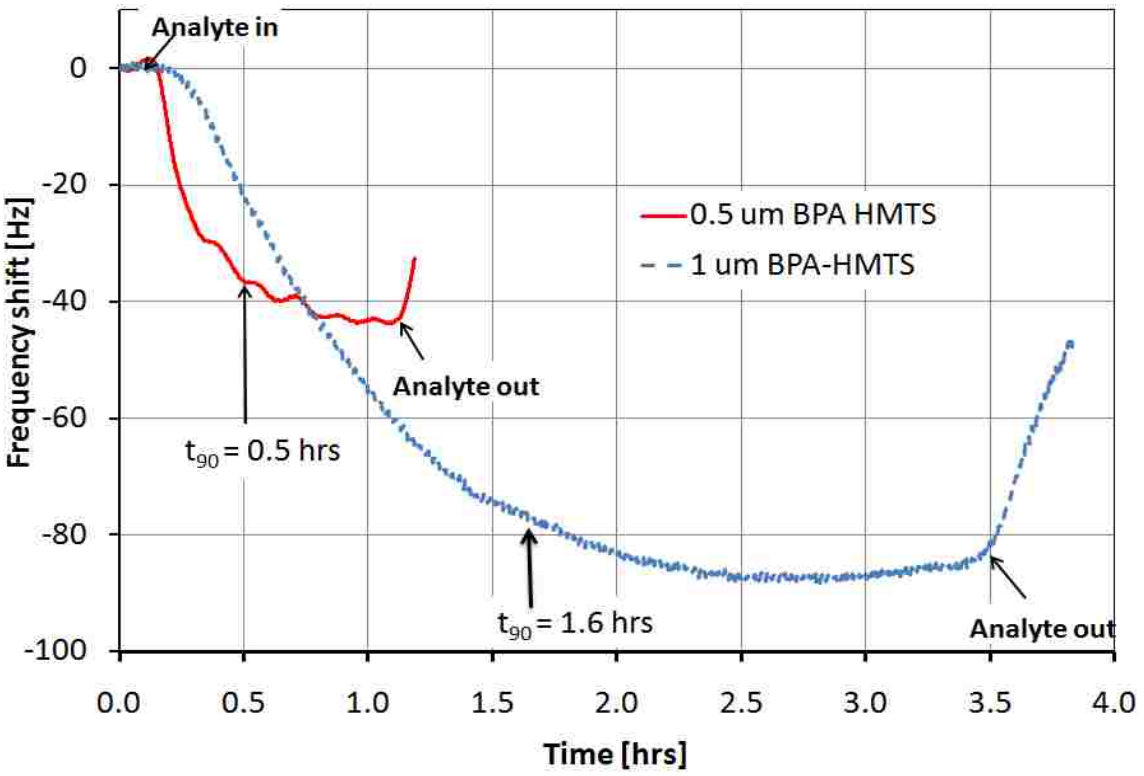

Figure 3.19 Measured frequency shifts in the detection of 15 ppm using 0.5 µm and 1 µm thick BPA-HMTS on a QCM device

The steady-state frequency shift for a 0.5 µm BPA-HMTS coated QCM exposed to 15 ppm of quercetin is 45 Hz with a response time, t_{90} of 30 minutes. For a 1 µm thick-BPA-HMTS coated device, the steady-state frequency shift is 98 Hz with a response time, t_{90} of 95 minutes.

We observed that when the film thickness was increased to 4 µm, the steady state frequency shifts increased by almost an order of magnitude with very little change in the response time. The sensor response for a QCM sensor coated with a 4 µm thick BPA-HMTS film is shown in Fig.3.20. The response time of the sensor upon exposure of 15 ppm quercetin for example is 93 minutes. The sensor response for a QCM sensor coated with a 4 µm thick BPA-HMTS film was also linear with quercetin concentration

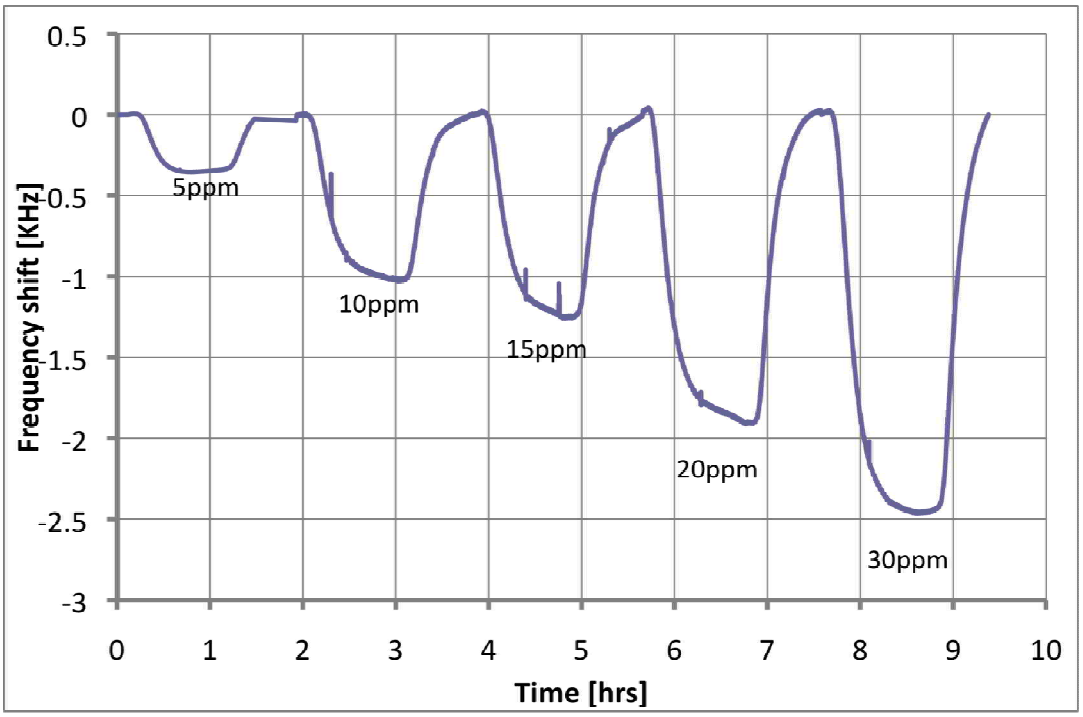

Figure 3.20 Measured frequency shifts in the detection of 5 - 30 ppm quercetin on a 4 μm thick BPA-HMTS coated QCM sensor

The sensitivity of the BPA-HMTS towards the analytes was evaluated using the relation $\Delta f/\Delta C$, where ΔC is the change in concentration. It is noted that Δf *is* determined when the response has reached steady-state upon exposure to a given concentration of analyte. Equation (3.5) is a summary of sensitivities in the present experiments.

$$\begin{aligned} \Delta f_{0.5\mu m} &= -2.35 Hz / ppm \\ \Delta f_{1\mu m} &= -3.62 Hz / ppm \\ \Delta f_{4\mu m} &= -82.7 Hz / ppm \end{aligned} \qquad 3.5$$

It is noted that upon increasing the film thickness to 4 μm, the sensitivity increases by more than an order of magnitude. This suggests that increasing the film thickness results in increase in the detection limit as more analyte is adsorbed by a thicker film

Fig.3.21 is a plot of the frequency shift as function of quercetin concentration showing the sensitivities for a 0.5 μm and 1 μm thick BPA-HMTS coated device.

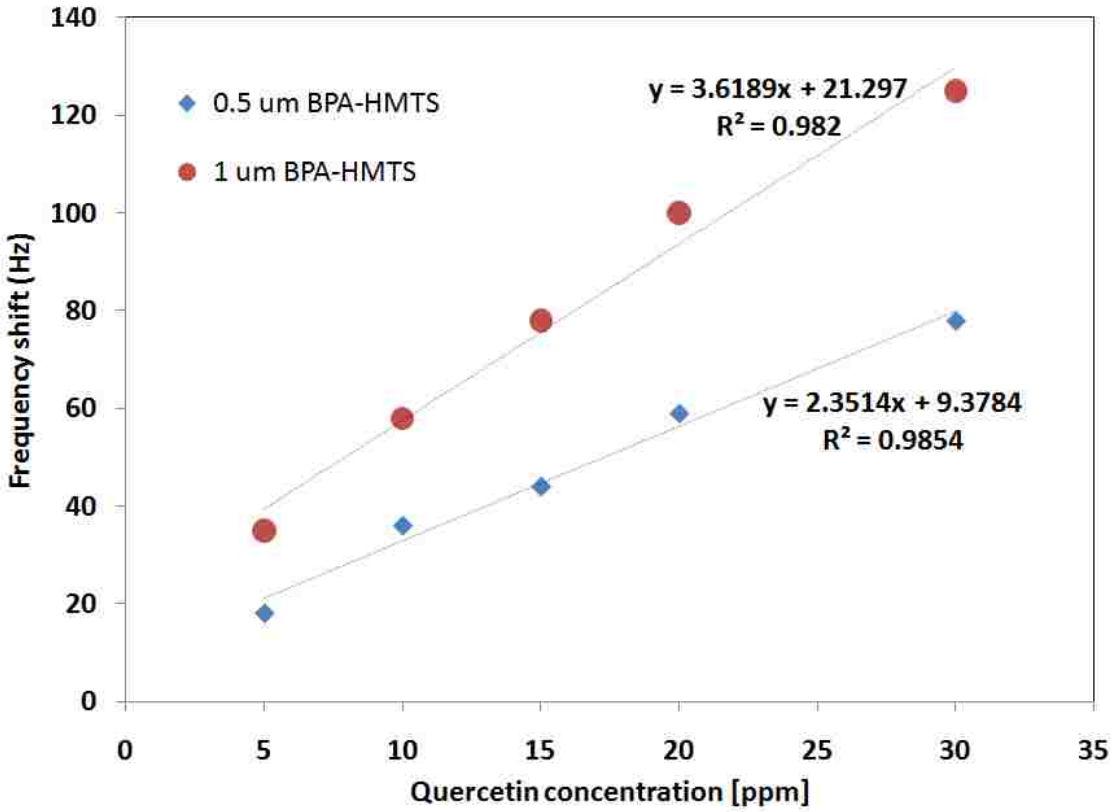

Figure 3.21 Frequency shifts versus quercetin concentrations for a 0.5 um and 1 um-thick BPA-HMTS on a QCM device. The slope of the linear plots represent the sensitvity of the device in Hz/ppm.

3.4 Conclusions

Diffusion of quercetin solution in PECH, PCL and PIB follows the Fickian mode of diffusion. Calculated diffusion coefficients for quercetin in PECH and PIB were in reasonable agreement with sensitivity values for PECH and PIB QCM coated devices. This suggests that diffusion coefficients can be used as parameters to select polymer

coatings for quartz crystal microbalance. The sensor response was linearly dependent on concentration for the concentration range studied for both PECH and PIB coated QCM. PECH and PIB coated device was not sensitive enough for quercetin concentration below 70 ppm.

(BPA-HMTS) has been synthesized and characterized for absorption of quercetin. The coating is more sensitive to quercetin than PECH and PIB. Sensitivity of BPA-HMTS coated QCM sensor increased with increasing film thickness. However, the response time increased drastically as the film thickness increased. A compromise can be reached between getting a very low detection time in a longer period and getting a poor detection limit in a very short space of time.

4 SYNTHESIS AND CHARACTERIZATION OF TERTIARY AMINE INTERCALATED A-ZIRCONIUM PHOSPHATE

Introduction

4.1.1 Intercalation of alkylamines in α-zirconium phosphate

Layered α-$Zr(HPO_4)_2$ H_2O (hereafter α-ZrP) is composed of two dimensional macromolecular units that are weakly interacting with each other.[65] α-ZrP has a clay-like structure in which octahedrally coordinated zirconium atoms are bridged by three oxygen atoms of the tetrahedral phosphate groups. The free OH groups point into the interlayer space, forming a staggered bilayer of hydroxyl groups.[115] The crystal cell of α-ZrP is pseudo-hexagonal with a = 9.076 Å, b=5.298 Å and c = 15.414 Å and β = 101.71 ^{0} and belongs to P21/c.[115] A schematic representation of the structure of α-ZrP was presented in chapter 1.

Due to its acidic nature, α-ZrP readily reacts with basic compounds such as sodium hydroxide, ammonia and alkylamines. The intercalation of aliphatic monoamines and diamines in α-ZrP has been investigated by several researchers.[64,116-118] The intercalation process is driven by an acid-base interaction between the amino group and the P-OH group of the layer.[116] Stoichiometric intercalation can occur if the cross sectional diameter of the guest molecule does not exceed the free area around the active site.[2] For example, the free area about a PO–H group in a-ZrP is 24 $Å^2$.[67,119] Because the cross-sectional area of n-alkyl chains is less than this value, a stoichiometric amount of

amine, 2 mol per formula weight, can be intercalated.[119]

Another interesting feature is the angle of inclination of the amine chains in the bilayer relative to the mean plane of the layers. This angle is influenced by the free space available to the amine. For the α-ZrP type compounds these angles are 58.7 ^{0}C for α-TiP, 60.5 ^{0}C for α-ZrP and 66 ^{0}C for α-SnP.[120] These results are in the order of decreasing free space around the metal phosphate groups. Aliphatic primary and secondary monoamines have been reported to form bilayer arrangements in the interlayer spaces of α-ZrP. This arrangement was derived from the analysis of the correlation between interlayer distance and the number of carbon atoms in the alkylamine chain.[68, 116]

Less attention has been paid to intercalation of aliphatic amines that form interdigitated arrangements in the α-ZrP interlayer spaces. Interdigitated arrangement of amines have been reported on the intercalation of aromatic amines such as toluidines and 1,5 diaminonaphthalene (1, 5 –DAN).[121] The cross sectional area of the intercalated 1,5-DAN, calculated assuming that the C-N bonds are perpendicular to the host layers, is reported to be 34.6 Å^2.[121] As the cross sectional area of the 1,5-DAN is greater than the free surface area associated with each P-OH group, there is a possibility that one 1,5-DAN molecule interacts with more than one P-OH group resulting in the ratio of the P-OH group to amino group being greater than one. This phenomena is referred to as the covering effect.[116]

The cross sectional area of primary alkylamines is reported to be 18.4 Å^2. At greater than 50 % saturation, primary alkylamine will form bilayer arrangement in the interlayer spaces of α-ZrP. The intercalation of dimethyltetradecylamine (DtDA) and dimethylhexadecylamine (DHDA) into zirconium phosphate is reported in this chapter.

The intercalation of butylamine, octylamine and hexadecylamine is presented in this chapter for the purposes of comparing with the results from the tertiary amine intercalation. It is noted here that the intercalation structure of primary amines is well established.[60,64, 68]

The structures of the alkylamines used in this study are shown in Fig. 4.1 It is noted that the major difference between the primary and tertiary amines presented in Fig. 4.1 is that the hydrogen atoms bonded to the nitrogen atom in the primary amines are replaced by methyl groups for the tertiary amine.

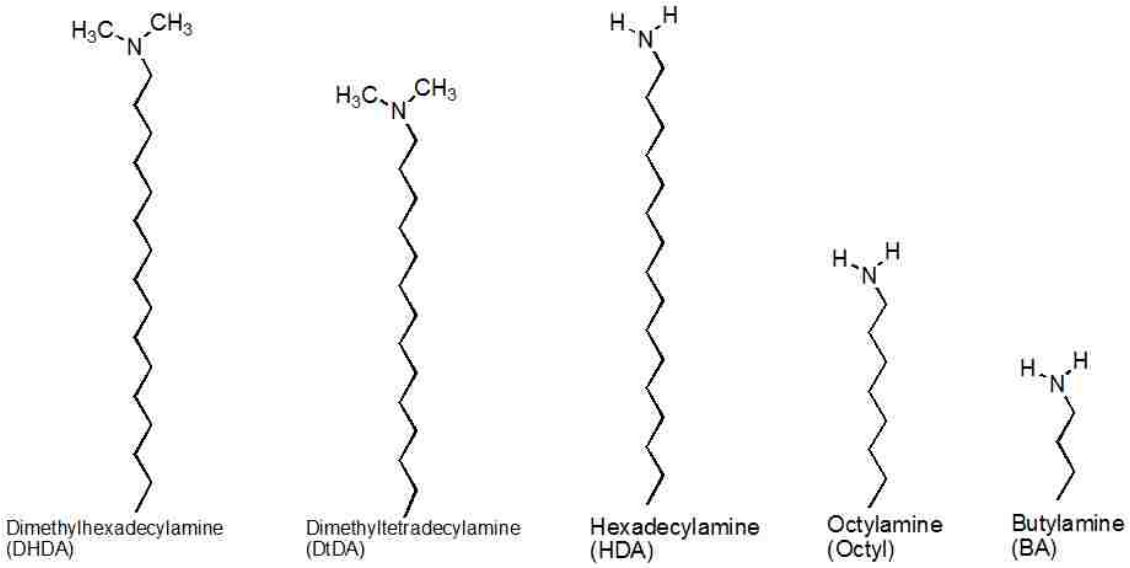

Figure 4.1 chemical structures of amines used in this study

4.2 Experimental

4.2.1 Materials

Zirconium (IV) chloride (98 %), phosphoric acid (85 % w/v), dimethyltetradecylamine (DtDA), (95 %), dimethylhexadecylamine (DHDA), (95 %), octylamine (Octyl), butylamine (BA), hexadecylamine (HAD) and ethanol (95 % w/v) were purchased from Sigma Aldrich. All chemicals were used as supplied without further purification.

α-ZrP was synthesized according to literature method [61] as described in Chapter 2. Intercalation of DHDA into layered zirconium phosphate was achieved by mixing 5 grams of the layered material with 10 millimoles of DHDA in ethanol. The mixture was stirred at room temperature for 2 days. The solution was filtered and washed with ethanol to remove unreacted DHDA. Intercalation of DtDA, HDA, Octyl and BA was achieved using a procedure similar to the intercalation of DHDA. The products will hereafter be referred to as ZrP-DtDA and ZrP-DHDA, ZrP-HAD, ZrP-Octyl and ZrP-BA, for the dimethyltetradecylamine and dimethylhexadecylamine, hexadecylamine, octylamine and butylamine intercalation products, respectively.

4.2.2 Analytical Techniques

Powder X-ray diffraction patterns of ZrP-DHDA, ZrP-DtDA, ZrP-HAD, ZrP-Octyl, ZrP-BA were obtained using a Rigaku Miniflex II diffractometer. The specifications of the diffractometer were described in Chapter 2. Infrared absorption spectra were obtained using a Perkin Elmer Spectrum 100 Fourier transform infrared

(FTIR) spectrometer equipped with a single reflectance ZnSe attenuated total reflectance (ATR) accessory from Pike Technologies. Solids were pressed on the ATR accessory. Infrared spectra were recorded at a resolution of 2 cm^{-1}, averaged over 8 scans, in the range 4000 cm^{-1} to 675 cm^{-1}. The instrument and experimental details of Transmission Electron Microscopy, solid state NMR and Thermogravimetric analysis were described in Chapter 2. The chain length of the alkylamines were calculated using B3LYP/6-31G* level in Gaussian 03.[122]

4.3 Results and Discussion

4.3.1 X-ray diffraction analysis of Intercalation of tertiary amines in α-ZrP

Synthesis of α-ZrP and intercalation of alkylamines was confirmed using X-ray diffraction analysis and Fourier Transform Infrared Spectroscopy. The X-ray diffraction patterns of α-ZrP, ZrP-BA, ZrP-Octyl, ZrP-HAD, ZrP-DtDA and ZrP-DHDA are shown in Fig. 4.2.

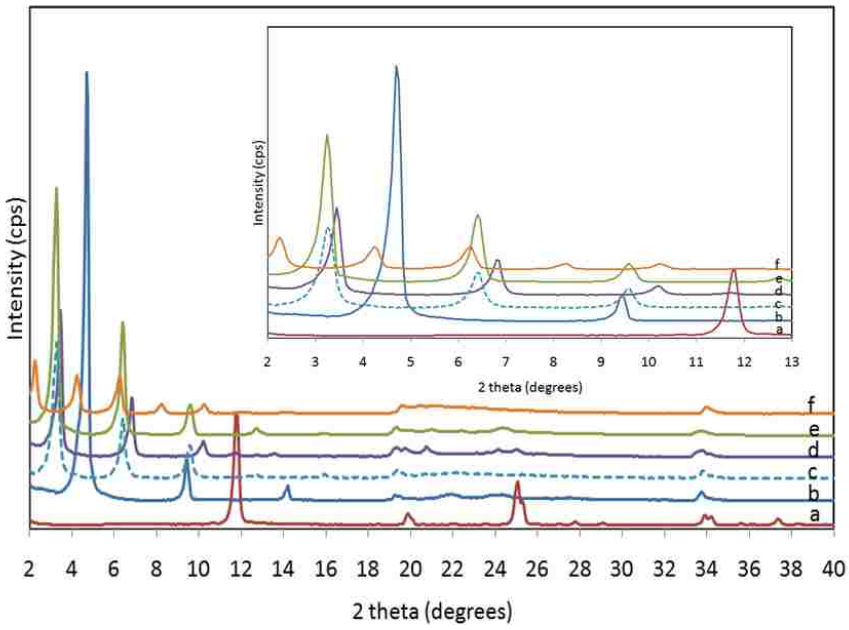

Figure 4.2 Powder X-ray diffraction patterns of ZrP (a), ZrP-BA (b) ZrP-Octyl (c) ZrP-DtDA (d) ZrP-DHDA (e) ZrP-HDA (f). The positions of the (002) peak for each pattern are clearly shown in the insert.

The first peak, with Miller indices, *002* at 2 θ value of 11.7 ^{0} suggest an interlayer space of 7.6 Å. This value is consistent with a value of 7.65 Å reported for α-ZrP.[64] Trace b in Fig. 4.2 shows that upon intercalation of butylamine (BA) the *002* peak in α-ZrP shifts to a 2 θ value of 4.7 ^{0} .This corresponds to an interlayer spacing of 18.6Å. Trace c in Fig.4.7 shows that upon intercalation of octylamine the *002* peak in α-ZrP shifts to a 2 θ value of 3.2 ^{0}, corresponding to an interlayer spacing of 27.6 Å. Upon intercalation of DtDA (Trace d) the *002* peak shifts to a 2 theta value of 3.42 ^{0} corresponding to an interlayer space of 25.6 Å. The interlayer spaces resulting from intercalation of HDA and DHDA are 43.1 Å and 28.03 Å, respectively. The *00l* (*l*=2 to 6) basal reflections found in the lower angle region for ZrP-BA, ZrP-Octyl, ZrP-DtDA and ZrP-DHDA are narrow and equally spaced indicating high range ordering in the *c*-axis. It is also noted that the

reflection at $2\theta = 34^{0}$ with Miller indices (*020*) in the α-ZrP remains largely unaltered after intercalation of alkylamines suggesting that the intercalation processes occurring in the interlayer region of the α-ZrP do not significantly alter the Zr-O-P framework. The increase in interlayer space due to alkylamine intercalation is obtained by subtracting the zirconium phosphate layer thickness of 6.3 Å [68] from the d-spacing obtained from X-ray diffraction. For example the observed d-spacing for the intercalation of butylamine in ZrP is 18.6 Å, if 6.3 Å is subtracted from this value; the interlayer space obtained is 11.4 Å. The length of butylamine calculated from a B3LYP/6-31 G* optimized structure using Gaussian 03 [122] is 6.2 Å. The chain length reported here is the distance from the center of the hydrogen atom attached to the nitrogen atom to the center of the hydrogen atom attached to the carbon atom furthest from the nitrogen group. This suggests that the interlayer increase is consistent with a bilayer arrangement of butylamine molecules tilted at some angle in the interlayer space of ZrP.

The optimized geometries of the DHDA and DtDA molecules were used to calculate the chain lengths. The chain lengths are reported as the distance from the center of the hydrogen atom of the methyl group attached to the nitrogen atom to the center of the hydrogen atom attached to the carbon atom furthest away from the nitrogen atom. The chain lengths are 21.2 Å and 22.8 Å for DtDA and DHDA, respectively. The interlayer increases for both DtDA and DHDA are consistent with the molecules of the respective tertiary amines forming an interdigitated i.e. overlapping, arrangement in the interlayer space rather than the more commonly observed bilayer structure. The calculated lengths of the alkylamines used in this study are shown in Table 4.1 along with the observed interlayer increases. The arrangement of alkylamine molecules in Table 4.1

is proposed after comparing the calculated sizes and the interlayer increase obtained from X-ray diffraction patterns.

Table 4.1 Calculated alkylamine sizes and proposed interlayer arrangement of alkylamines in ZrP interlayer spaces

Alkylamine	Calculated Length (Å)	XRD Observed interlayer increases(Å)	Arrangement of molecules in the ZrP interlayer space
Butylamine	6.2	11.3	bilayer
Octylamine	11.6	20.9	bilayer
Hexadecylamine	20.7	38.9	bilayer
Dimethyltetradecylamine	21.2	19.5	interdigitated
Dimethylhexadecylamine	22.8	20.2	interdigitated

It is noted from Fig.4.1 that the only difference in the structure of hexadecylamine (HDA) and dimethylhexadecylamine (DHDA) is that the hydrogen atoms attached to nitrogen are replaced by methyl group. However, as shown in Table 4.1, HDA molecules form a bilayer arrangement in the ZrP interlayer spaces while DHDA molecules form an interdigitated arrangement. We attribute this to differences in the cross sectional area of DHDA and HAD. The cross sectional area of *trans-trans* monoalkyls obtained from unit cell parameters of solid paraffin is 18.4 $Å^2$,as reported in section 4.1.1.

The cross sectional area for the tertiary amines, DtDA and DHDA were estimated using a method reported by Valvani and co-workers. [123] In this method, a methyl group is considered as a single sphere rather than individual atoms. Fig.4.3 shows a schematic

diagram of the planar view as treated in the method for estimating the cross-sectional area of a methyl group. Solid curves show a carbon atom in the center (van der Waals radius, 1.6 Å) and three tetrahedral hydrogen atoms (van der Waals, 1.2 Å) located at 1.09 Å from the center of the carbon atom. The dotted circle shows the methyl group as single sphere with a radius of 2.0 Å. This allows us to estimate the surface area of the methyl group to be 33.5 $Å^2$. This suggests that the total cross sectional area of DHDA and DtDA using the sum of the cross sectional areas of methyl groups and nitrogen atom (van der Waals radius 1.5 Å) is DtDA is 73.5 $Å^2$.

Figure 4.3 Planar view of a methyl group. The solid lines show a carbon atom in the center with van der Waals radius of 1.6 Å and, 3 hydrogen atoms with van der Waals radius 1.2 Å. The dotted lines show the whole methyl group treated as a sphere of radius 2 Å.

The surface area of the active P-OH group is reported to be 24 $Å^2$. The surface area for DHDA and DtDA may suggest that each tertiary amine interacts with three P-OH groups. This arrangement of tertiary amine would result in what has been referred to as

the “covering effect” [116] where some of the P-OH group in the intercalated product remain unreacted. The steric effect of the methyl groups also hinders consecutive tertiary amines in the interlayer space to have their amine groups side by side resulting in an interdigitated arrangement as shown in Fig.4.4.

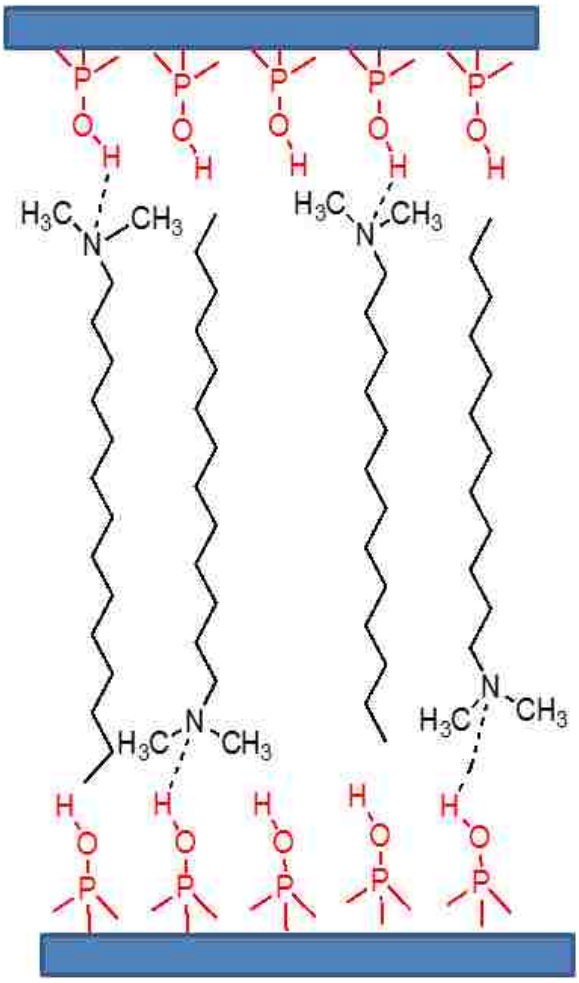

Figure 4.4 Schematic representation of ZrP-DHDA showing one alkylamine interacting with 3 phosphate groups. OH groups of phosphate are not shown for clarity. The length of the alkyl chain does not represent the actual number of carbon atoms

The arrangement of tertiary amines in ZrP interlayer spaces shown in Fig.4.4 is substantially different from the arrangement of primary amines such as butylamine, octylamine or hexadecylamine. It has been reported that the cross-sectional area of primary amines is 18.6 $Å^2$.[64,68] This arrangement results in a one to one reaction of the primary alkylamines with the P-OH groups. The proposed arrangement of primary alkylamines in the ZrP interlayer spaces is shown in Fig.4.5.

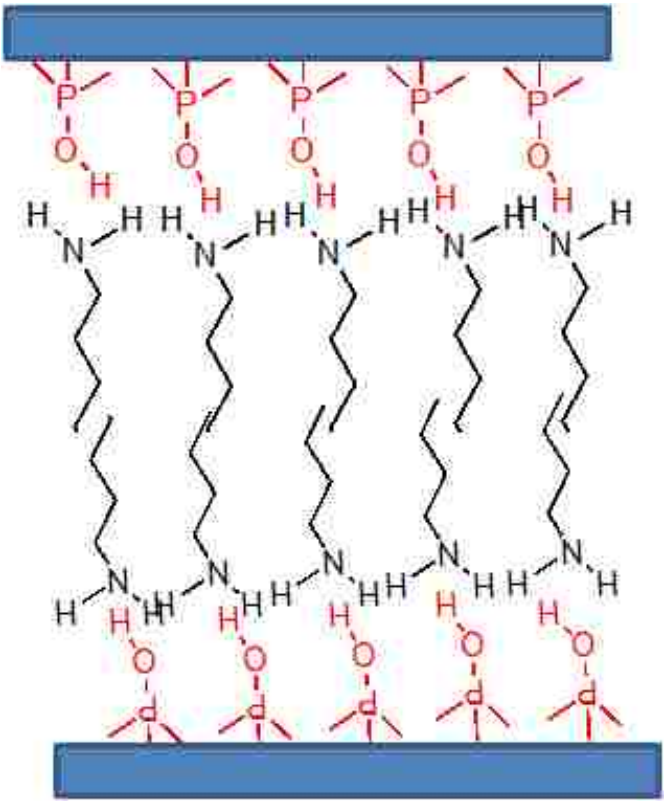

Figure 4.5 Schematic representation of ZrP-BA showing one alkylamine interacting with 1 phosphate group. Interlayer water molecules are not shown for clarity.

A comparison of the interlayer increase due to octylamine and dimethylhexadecylamine intercalation shown in Table 4.1 would also support the bilayer arrangement of the octylamine molecules in the ZrP interlayer space shown in Fig.4.5. It is noted that the

alkylamine chain length in DHDA is twice as long as the octylamine length but we observe interlayer increases of about the same size confirming that octylamine molecules form a bilayer arrangement while DHDA form an interdigitated arrangement.

It has been reported that the loading of primary alkylamines affects the phase compositions of the intercalated compounds. At low loadings the alkylamines are believed to lie parallel to the zirconium phosphate layers, while an increase in the concentration of reactant amines results in alkylamines intercalated in bilayer arrangements.[60, 68] The interlayer distance of ZrP is 7.6 Å, upon intercalation of propylamine at a loading rate of 1 millimole propylamine per gram of ZrP, a mixture of phases with interlayer distances of 9.9 Å and 10.4 Å were formed.[66] The 10.4 Å phase was reported to increase in intensity relative to the former phase upon increasing the amine loading, until it was the only phase at an amine loading of 2 millimoles per gram of ZrP. When the loading was increased further, a mixture of phases was observed at a loading of 5 millimoles per gram with a pure 16.4 Å phase being obtained at a loading rate of 6 millimoles per gram of ZrP. Finally a 17.6 Å phase was obtained for a loading of 8 millimoles per gram of ZrP. This phase was reported to have 2 mol amine per mol of ZrP.[66] This behavior in which a progressive increase of added amines resulted in a corresponding change of product phases, was also observed for the intercalation of butylamine and octylamine.[60,68]

The intercalation of DtDA and DHDA is substantially different from that of primary alkylamines. Only one phase is observed for the intercalation of DtDA and DHDA. Fig.4.6 shows the powder X-ray diffractions for the intercalation of DHDA using different loadings. It is noted that there is only one phase which increases in intensity as

the loading increases. The difference in the intercalation behavior of DtDA or DHDA in ZrP from the intercalation of primary amines is also observed using FTIR spectroscopy discussed in section 4.3.2.

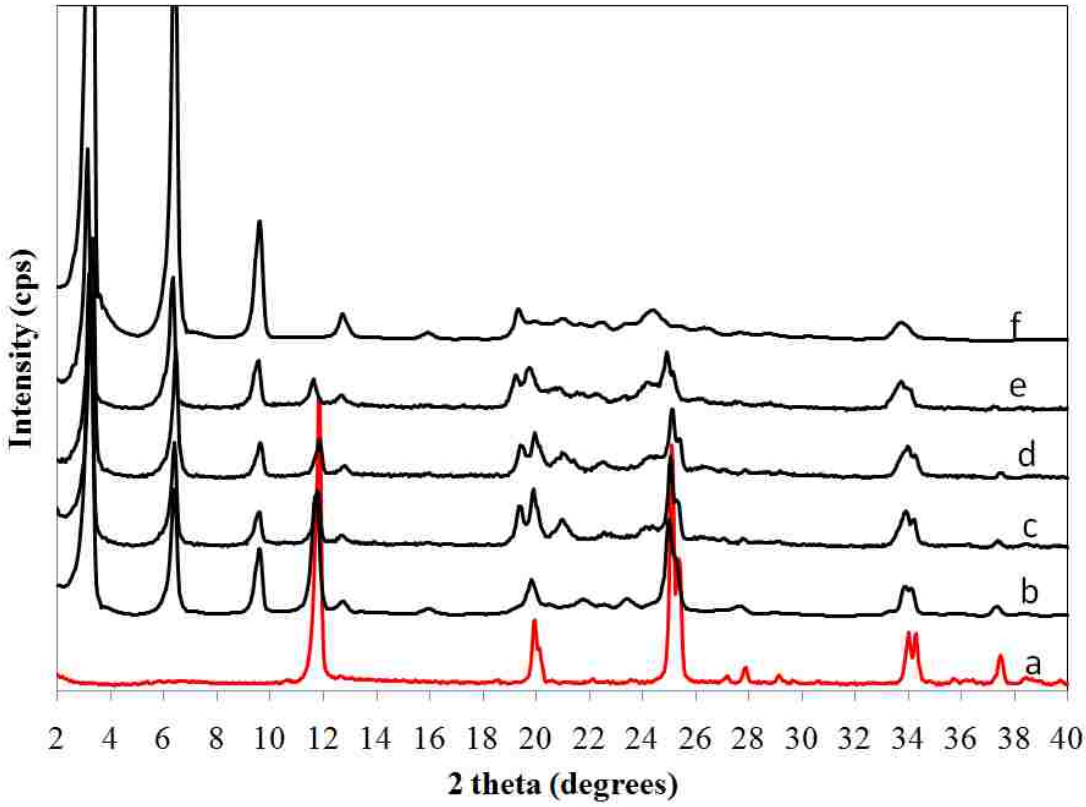

Figure 4.6 X-ray diffraction patterns for the intercalation of DHDA in ZrP (a) at a loading rate of 3 mmoles per gram (b) 5 mmoles per gram (c) 7 mmoles per gram (d) 9 mmoles per gram (e) and 12 millimoles per gram (f)

4.3.2 Spectroscopic characterization of alkylamine intercalation

4.3.2.1 Attenuated total reflectance Fourier transform infrared spectroscopy

The interaction between alkylamines and the host layers was studied using IR spectroscopy. As an example, the infrared spectra of the ZrP-DHDA together with the

spectra of α-ZrP and pure dimethylhexadecylamine are shown in Fig.4.7. The intercalation of DHDA in ZrP is confirmed by the peaks at 2989 cm^{-1} attributed to ν_s (CH) of DHDA

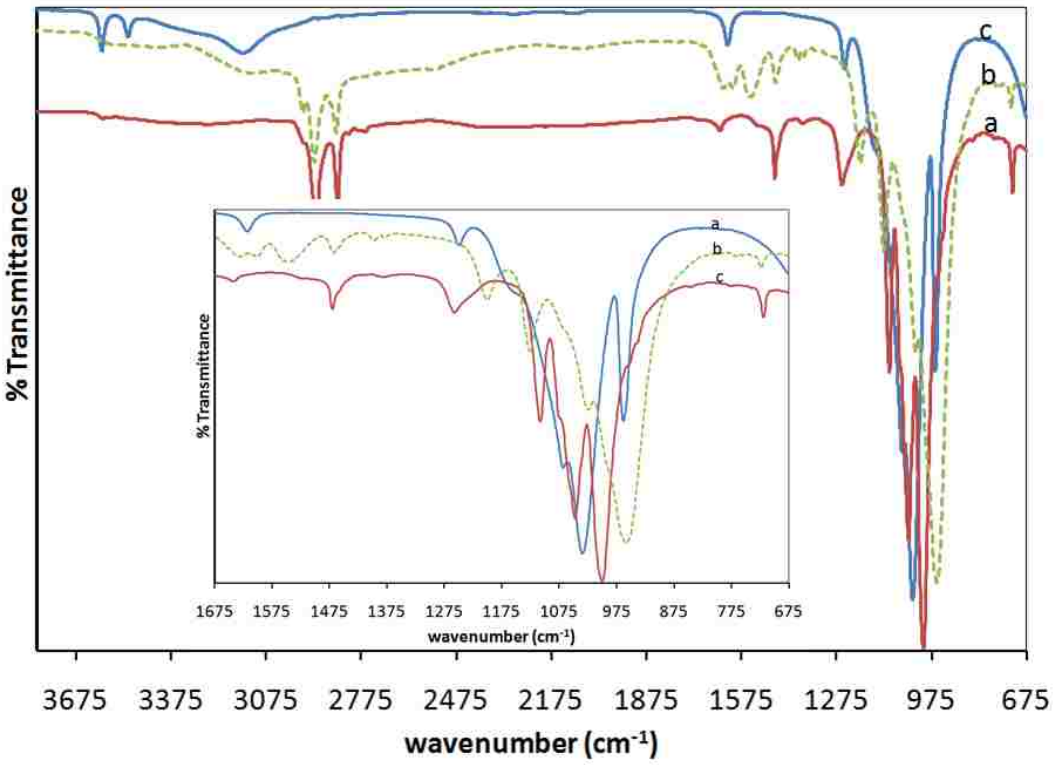

Figure 4.7 ATR FTIR spectra of ZrP (a) DHDA (b) ZrP-DHDA (c). Insert shows the spectra in the wavenumber range 1675 cm^{-1} to 675 cm^{-1} showing the shift of the PO_4 stretching band upon intercalation of DHDA in ZrP

Two sharp bands observed in the ZrP spectrum at 3593 and 3510 cm^{-1}, attributed to the ν_{as} (OH) stretching modes of lattice water,[121] completely disappear upon intercalation of DHDA. The disappearance of the OH stretching modes may suggest a difference in hydrogen bonding character upon intercalation of alkylamines or the substitution of water by alkylamines. The band at 3150 cm^{-1} is assigned to ν_s (OH). This

band also broadens after intercalation of dimethylhexadecylamine. The insert in Fig. 4.7 shows the spectra in the wavenumber range 1675 cm^{-1} to 675 cm^{-1}. The σ_{as} (OH) band at 1612 cm^{-1} in ZrP shifts to 1636 cm^{-1} upon intercalation of DHDA. The in-plane bending mode ν_{in}(POH) at 1252 cm^{-1} in ZrP shows up as a broad band around 1215 cm^{-1} in the presence of DHDA. The FTIR spectrum of DtDA is similar to the FTIR spectrum of DHDA presented in Fig.4.7. As can be observed from Fig.4.8 below for BA intercalation the ν_{in} POH) band at 1252 cm^{-1} disappears when the primary amine is intercalated. This is an indication of complete deprotonation of the phosphate groups when alkylamines are intercalated whereas due to the "covering effect" mentioned in section 4.1.1 some of the phosphate groups remain unreacted upon intercalation of DHDA

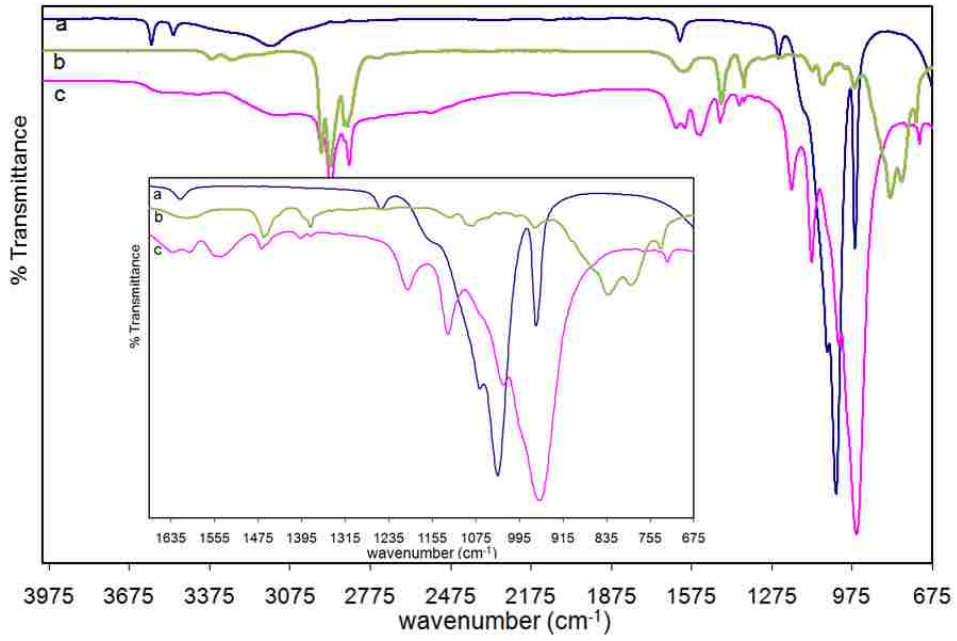

Figure 4.8 ATR-FTIR spectrum of ZrP (a) Butylamine (b) ZrP-BA (c). Insert shows the 1650 cm-1 to 675 cm-1 range which shows the shift in the PO_4 stretching band upon intercalation of butylamine in ZrP

The positions of the ν (PO_4) band in ZrP shifts from 1035 cm^{-1} to 998 cm^{-1} upon intercalation of DHDA (Fig.4.7). The same band shifts to 958 cm^{-1} upon intercalation of butylamine (Fig.4.8). This is another indication that the intercalation of butylamine results in complete reaction of the phosphate groups in ZrP while some phosphate groups may still be unreacted even after complete intercalation of DHDA.

4.3.2.2 Solid state ^{31} Phosphorus nuclear magnetic resonance spectroscopy

It has been shown that the intercalation of amines into the gallery space of ZrP results in downfield shift of the ^{31}P NMR peak.[119] A downfield shift of up 10 ppm have been observed for deprotonated phosphate groups, while shifts of about 2-4 ppm were attributed to hydrogen bonded phosphate groups.[66] The ^{31}P NMR spectra of α-ZrP and ZrP-DHDA are shown in Fig.4.9.

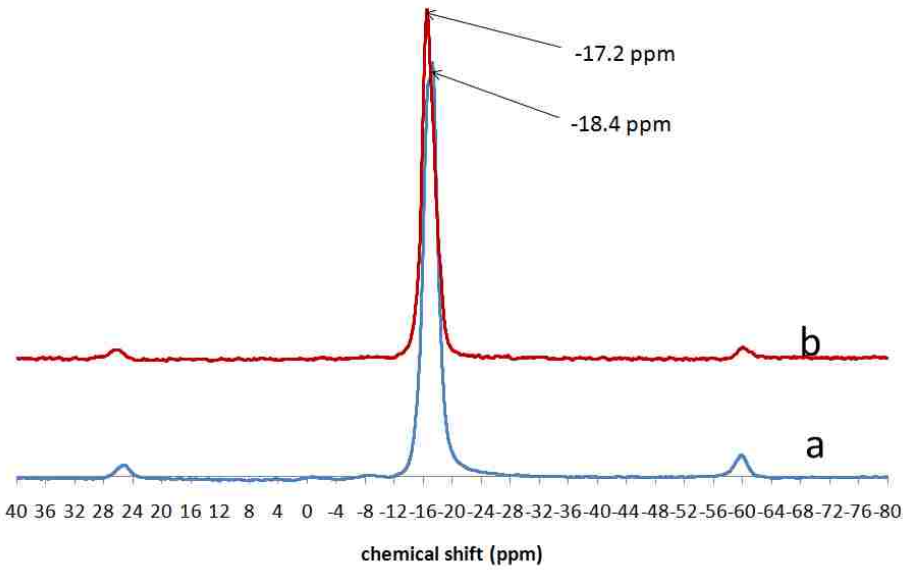

Figure 4.9 ^{31}P solid state NMR spectrum of ZrP (a) and ZrP-DHDA (b)

The initial ZrP phase shows a single resonance peak at -18.4 ppm, with spinning side bands on either side of the isotropic resonance. The low intensities of the spinning side bands suggest that the chemical shift anisotropy is small.[124] A small downfield shift of 1.2 ppm is observed for ZrP-DHDA (Fig.4.9, Trace b) suggesting that the phosphate groups are most likely hydrogen bonded to the amine molecules. The resonance peak in Trace b shows significant broadening. A likely cause of this broadening is chemical shift dispersion[125] as a result of disordered placement of the phosphate groups between the layers upon intercalation of DHDA.

However, the ^{31} P NMR spectrum for ZrP-BA in Fig.4.10 shows two ^{31}P resonances of unequal intensities which suggest two chemically distinct phosphate groups.

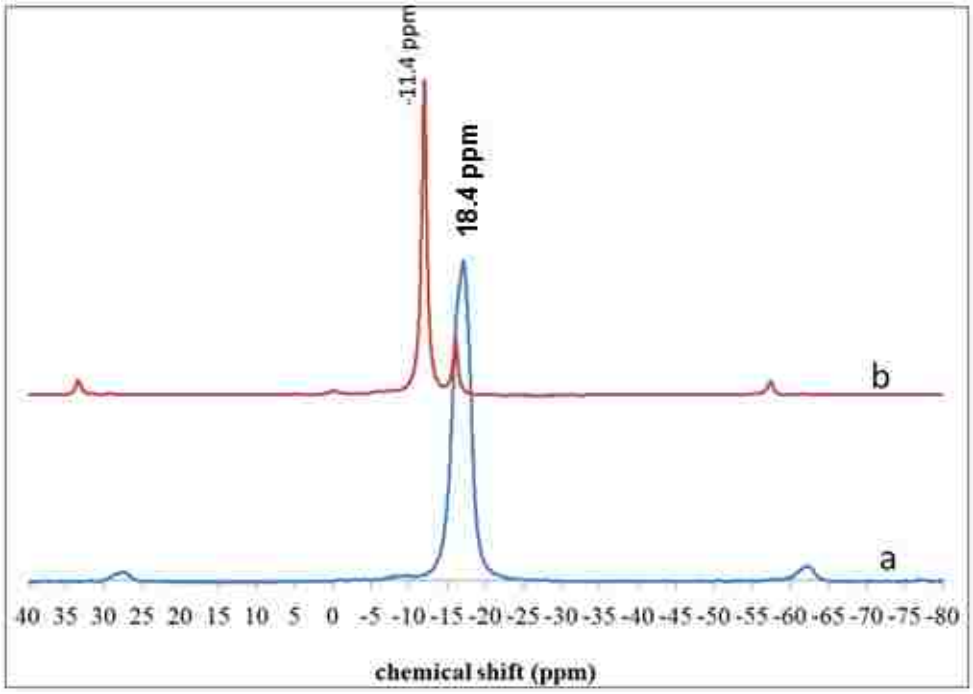

Figure 4.10 ^{31}P solid state NMR spectrum of ZrP (a) and ZrP-BA (b)

The smaller peak at 16.2 ppm may represent phosphate groups that are hydrogen bonded to butylamine molecules while the larger peak at -11.4 ppm may represent deprotonated phosphate groups. Integration of the two peaks shows that the ratio of the deprotonated phosphate groups to the hydrogen bonded phosphate groups is approximately 4:1. This suggests that about 80 % of the phosphate groups are deprotonated.

Results obtained from solid state NMR are consistent with ATR-FTIR results where it was observed that the intercalation of DHDA, a tertiary amine, in ZrP results incomplete deprotonation of the phosphate groups despite the X-ray diffraction patterns showing no ZrP phase. Whereas, the chemical shifts of ZrP-BA NMR and the ATR-FTIR spectrum are consistent with deprotonation of the phosphate groups. It is therefore proposed that the bonding in ZrP-BA is predominantly ionic while the bonding in tertiary amines is predominantly hydrogen bonding as shown in the bonding schemes below, where R, represents the alkyl chains.

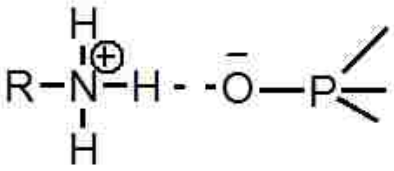

Ionic bonding

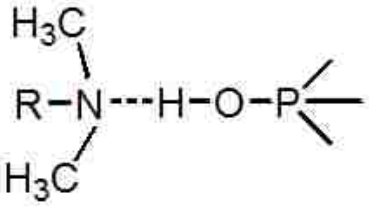

Hydrogen bonding

4.3.3 Transmission Electron Microscopy

The microstructure of layered zirconium phosphate and layered ZrP-DHDA was analyzed using TEM. Fig.4.11 shows TEM images of zirconium phosphate and ZrP. The image at

low resolution (200 nm) shows particles with a mixture of shapes including hexagonal shapes and some irregular polygons. The hexagonal shapes are clearly shown in the higher resolution (50 nm) image. The diameter of one particle in Fig.4.11 (picture b) obtained by measuring using the image scale bar is 42 nm.

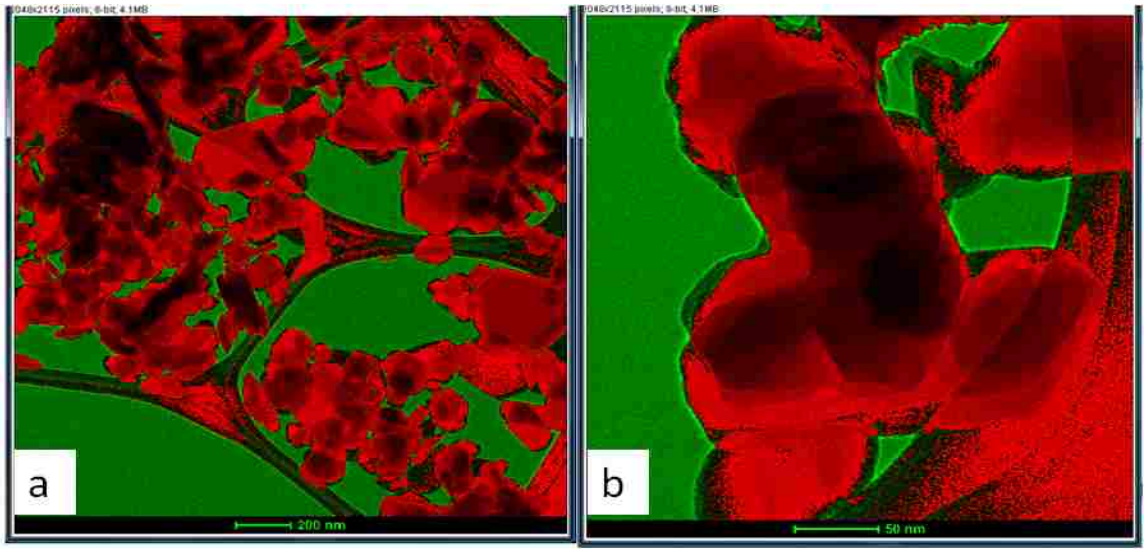

Figure 4.11 TEM images of ZrP at a resolution of 200 nm (a) and 50 nm (b)

The TEM images of ZrP-DHDA are shown in Fig.4.12. Image (a)shows random shapes of the ZrP-DHDA.

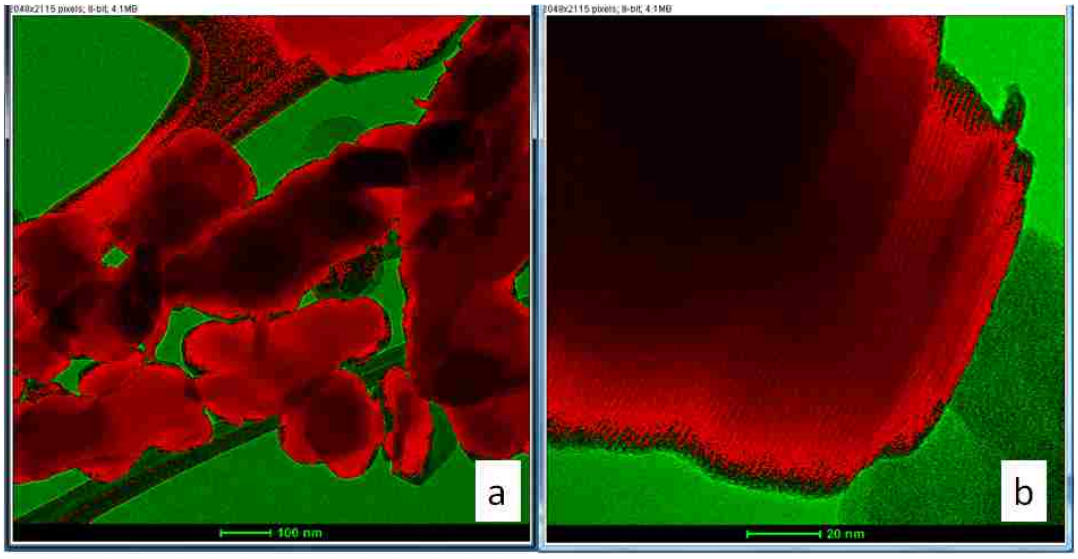

Figure 4.12 TEM images of ZrP-DHDA at a resolution of 100 nm (a) 20 nm (b)

The lattice fringes in ZrP-DHDA are very obvious in image (b) at 20 nm resolution. The space between the lattice fringes estimated using the scale bar is 2 nm. This value is in reasonable agreement with the d-spacing of 2.7 nm observed from X-ray diffraction analysis. Image b also suggest that there is uniform growth in one direction suggesting that with proper control of synthesis method and conditions layered ZrP-DHDA of high aspect ratio can be synthesized.

4.3.4 Thermogravimetric Analysis of zirconium phosphate and intercalation products

The composition of the intercalated products (ZrP-DHDA and ZrP-DtDA) was obtained from thermogravimetric analysis. TGA curves for ZrP and the intercalation products are shown in Fig.4.13

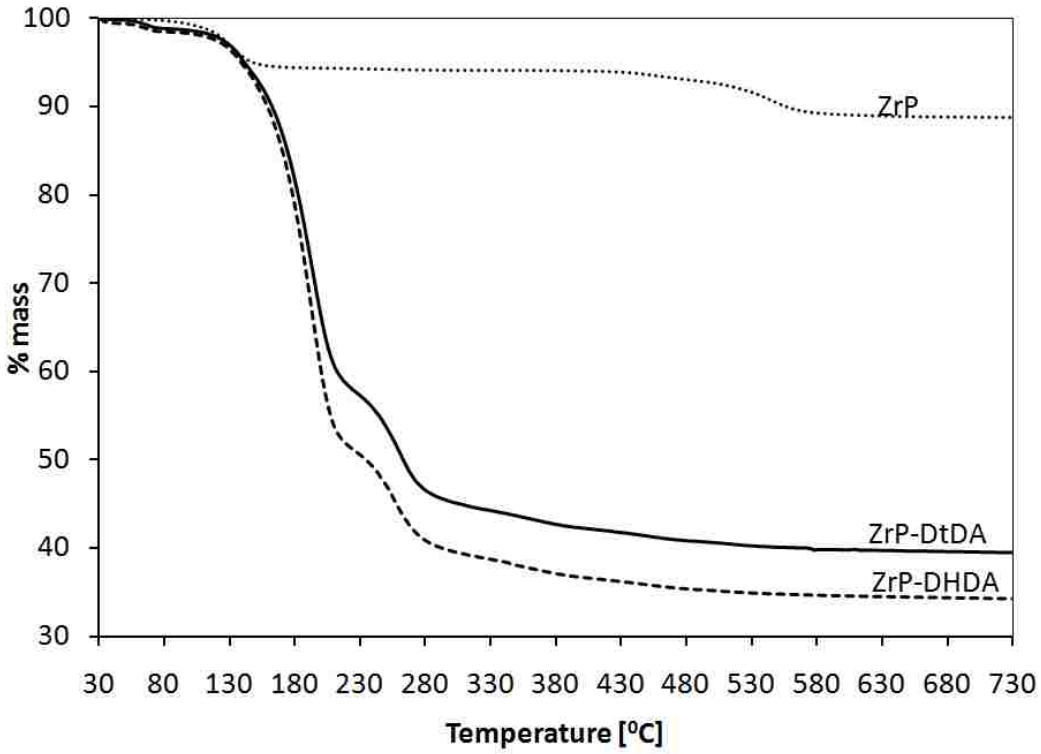

Figure 4.13 Thermogravimetric analysis curves for ZrP (upper trace), ZrP-DtDA (middle trace) and ZrP-DHDA (dotted Trace) . TGA was run under air between 50 ^{o}C and 800 ^{o} C at a ramp rate of 10 0 C min^{-1}

The TGA curve for zirconium phosphate shows three distinct processes. The first weight loss between 109 and 154 ^{0}C is attributed to water loss. The loss between 426 ^{0}C and 556 ^{0}C is attributed to dehydroxylation of the phosphate with subsequent transformation to zirconium pyrophosphate (ZrP_2O_7).[62] The total weight loss was 11.26 %. The product of the degradation of ZrP was confirmed by X-ray diffraction analysis. The X-ray diffraction pattern of a sample of ZrP heated in a furnace at 700 ^{0}C for 12 hours under air showed that the Zr-O-P frame is still intact at 700 ^{0}C. Fig.4.14 shows the X-ray diffraction pattern of ZrP_2O_7 .

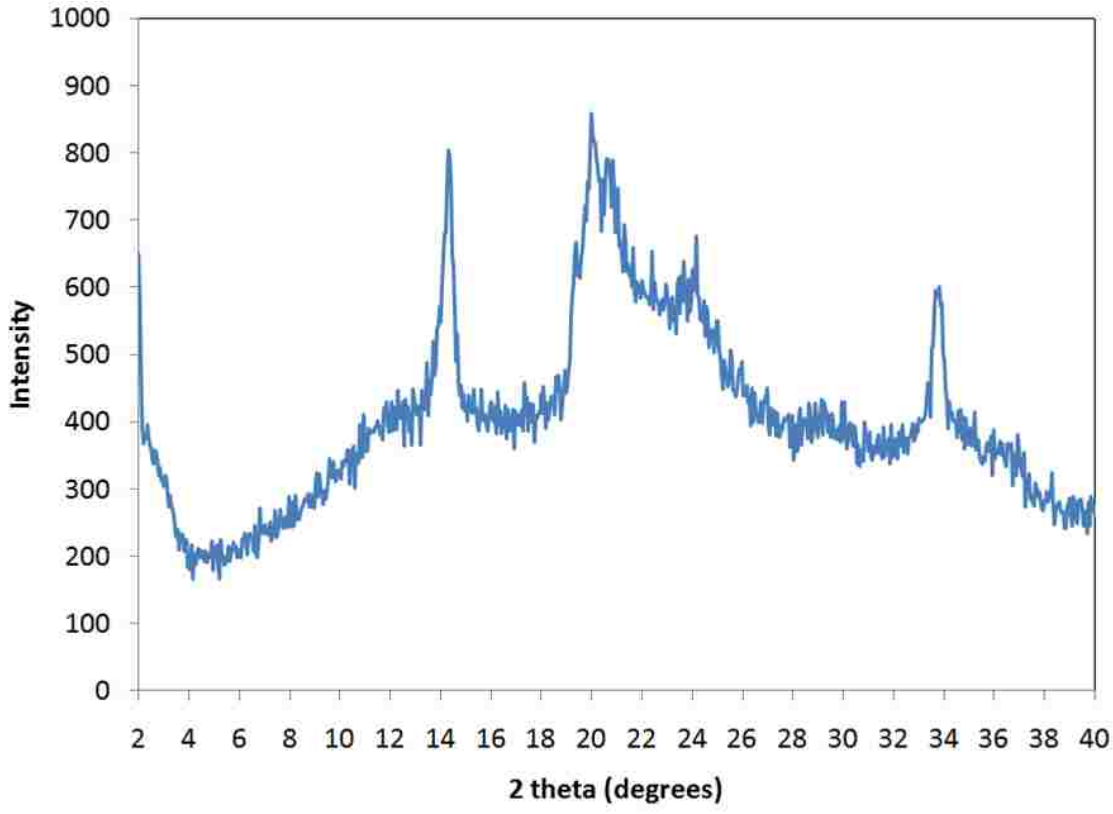

Figure 4.14 X-ray diffraction pattern of the final product of thermal degradation of ZrP. The sample was heated to 700 ^{0}C and cooled before XRD analysis.

The *002* peak at 2 theta 14.3^0 in Fig.4.14 is shifted to higher 2 theta angle compared to the *002* peak in ZrP (2 theta value 11.7 ^{0}). This increase in 2 theta value is consistent with decrease in the interlayer space that is due to the loss of interlayer water molecules upon heating the ZrP sample. The *020* peak at 2 theta value of 33.6 in ZrP appears around the same position after heating to 700 ^{0}C. This suggest that the zirconium phosphate layer is stable up to 700 ^{0}C. The TGA and DTG curves for ZrP showing the temperatures at which the three distinct steps of ZrP degradation are presented in Fig.4.15 as well as the FTIR absorption spectra of the gases evolved at 130 ^{0}C and 450 ^{0}C.

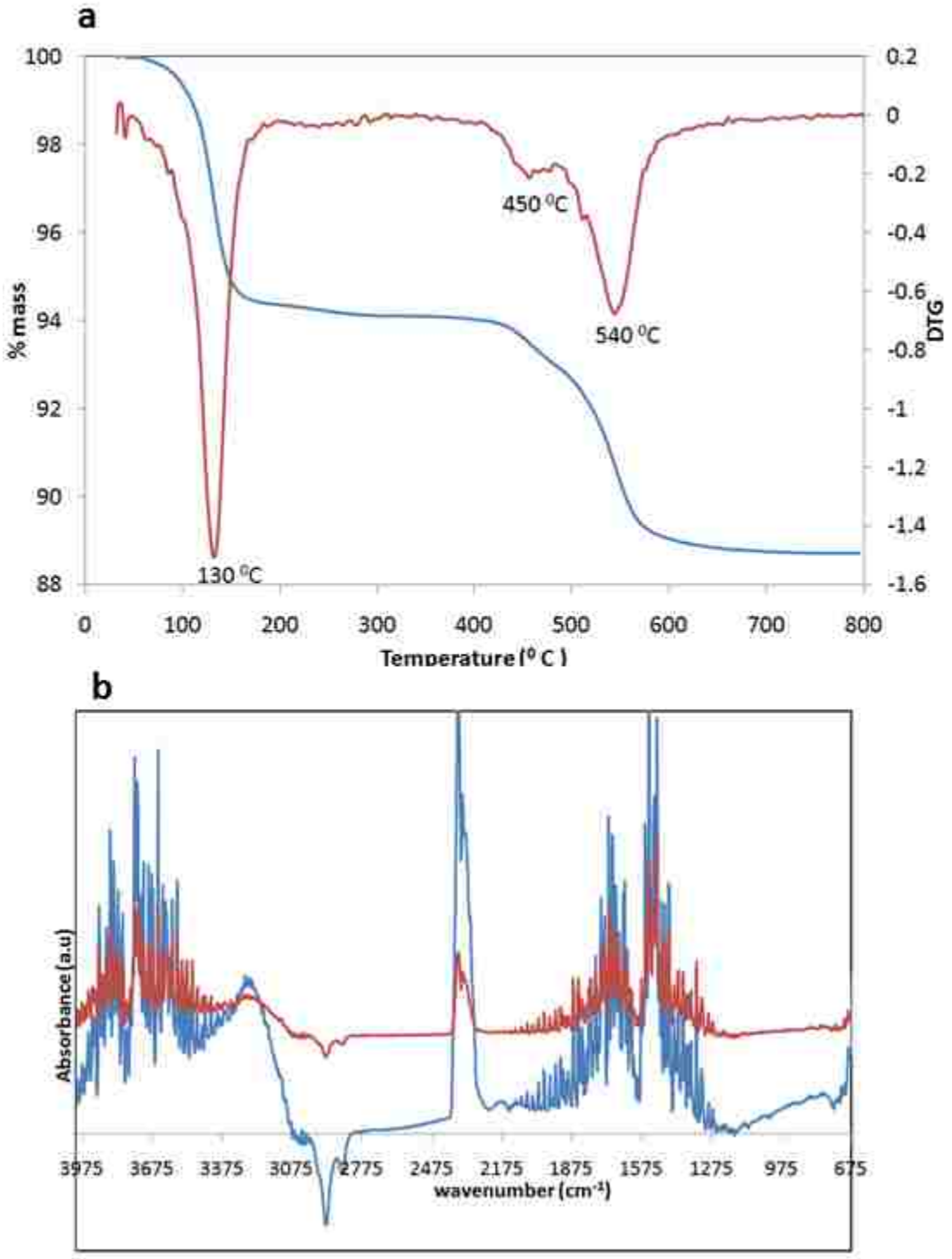

Figure 4.15 TGA-DTG (a) for the degradation of ZrP. The DTG curve shows the temperature at which loss of water occurs. (b) FTIR spectra of the gas evolved at 130 ^{0}C (blue trace) and 450^0 C (red trace)

The degradation of alkylamine intercalated α-ZrP is divided into three temperature regions as well: dehydration (60 ^{0}C -130 ^{0}C), desorption and decomposition of the amines (160 ^{0}C -400 ^{0}C) and dehydroxylation of the phosphate groups (400 ^{0}C – 800 ^{0}C).As can be observed in Fig 4.13 the loss of water for the alkylamine intercalates occurs at lower temperatures than for α-ZrP. This is because upon intercalation of alkylamines, the water molecules in the interlayer space of ZrP are substituted by alkylamines. Fig.4.16 a shows the TGA and DTG curves for ZrP-DHDA. The FTIR spectra of the gases evolved during the decomposition process is shown in Fig.4.16b.

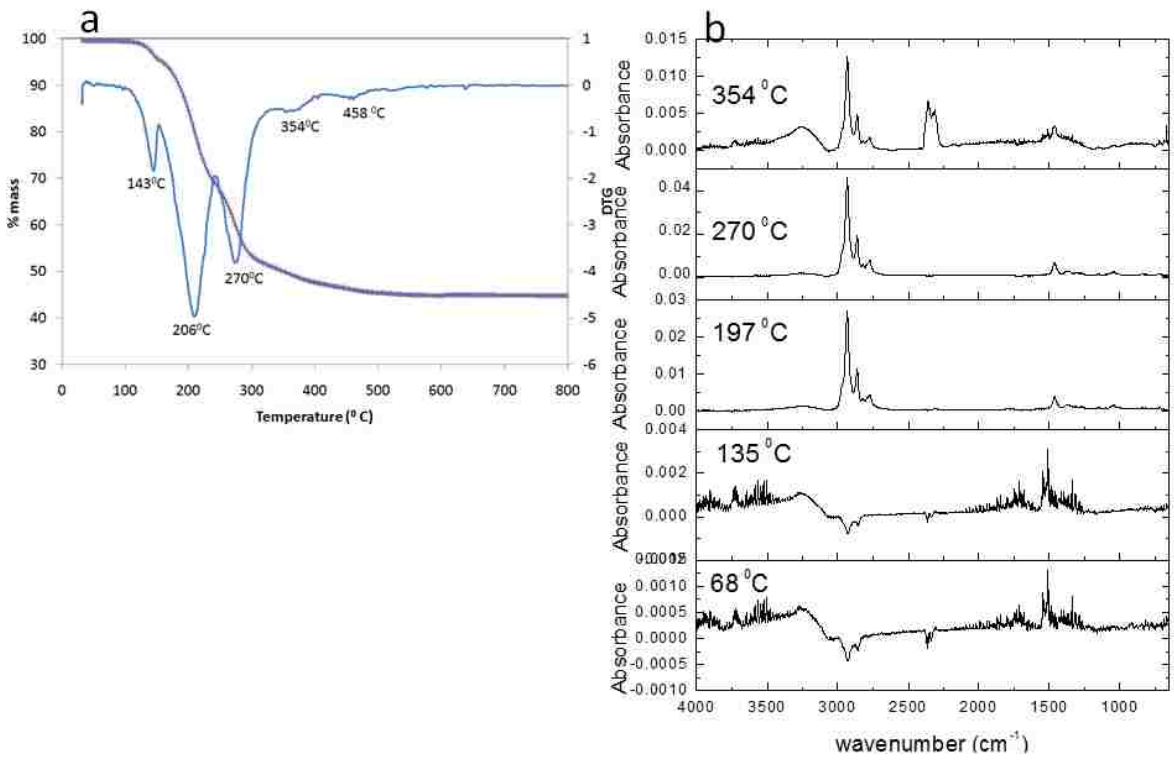

Figure 4.16 TGA-DTG curves for ZrP-DHDA (a) and FTIR (b) of the gases evolved during heating of ZrP-DHDA from 50 ^{0} C to 800 ^{0} C.

The FTIR absorption spectra (Fig.4.16 b) show the different products that are evolved during the degradation process. The first two spectra at 68 ^{0}C and 135 ^{0}C indicate the loss of water, the organic alkylamine is observed at 197 ^{0}C as shown by sharp peaks around 2900 cm^{-1} which are due the C-H stretching modes. The desorption and degradation of alkylamines continues beyond 300 ^{0}C as observed from the FTIR spectra at 270 ^{0}Cand 354 ^{0}C. It is noted from the spectrum at 354 ^{0}C that peaks due to OH asymmetric stretching modes around 3500 cm^{-1} and the bending OH mode around 1620 cm^{-1} start to be more prominent again at this temperature. This is evidence of the dehydroxylation of the phosphate groups.

Assuming the final product of the degradation of the ZrP-DHDA is ZrP_2O_7, the chemical formula of ZrP-DHDA was estimated using the TGA-FTIR data shown in Fig.4.16. The final product obtained after heating the sample was 45.2 % of the total sample. The total percentage of water was obtained by subtracting the amount of water lost below 143 ^{0}C. This amount was 4.6 % of the total sample. The total organic content of the ZrP-DHDA was therefore estimated to be 50.2 % of the total sample. The elemental analysis data for zirconium phosphate and its intercalation compounds are presented in Table 4.2.

Table 4.2 Microanalytical data for zirconium phosphate and the intercalation products

Compound	% Zr	% P	% C	% N	% H
ZrP	29.4	20.8	0.13	0.02	1.43
ZrP-BA	20.1	14.1	21.55	6.48	5.77
ZrP-DHDA	15.7	11.0	36.61	2.46	7.49
ZrP-DtDA	17.4	12.2	31.93	2.09	6.81

The analytical data shown in Table 4.2 is in reasonable agreement with the proposed structures of dimethylhexadecylamine (DHDA) and butylamine (BA) intercalated ZrP presented in Fig.4.4 and Fig.4.5, respectively. The structures proposed suggest that the ratio of phosphorus to nitrogen is much higher in ZrP-BA than in ZrP-DHDA because of steric hindrance in DHDA molecules due to the presence of bulky methyl groups. The phosphorus to nitrogen ratio in ZrP-BA is 2.17 while in ZrP-DHDA it is 4.45. Based on the compositions shown in Table 4.2 as well as data from TGA analysis, the chemical formulae for the intercalation compounds are $Zr(HPO4)_{2.3}$ 2.8 $C_4H_9NH_2$ 0.5 H_2O for ZrP-BA, $Zr(HPO_4)_{2.3}$ 0.8 $(CH_3)_3(CH_2)_{15})N$ 1.2 H_2O for ZrP-DHDA and $Zr(HPO_4)_{2.8}$ 1.2 $(CH_3)_3(CH_2)_{13})N$ 0.9 H_2O for ZrP-DtDA.

4.4 Conclusions

Zirconium phosphate was organically modified using dimethylhexadecylamine and dimethyltetradecylamine. These tertiary amines form an interdigitated arrangement in the interlayer space. ATR-FTIR and NMR data indicate that even though the ZrP phase is completely absent from X-ray diffraction, there is substantial amount of the phosphate group that remain unreacted. The increase in interlayer space is consistent with the chain length of the respective tertiary alkylamines intercalated.

5 ADSORPTION OF 4-CHLOROPHENOL BY DIMETHYL-HEXADECYLAMINE MODIFIED LAYERED A-ZIRCONIUM PHOSPHATE

5.1 Introduction

A wide variety of chlorinated compounds such as cleaning-solvents, plasticizers, lubricants, pesticides and refrigerants are used by society in many beneficial ways.[126] Chlorine is one of the most commonly used chemical for disinfecting waste water.[127] When used in excess, chlorine used for disinfection can produce harmful disinfection by-products. Chlorophenol is one of the disinfection by products that can reach potentially harmful levels in surface waters. These may be mono, di or trichlorophenols depending on the levels of the phenolic compounds as well as the disinfectant and the environmental conditions.[47] Even low levels of chlorophenol have been reported to be carcinogenic.[57] While some of chlorinated compounds are being replaced by less harmful chemicals, many continue to be used because of the lack of suitable replacements or as a result of economic considerations. Research efforts have therefore been undertaken to develop effective tools of monitoring and eliminating chlorinated and other problematic wastes from the environment.[128]

Adsorption is a widely used method for removing pollutants from water. Solid materials, such activated carbon[129-131] and inorganic clays [5,58,132] have been used by several researchers to remove pollutants from water. Activated carbon is well known as an effective sorbent of toxic materials from water. [46,47] Its sorbent characteristics are regenerable by thermal desorption and/or acid treatment, however a significant part of the sorbent is lost in each regeneration cycle.[43] This is one of the main reasons for activated carbon's low economical efficiency in its applications. Therefore, the interest in the

development of sorbents for specific surfaces such as nanocrystalline metal oxides, [128] layered nanodimensional materials[5,132,133] and organoclays[134,135] has significantly increased in recent years. Layered inorganic materials that are readily synthesized have been widely used for removal of pollutants in water.[132, 133,136] However, they are less effective at binding hydrophobic organic compounds (HOCs), such as pesticides or phenols, because of their strongly hydrophilic surface. Anionic surfactants, such as sodium dodecylsulfate (SDS), are the main organic modifying components of many clay minerals.[8, 57]

α-Zirconium bis(monohydrogen phosphate) monohydrate, α-$Zr(HPO_4)_2.H_2O$ (abbreviated α-ZrP) is a well-known inorganic ion exchanger with an interlayer distance of 7.6 Å. The structure of α-ZrP was presented in Chapter 1. The cation exchange capacity of α-ZrP is reported to be 6.64 mequiv/g of the exchanger.[3] The proton of the phosphate group can be exchanged with cations such as Na^+, K^+, Li^+, Cs^+ and Rb^+.[138] This has led to the development of zirconium phosphate as a sorbent for the removal of heavy metals.[139]

The interlayer spacing in α-ZrP can be expanded to accommodate cationic as well as neutral guests. Intercalation of alkylamines in α-ZrP was described in Chapter 4. Amines, which possess a Brønsted basic character have a high affinity for the Brønsted acidic P-OH groups and are easily adsorbed. To this end they have been widely used to organically modify ZrP. Electrostatic attraction between the polar head groups of the protonated amine and the deprotonated phosphate groups hold the alkylamine molecules between the layers. In this chapter, the use of a dimethylhexadecylamine (DHDA) intercalated zirconium phosphate as a potential sorbent for 4-chlorophenol is reported.

Although the main focus will be on DHDA intercalated ZrP, results from other alkylamine intercalated products will be discussed. The efficiency of ZrP-DHDA as a sorbent was evaluated using sorption kinetics and equilibrium adsorption isotherms.

5.2 Experimental

5.2.1 Materials

Chlorophenol (99 %) was purchased from Sigma-Aldrich and used without purification, Zirconium phosphate (ZrP), ZrP-DHDA and ZrP-BA were synthesized as described in chapter 4.

5.2.2 Sorption Isotherms and Kinetics

The equilibrium adsorption isotherms of α-ZrP as well as ZrP-DHDA were determined by preparing solutions of 4-chlorophenol ranging from 5 ppm to 3000 ppm in distilled water using a batch technique. α-ZrP or ZrP-DHDA (0.1 g) and chlorophenol (30 ml) solutions were reacted in glass bottles in a shaking bath, kept at a constant temperature, for 24 hrs to allow equilibrium adsorption. The shaking speed was 300 strokes per minute. The suspension in each glass bottle was then filtered and concentration of 4-chlorophenol was determined by UV-Vis analysis. A calibration curve in the range 0 to 10 mg/L of 4-chlorophenol was constructed using the maximum absorption at 225 nm. The amount of 4-chlorophenol remaining in solution was determined using the calibration curve. The 4-chlorophenol uptake at equilibrium, q_e (mg/g) was calculated using equation 5.1,[47]

$$q_e = \frac{(C_0 - C_e)V}{W} \qquad 5.1$$

Where C_0 and C_e (mg/L) are the liquid phase concentration of 4-chlorophenol at initial and at equilibrium, respectively. V (L) is the volume of solution and W (g) is the mass of adsorbent (ZrP-DHDA or α-ZrP) used. For kinetics experiments, 0.1 g of ZrP-DHDA was contacted with 30 ml of 4-chlorophenol in the 15 mg/L to 25 mg/L concentration range. At predetermined time intervals, the suspensions were filtered and the concentration of 4-chlorophenol was determined using UV-vis absorption. The amount of 4-chlorophenol adsorbed, q_t (mg/g) at time *t* (min) was calculated using equation 5.2,[47]

$$q_t = \frac{(C_0 - C_t)V}{W} \qquad 5.2$$

Where C_t (mg/L) is the concentration of 4-chlorophenol at time *t*.

5.2.3 Analytical Techniques

Powder X-ray diffraction measurements were obtained with a Rigaku Miniflex II diffractometer as described in Chapter 2. Infrared absorption spectrum of α-ZrP and ZrP-DHDA was obtained using a Perkin Elmer Spectrum 100 Fourier Transform Infrared (FTIR) spectrometer equipped with a single reflection ZnSe attenuated total reflectance (ATR) accessory from Pike Technology. Solids were pressed on the ATR accessory. Infrared spectra were recorded at a resolution of 2 cm^{-1}, averaged over 8 scans, in the

range 675-4000 cm^{-1}. UV-vis absorption spectrum of 4-chlorophenol was obtained using Perkin Elmer Lambda 35 UV-Vis spectrometer.

5.3 Results and Discussion

5.3.1 Powder X-Ray Diffraction Analysis

Synthesis of α-ZrP was confirmed by X-ray diffraction. Fig. 5. 1 shows the X-ray diffraction pattern of α-ZrP and dimethylhexadecylamine intercalated zirconium phosphate (ZrP-DHDA). The (*002*) peak for ZrP (Fig. 5.1) was used to calculate the interlayer space using Bragg's law.[71] The *002* peak for α-ZrP (Fig.5.1, Trace a) at 2 theta value of 11.7^0 indicates an interlayer space of 0.76 nm. Trace b shows that upon intercalation of dimethylhexadecylamine (DHDA) the *002* peak in ZrP shifts to a 2 theta value of 3.2^0 corresponding to an interlayer distance of 2.76 nm. The increase in interlayer space due to DHDA intercalation is consistent with DHDA molecules that form an interdigitated arrangement in the interlayer space. This arrangement was confirmed using computational calculations as described in Chapter 4. The insert in Fig.5.1 shows the XRD patterns of ZrP-DHDA and the product of chlorophenol intercalated in ZrP-DHDA (Trace c).

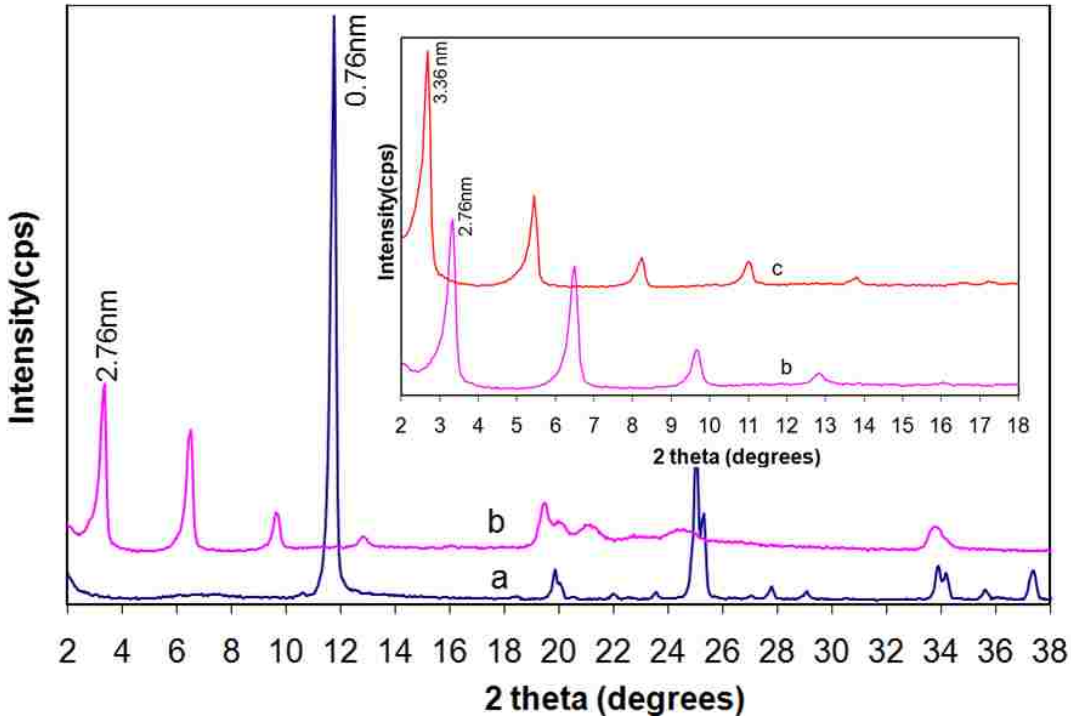

Figure 5.1 Powder X-ray diffraction pattern of α-ZrP (a) ZrP-DHDA (b). Insert shows the X-ray diffraction patterns of ZrP-DHDA (b) and ZrP-DHDA intercalated with chlorophenol(c) in the $2^0 - 20^0$ two theta range

The interlayer space increases from 2.76 nm (Trace b) to 3.36 nm (Trace c) upon intercalation of 4-chlorophenol. The length of 4-chlorophenol obtained from computation calculations is 0.63 nm. The increase in the interlayer space shown in the insert in Trace c is consistent with intercalation of 4-chlorophenol oriented perpendicular to the layers. Results in Trace c also suggest that chlorophenol and dimethylhexadecylamine molecules are co-intercalated in the ZrP interlayer spaces.

5.3.2 Adsorption Kinetics

Kinetic studies for the removal of chlorophenol were carried out to evaluate the efficiency of the ZrP-DHDA adsorbent. Four models of adsorption kinetics were used to

fit the experimental data: (i) the pseudo-first order model (Lagergren),[7] (ii) the pseudo-second order model, [140] (iii) a modified multiplex model, and (iv) a double-exponential model.[141] These models are commonly used to study adsorption in the liquid phase. The pseudo first order rate expression is given by equation 5.3:

$$\frac{dq_t}{dt} = k_1(q_e - q_t) \qquad 5.3$$

where k_1 (min^{-1}) is the pseudo-first order rate constant of adsorption, q_e (mg/g) is the amount of chlorophenol adsorbed at equilibrium and q_t (mg/g) is the amount of chlorophenol adsorbed at time *t*. After integration, with initial conditions $q_t = 0$ at time t = 0, the equation becomes:

$$q_t = q_e(1 - e^{-k_1 t}) \qquad 5.4$$

The pseudo-second order kinetic expression is expressed by the equation

$$\frac{dq_t}{dt} = k_2(q_e - q_t)^2 \qquad 5.5$$

where k_2 (g/mg/min) is the pseudo-second order rate constant of adsorption. The following integrated form is obtained:

$$q_t = q_e(1 - \frac{1}{k_2 q_e t + 1}) \qquad 5.6$$

A modified multiplex model based on the combination of the models assumes that the adsorption process has two steps (one fast and one slow);

$$\frac{dq_t}{dt} = k_{m1}(q_e - q_t) + k_{m2}(q_e - q_t)^2 \qquad 5.7$$

Where k_{m1} and k_{m2} are the rate constants of the rapid step (min^{-1}) and the slow step (g/mg/min), respectively. The integrated form of this equation can be expressed as

$$q_t = q_e - \frac{k_1 q_e}{(k_2 q_e + k_1)e^{k_1 t} - k_2 q_e} \qquad 5.8$$

The above kinetic models were used to calculate the rate coefficients for the purpose of evaluating the adsorbent.

The fourth model based on a double exponential was reported by Wilczak and Keinath[142] for the two-step kinetics of adsorption of Copper (II) and lead (II) on activated carbon. The mathematical expression for the two step contribution to the amount of adsorbed chlorophenol is given by:

$$q_t = q_{e1}(1 - e^{-k_{d1}t}) + q_{e2}(1 - e^{-k_{d2}t}) \qquad 5.9$$

where q_{e1} and q_{e2} are the amount of adsorbed chlorophenol in the rapid and the slow step respectively, k_{d1} and k_{d2} are the rate parameters (min^{-1}).

Non linear regression analysis was performed on the four kinetic models in order to determine the model which best fit the experimental results. The correlation coefficient (R^2) and the chi-square value (χ^2) were used to discriminate between the models. Additionally, quantitative comparison of the applicability of the different models in fitting the experimental data was performed using a normalized standard deviation, ε(%),

$$\varepsilon(\%) = 100 \times \frac{\sum_{i=1}^{N} \left| \frac{q_{e,i,exp} - q_{e,i,cal}}{q_{e,i,\exp}} \right|}{N} \qquad 5.10$$

where $q_{e,\,exp}$ and $q_{e,,cal}$ represent the experimentally observed and calculated amount of adsorbed chlorophenol respectively, and *n* is the number of data points.

Results of the time dependent chlorophenol adsorption are presented in Fig. 5.2 to Fig.5.5 along with the kinetic parameters for fitting the experimental data to the aforementioned models. Fig.5.2 shows the time dependent adsorption of chlorophenol fitted to a pseudo-first order kinetic model.

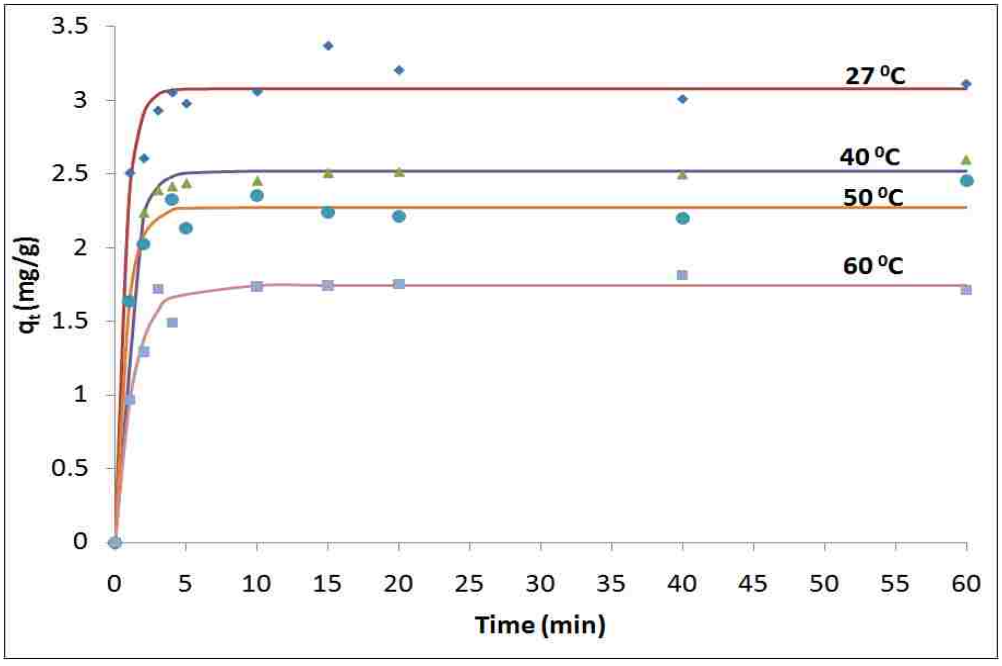

Figure 5.2 Amount of chlorophenol adsorbed by 0.1 g of ZrP-DHDA as a function of time at the temperatures indicated. Volume of chlorophenol used was 30 ml at an initial concentration of 25 mg/L. Solid lines represent non-linear fitting of the pseudo-first order kinetic model to experimental data

The amount of chlorophenol adsorbed reaches equilibrium within 10 minutes. The maximum adsorbed amount decreases as the temperature increases. This negative temperature dependency is an indication of weak van-der Waals or hydrogen bonding interactions between the adsorbent and the sorbates.[11,12] As the temperature increases these weak forces get disrupted and the amount of chlorophenol adsorbed decreases. Adsorption maximum adsorption capacity of ZrP-DHDA decreases from 3.07 mg/g to 1.74 mg/g as shown in Table 5.1 where the kinetic and statistical parameters of the pseudo-first order kinetic model are summarized. Fig.5.3 shows the experimental data fitted to a pseudo second order model. The kinetic and statistical parameters are summarized in Table 5.2. Fig.5.4 and Fig.5.5 show the experimental data fitted to a modified multiplex kinetic model and the double exponential model respectively.

Table 5.1 Kinetic and statistical parameters of the pseudo-first order kinetic model

Temp		Pseudo-first order				
	$q_{e,\,exp}$ (mg g^{-1})	$q_{eq,\,cal}$ (mg/g)	k_1 (min^{-1})	R^2	χ^2	ε(%)
27	3.15	3.07	1.44	0.9843	0.2438	5.42
40	2.48	2.52	1.04	0.9948	0.0581	1.82
50	2.19	2.27	1.23	0.9818	0.0769	4.84
60	1.68	1.74	0.77	0.9887	0.0648	5.20

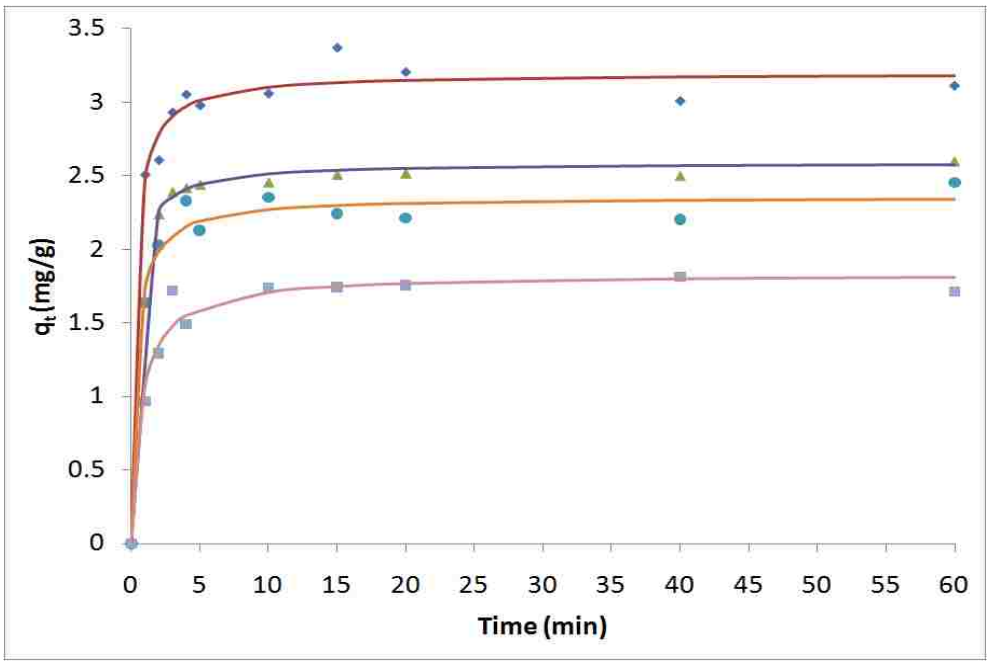

Figure 5.3 Amount of chlorophenol adsorbed by 0.1 g of ZrP-DHDA as a function of time at the temperatures indicated. Volume of chlorophenol used was 30 ml at an initial concentration of 25 mg/L. Solid lines represent non-linear fitting of the pseudo-second order kinetic model to experimental data

Table 5.2 Kinetic and statistical parameters of the pseudo-second order kinetic model

Temp (^{0}C)	Pseudo-second order					
	$q_{e,\ exp}$ (mgg^{-1})	$q_{eq,\ cal}$ (mg/g)	k_2 (g/mgmin)	R^2	χ^2	ε(%)
27	3.15	3.19	1.03	0.9923	0.1331	3.81
40	2.48	2.58	1.29	0.9969	0.0353	1.41
50	2.19	2.36	1.14	0.9981	0.0921	3.32
60	1.68	1.83	0.75	0.9850	0.0648	6.03

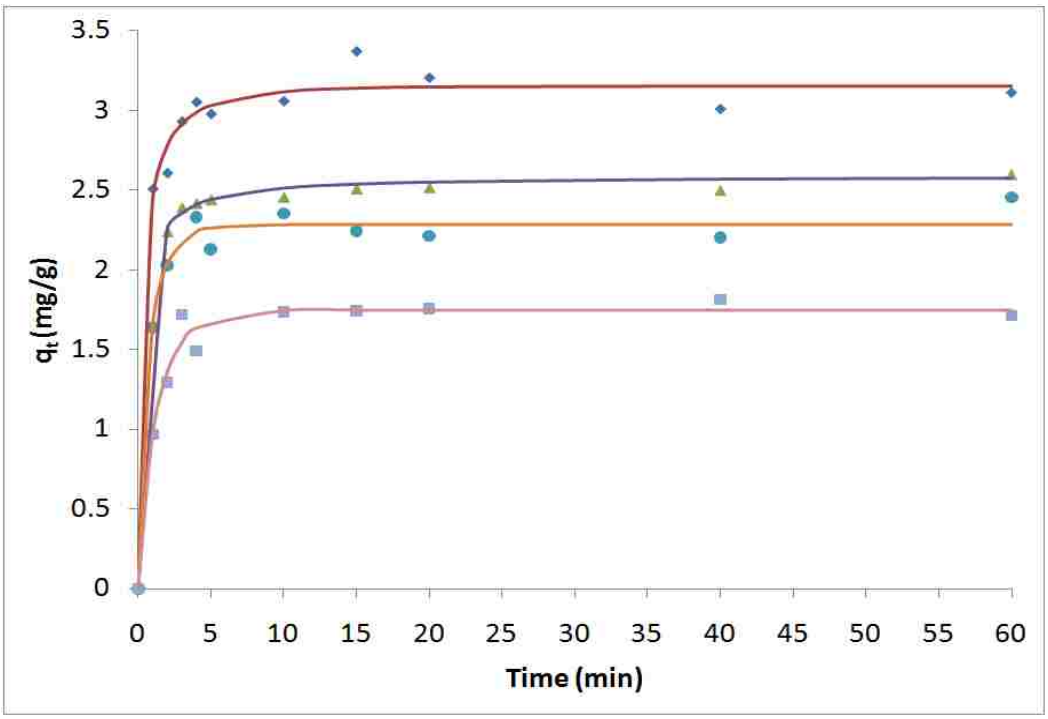

Figure 5.4 Amount of chlorophenol adsorbed by 0.1 g of ZrP-DHDA as a function of time at the temperatures indicated. Volume of chlorophenol used was 30 ml at an initial concentration of 25 mg/L. Solid lines represent non-linear fitting of the modified multiplex kinetic model to experimental data

Table 5.3 Kinetic and statistical parameters of the modified multiplex model

Temp (^{0}C)	Modified Multiplex Model					
	$q_{eq,\ cal}$ (mg/g)	k_{m1} (min^{-1})	k_{m2} (g/mg min)	R^2	χ^2	ε(%)
27	3.15	1.84	0.907	0.9927	0.1248	3.33
40	2.59	1.25	0.89	0.9969	0.0353	1.53
50	2.28	0.80	0.38	0.9921	0.0738	3.22
60	1.74	0.58	0.18	0.9891	0.0628	4.81

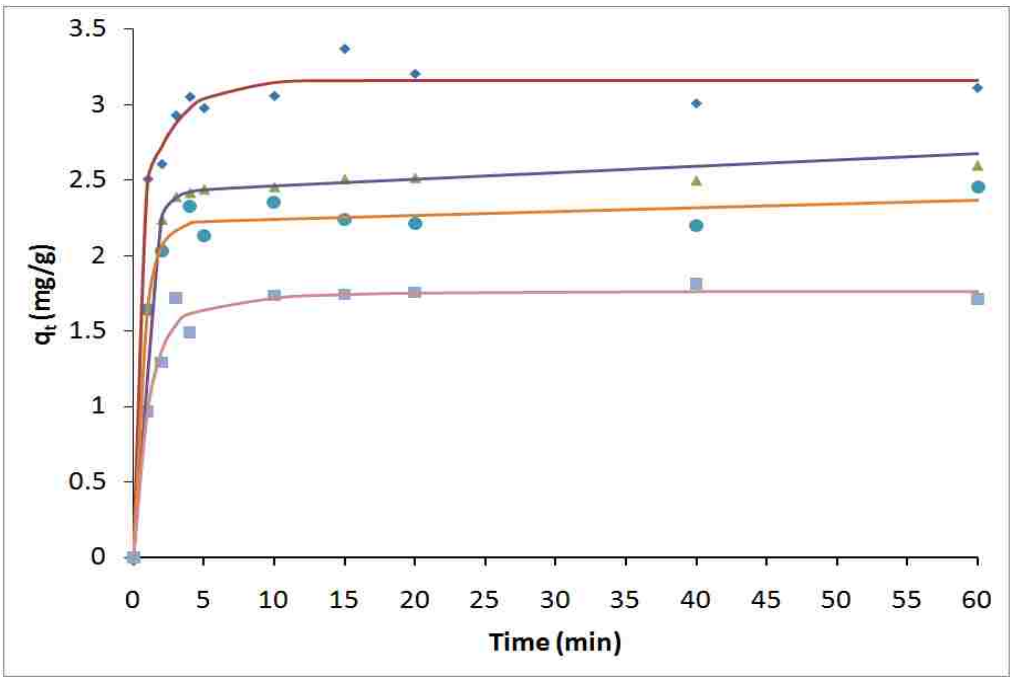

Figure 5.5 Amount of chlorophenol adsorbed by 0.1 g of ZrP-DHDA as a function of time at the temperatures indicated. Volume of chlorophenol used was 30 ml at an initial concentration of 25 mg/L. Solid lines represent non-linear fitting of the double exponential model to experimental data

Table 5.4 Kinetic and statistical parameters of the double exponential model

Temp	Double Exponential Model						
	$q_{e1,\,cal}$ (mgg^{-1})	$q_{e2,\,cal}$ (mgg^{-1})	k_{d1} (min^{-1})	k_{d2} (min^{-1})	R^2	χ^2	ε(%)
27	2.11	1.05	2.84	0.44	0.9939	0.1061	5.42
40	2.42	3.04	1.29	0.0015	0.9989	0.0403	1.82
50	2.21	2.33	1.32	0.0011	0.9936	0.0601	3.84
60	1.58	0.18	0.90	0.1454	0.9896	0.0596	5.20

Results presented here show that the data can be described by two-step models as the pseudo-first order model had correlation coefficients that were not as good as the other three models. This suggests that the adsorption of chlorophenol is not a simple first order reaction but may be a pseudo-second order reaction. The parameters of the modified multiplex parameter model show that the rate constant of the first step is much higher than the rate constant of the second step, suggesting that the process involves a rapid step followed by a slow step. It is also noted that at a temperature of 60 ^{0}C, the correlation coefficients and the normalized standard deviation indicate that the models do not fit the experimental data as well as they do for the lower temperatures. The fitted data for all the four kinetic models are plotted on the same graph for the experiment at 27 ^{0}C as shown in Fig. 5.6. This compares the goodness of fit for the models

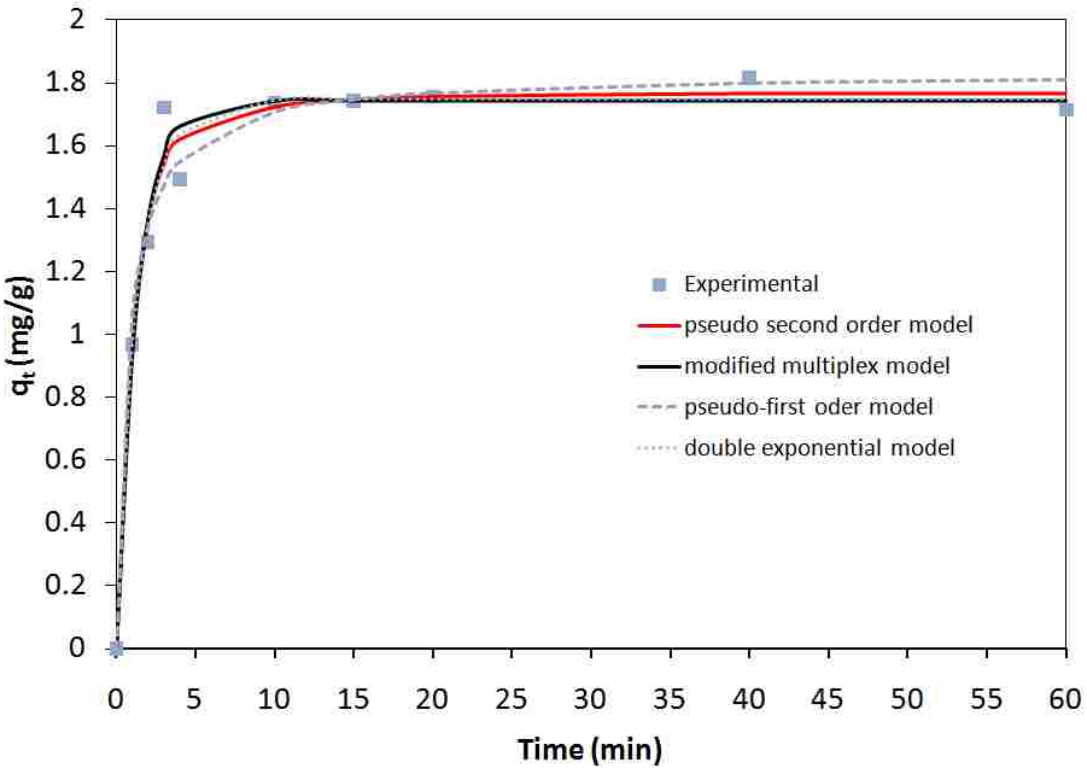

Figure 5.6 Amount of 4-chlorophenol adsorbed by 0.1 g of ZrP-DHDA as a function of time at 27 ^{0}C. The lines represent the kinetic models used to describe the experimental data

The effect of the initial concentration of 4-chlorophenol on the adsorption kinetics was studied using three different initial concentrations at a temperature of 26 ^{0}C. The initial concentrations used were 15 mg/L, 20 mg/L and 25 mg/L. Fig.5.7 shows the amount of 4-chlorophenol adsorbed as a function of time at using different initial chlorophenol concentrations.

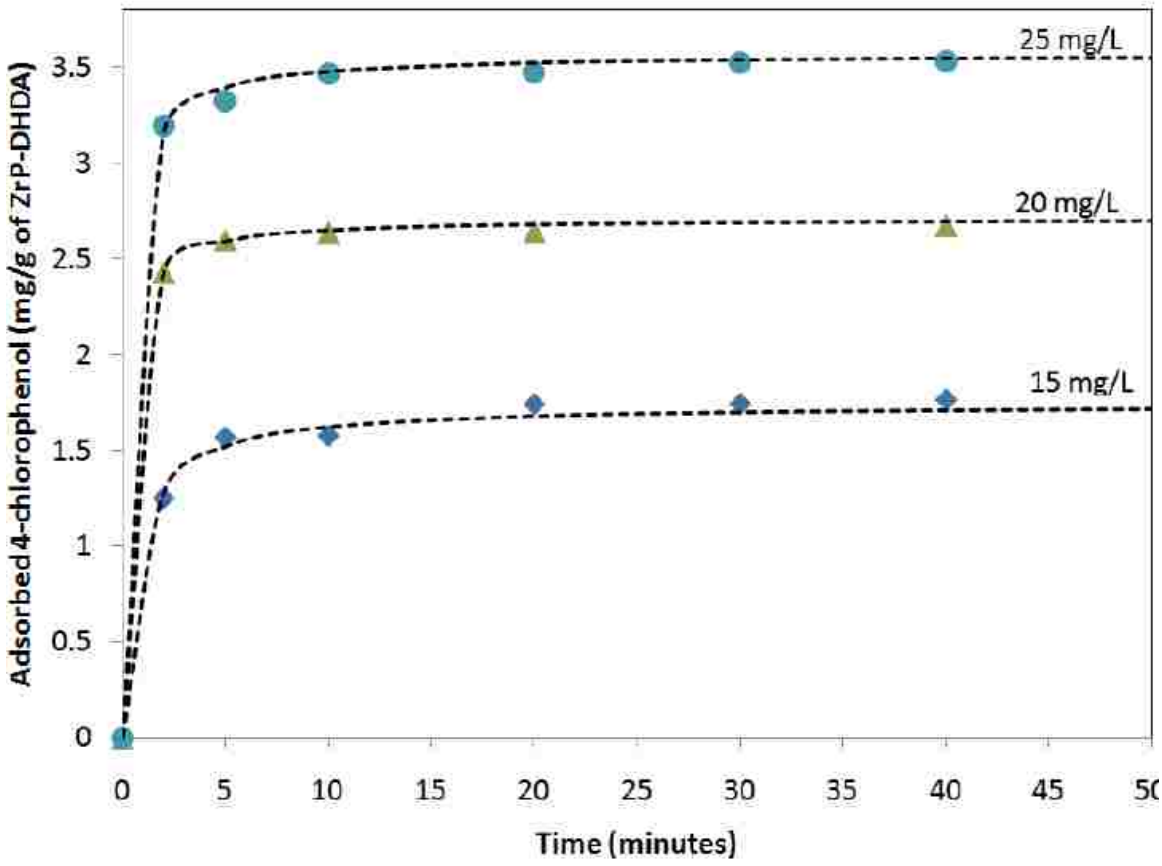

Figure 5.7 Amount of 4-chlorophenol adsorbed by 0.1 g of ZrP-DHDA in 30 ml of solution as a function of contact time for various chlorophenol initial concentrations. Dotted lines represent non -linear fit of experimental data to pseudo-second order kinetics model Amount of 4-chlorophenol adsorbed by 0.1 g of ZrP-DHDA in 30 ml of solution as a function of contact time for various chlorophenol initial concentrations. Dotted lines represent non -linear fit to pseudo-second order kinetics model

Table 5.5 Kinetic and statistical parameters of the pseudo-second order kinetic model for concentration dependent experiment

Initial Chlorophenol concentration (mg/L)	pseudo-second order kinetic model					
	$q_{e,\ exp}$ (mg/g)	$q_{e,\ calc}$ (mg/g)	k_2 (g/ mg. min)	R^2	χ^2	ε(%)
15	1.6±0.2	1.74±0.02	1.4±0.2	0.9947	0.0124	1.98
20	2.62±0.03	2.707±0.007	2.3±0.3	0.9998	0.0368	1.27
25	3.53±0.31	3.6±0.2	3.57±0.02	0.9992	0.0758	1.33

The maximum adsorption capacity of ZrP-DHDA increases with increasing initial concentration as shown in Table 5.5. When the initial concentration of 4-chlorophenol is 15 mg/L, the maximum adsorption capacity, q_e is 1.6 ± 0.2 mg/g. Increasing the initial concentration to 25 mg/L results in the maximum adsorption capacity increasing to 3.53 ±0.03 mg/g. This increase in maximum adsorption capacity with increasing initial concentration, suggests cooperative adsorption among the adsorbed chlorophenol molecules. The rate of adsorption also increases with increasing initial concentration as indicated by k_2 values in Table 5.5.

5.3.3 Adsorption Isotherms

The equilibrium adsorption capacities of the alkylamine intercalated zirconium phosphate compounds were estimated using equilibrium adsorption studies in the concentration range 5 mg/L to 3000 mg/L of 4-chlorophenol. The unmodified ZrP was

compared with the BA, Octyl, and DHDA intercalated ZrP. Fig. 5.8 shows the equilibrium adsorption isotherms of ZrP, ZrP-BA, ZrP-Octyl and ZrP-DHDA at 26 ^{0}C.

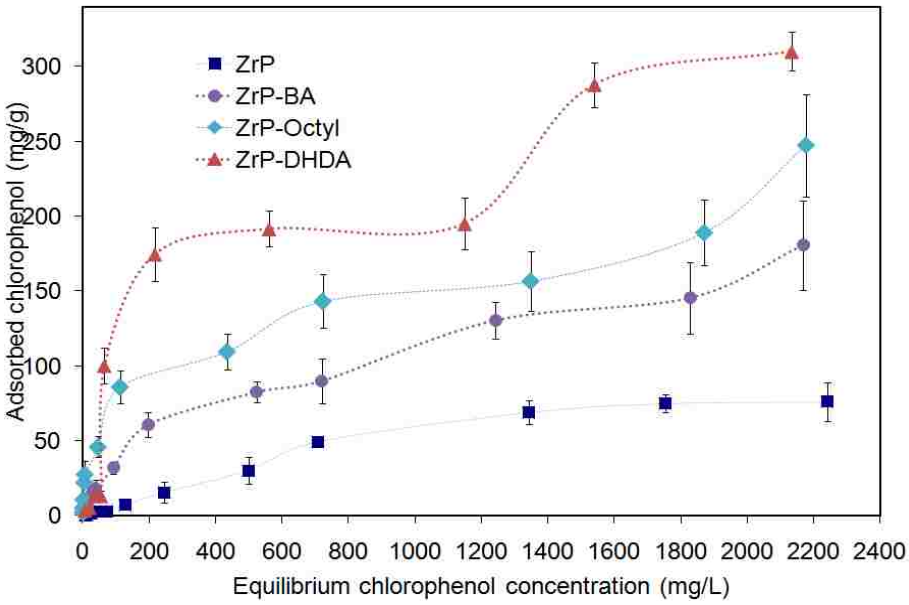

Figure 5.8 Equilibrium Sorption isotherms for 4-chlorophenol onto Zirconium phosphate (ZrP) butylamine modified zirconium phosphate (ZrP-BA), octylamine modified zirconium phosphate (ZrP-Octyl) and dimethylhexadecylamine modified zirconium phosphate (ZrP-DHDA) at 26 ^{0}C. The initial concentrations ranged from 5 mg/L to 3000 mg/L.

The unmodified Zirconium phosphate (ZrP) has low affinity for 4-chlorophenol due to the hydrophilicity of the phosphate surfaces. The adsorption of 4-chlorophenol by ZrP is assumed to take place on the surface of the layered material because X-ray diffraction analysis revealed no change of the interlayer space upon chlorophenol adsorption. Intercalation of ZrP with alkylamines makes it more hydrophobic. The organically modified layered material acts as a partitioning medium allowing 4-chlorophenol to partition from the aqueous medium into the organic medium. The amount of 4-chlorophenol adsorbed by the alkylamine modified ZrP increases from butylamine

intercalated ZrP to dimethylhexadecylamine intercalated ZrP as shown in Fig 5.8. The 2 stage processes exhibited by ZrP-DHDA may suggest that both surface adsorption and intercalation of 4-chlorophenol into the layered material occur in this material. Results in Fig.5.8 as well as a previously reported study on the adsorption of phenols by butylamine intercalated ZrP[69] suggest that ZrP-DHDA is a better adsorbent of chlorophenol than ZrP-BA and the other primary amine intercalated ZrP. We attribute this difference to the arrangement of the alkylamines in the layered ZrP. The arrangement of alkylamines was schematically represented in Fig.4.4 and Fig.4.5 for ZrP-DHDA and ZrP-BA, respectively. Butylamine molecules are tightly packed within the layer space, while dimethylhexadecylamine have more free space through which the chlorophenol molecules can diffuse. The interlayer porosity in ZrP-DHDA is greater than in ZrP-BA as shown by Fig.4.4 and fig.4.5The use of ZrP-DHDA as a sorbent for 4-chlorophenol was therefore the focus of this study, other alkylamine intercalated compounds are presented for comparison purposes.

The sorption isotherm models used in this study could not describe the entire concentration range shown in Fig.5.8. A lower concentration range was chosen to study the adsorption behavior of ZrP-DHDA. The adsorption isotherms for 4-chlorophenol onto α-ZrP and dimethylhexadecylamine intercalated zirconium phosphate (ZrP-DHDA) were used to study the effect of dimethylhexadecylamine in ZrP on the sorption of 4-chlorophenol. Fig. 5.9 shows the adsorption isotherm of 4-chlorophenol onto α-ZrP using initial chlorophenol concentration range of 5 mg/L to 800 mg/L. Three common adsorption models (Langmuir, Freundlich and the BET adsorption isotherm for liquid phase adsorption[143]) were used to describe the equilibrium between adsorbed 4-

chlorophenol (q_e) on ZrP and 4-chlorophenol in solution (C_e) at constant temperature. The Langmuir isotherm given by equation 5.11 is known to be valid for monolayer sorption onto a homogeneous surface with a finite number of identical sites. [143]

$$q_e = \frac{\beta K_L C_e}{(1 + K_L C_e)} \qquad 5.10$$

where q_e amount adsorbed at equilibrium, β is the maximum adsorption capacity per unit mass of adsorbent (mg/g) and K_L is the affinity constant (L/mg). The Langmuir sorption maximum β, represents the practical limiting adsorption capacity when the surface is fully covered with 4-chlorophenol and allows the comparison of adsorption performance, particularly where the sorbent did not reach its full saturation in experiments.[43,50,144]

The empirical Freundlich equation based on a monlayer adsorption by the adsorbent with a heterogeneous energy distribution is given by equation 5.12

$$q_e = K_f C_e^n \qquad 5.12$$

where q_e and C_e are as defined in equation 5.10, K_f and *n* are the Freundlich constants characteristic on the system. They are indicators of adsorption capacity and adsorption intensity, respectively.[43] The Freundlich isotherm is also widely used but provides no information on the monolayer adsorption capacity, in contrast to the Langmuir isotherm.[145] The three-parameter BET model for liquid phase adsorption has been proposed to improve the fit by Langmuir or Freundlich isotherm where adsorption occurs on more than one type of adsorption sites and is given by equation 5.13,[146]

$$q = q_m \frac{K_s C_{eq}}{(1 - K_L C_{eq})(1 - K_L C_{eq} + K_s C_{eq})} \quad 5.13$$

where q_m is the monolayer adsorption capacity of the adsorbent in mg/g, K_s is the equilibrium adsorption constant of the first layer and K_L is the equilibrium adsorption constant of the upper layers and C_{eq} is the equilibrium concentration of 4-chlorophenol in solution. The experimental data was fitted to equations 5.11 to 5.13 to evaluate the sorption capacity of ZrP as shown Fig.5.9. The adsorption constants for the different isotherms are obtained by non-linear regression analysis for each model and listed in Table 5.7 with average percentage errors. The average percent errors between the experimental and predicted values are calculated using equation 5.10.

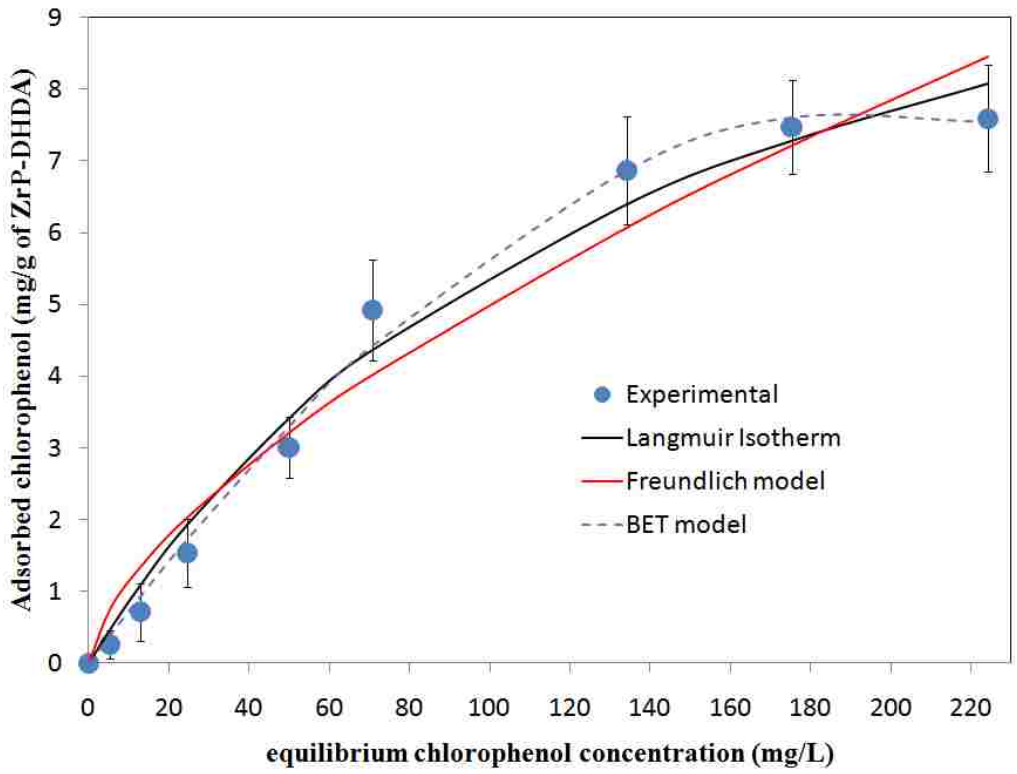

Figure 5.9 Adsorption isotherm for chlorophenol onto ZrP at 26 ^{0}C. Initial concentrations of chlorophenol ranged from 0 to 800 mg/L

Table 5.6 Comparison of the Freundlich, Langmuir and BET adsorption constants on the adsorption of 4-chlorophenol on ZrP.

Freundlich model				
K_f $[(mg/g)(mg/L)]^{-1/n}$	n	ε (%)	R^2	
0.3±0.1	0.64±0.08	36.9	0.9773	
Langmuir model				
K_L(L/ mg)	Q (mg/g)	ε (%)	R^2	
0.007 ±0.002	13.39 ± 1.7	19.9	0.9873	
BET model				
K_s (L/mg)	K_L (L /mg)	Q (mg/g)	ε (%)	R^2
0.004±0.002	0.0005±0.0001	23±6	11.7	0.9923

This type of adsorption shown in Fig.5.9 is typical of surface adsorption where the curvature shows that as more sites in the substrate are filled, it becomes increasingly difficult for more solute molecules to find vacant adsorption sites. In view of the values of percentage errors in Table 5.6, the BET isotherm exhibited the best fit to the adsorption data at the temperature reported. However, the Langmuir also seems to agree with experimental data to a reasonable extent. The maximum adsorption capacity for the adsorption of 4-chlorophenol as obtained from the BET model is 23±6 mg/g as shown in Table 5.6. The K_s and K_L values reported in Table 5.6 suggest that the adsorption occurs at two different types of sites or layers with the first layer having a higher affinity constant than the subsequent layer.

However, upon intercalation of DHDA into ZrP, the adsorption isotherm shows a different type of adsorption mechanism as shown in Fig. 5.10. For the same concentration range as shown in Fig. 5.9 , ZrP-DHDA shows an S type of adsorption isotherm.[143] The initial upward curvatures exhibited by isotherms at 26 ^{0}C and 32 ^{0}C in Fig. 5.10 are typical of adsorption processes that become easier as the concentration of 4-chlorophenol increases. This has been attributed to cooperative adsorption among the sorbates.[143]

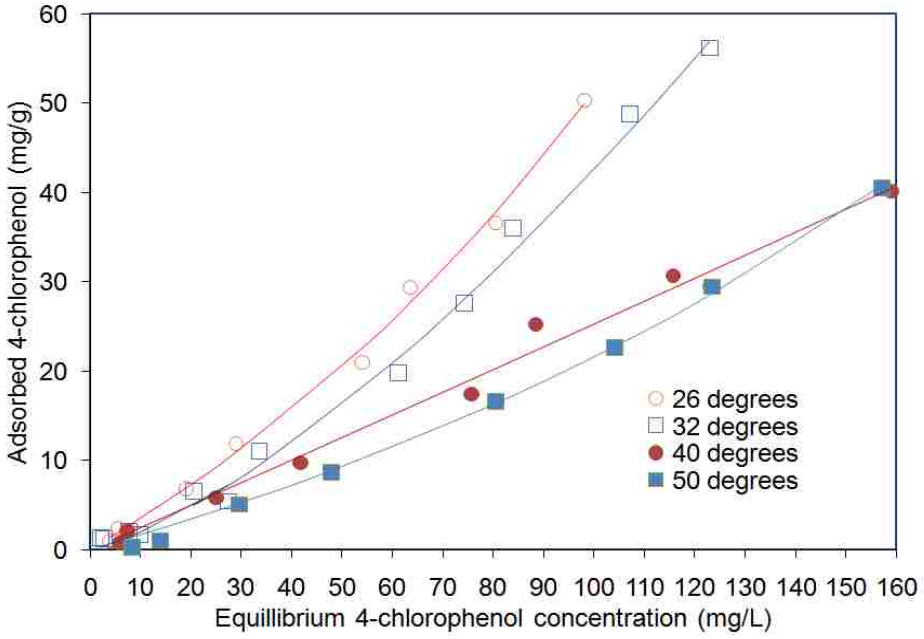

Figure 5.10 S-type adsorption isotherms for 4-chlorophenol onto ZrP-DHDA at different temperatures. Initial concentrations ranged from 0 to 800 mg/L. Solid lines represent BET isotherms for liquid phase adsorption.

The different isotherm shapes in Fig.5.9 and Fig.5.10 suggest that the mechanism of 4-chlorophenol adsorption onto α-ZrP is different from its adsorption onto ZrP-DHDA. This difference is attributed to the presence of organic DHDA in the ZrP-DHDA adsorbent that makes it more hydrophobic than α-ZrP. This increased hydrophobic

character increases the affinity of 4-chlorophenol for ZrP-DHDA. The negative temperature dependence of the adsorption of 4-chlorophenol onto ZrP-DHDA reported in section 5.3.2 is also observed in Fig. 5.10 for the adsorption isotherms in the temperature range 26 ^{0}C to 50 ^{0}C. Physical interactions again are proposed to apply for sorption isotherms in Fig.5.10. The S type isotherms shown in Fig.5.10 were well described by a BET isotherm (equation 5.11) for liquid phase adsorption. Table 5.7 summarizes the parameters obtained when the experimental results in Fig. 5.10 were fit to equation 5.11.

Table 5.7 BET parameters for the adsorption of 4-chlorophenol onto ZrP-DHDA at various temperatures

Temperature (degrees C)	q_m	K_s	K_L	R^2
26	208±12	0.0016±0.0004	0.003±0.001	0.99815
32	135±18	0.0013±0.0001	0.0021±0.0003	0.99625
40	79 ±8	0.0015±0.0003	0.0019±0.0005	0.99506
50	68±5	0.0006±0.0001	0.0027±0.0003	0.99926

The maximum amount of 4-chlorophenol adsorbed, q_m, decreases as temperature increases from 26 ^{0}C to 50 ^{0}C. The affinity constants K_s and K_L do not show a particular specific temperature dependence behavior.

The adsorption behavior exhibited in Fig.5.10 is typical of unsaturated adsorbent. At higher concentrations of 4-chlorophenol the isotherm at 26 ^{0}C shows a two stage process as shown in Fig.5.11. The plateau or beginning of a linear portion represents "first degree saturation" .[143] This suggests that the adsorption of 4-chlorophenol may

form more than one layer on the adsorbent sites. However, increasing the temperature results in the adsorption isotherm exhibiting an L shape (Langmuir) character as shown by the isotherm at 40 ^{0}C in Fig.5.11.

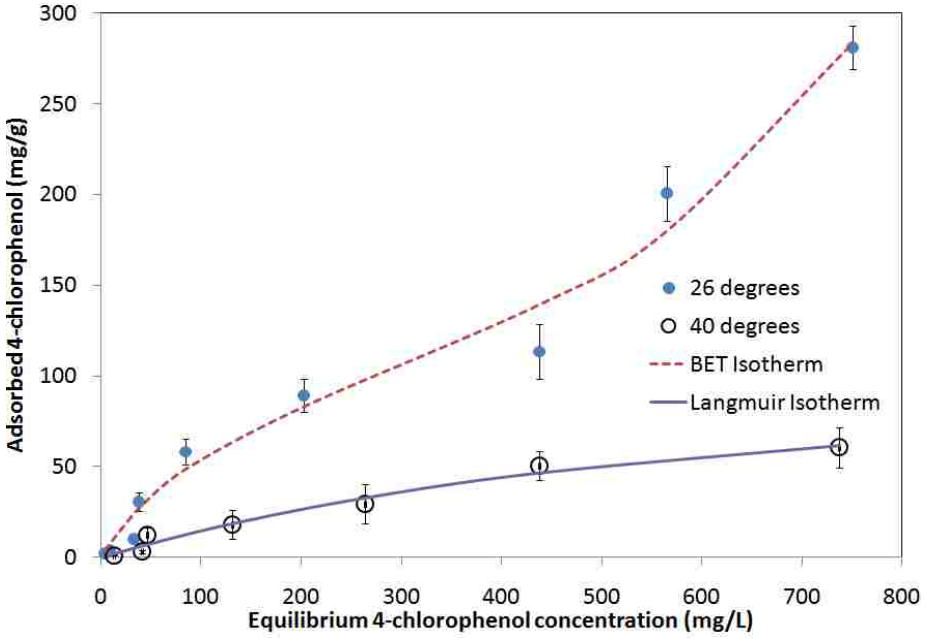

Figure 5.11 Adsorption of 4-chlorophenol onto ZrP-DHDA in the 0 to 2000 mg/L chlorophenol concentrations. Closed circles represent the adsorption isotherm for 26 degrees. Open circles represent the adsorption isotherm at 40 degrees.

The experimental data in Fig. 5.10 are described by two different isotherms. At 40 ^{0}C the data follow a Langmuir isotherm described by equation 5.11 with the Langmuir parameters K_L, as 0.0018 L /mg and q_m as 102 mg/g. At 26 ^{0}C the isotherm follows a BET isotherm described by equation 5.12. The values of the parameters calculated were 383 mg/g for the maximum adsorption capacity q_m, 0.0019 L/mg for the first layer affinity constant K_s and 0.0011 L/mg for the upper layer constant K_L. The maximum adsorption capacity of 383 mg/g for 4-chlorophenol obtained in this study is more than

twice the maximum adsorption capacity of 115 mg/g that was reported for adsorption of chlorophenol by butylamine intercalated zirconium phosphate (Zr-BA). [69]

5.3.4 XRD analysis

The adsorption of chlorophenol onto ZrP-DHDA was further elucidated by performing X-ray diffraction analysis on the solid materials recovered after reacting chlorophenol with ZrP-DHDA. The XRD patterns of the ZrP-DHDA obtained after sorption of 4-chlorophenol in the concentration range 0 to 2000 mg/L are shown in Fig.5.12.

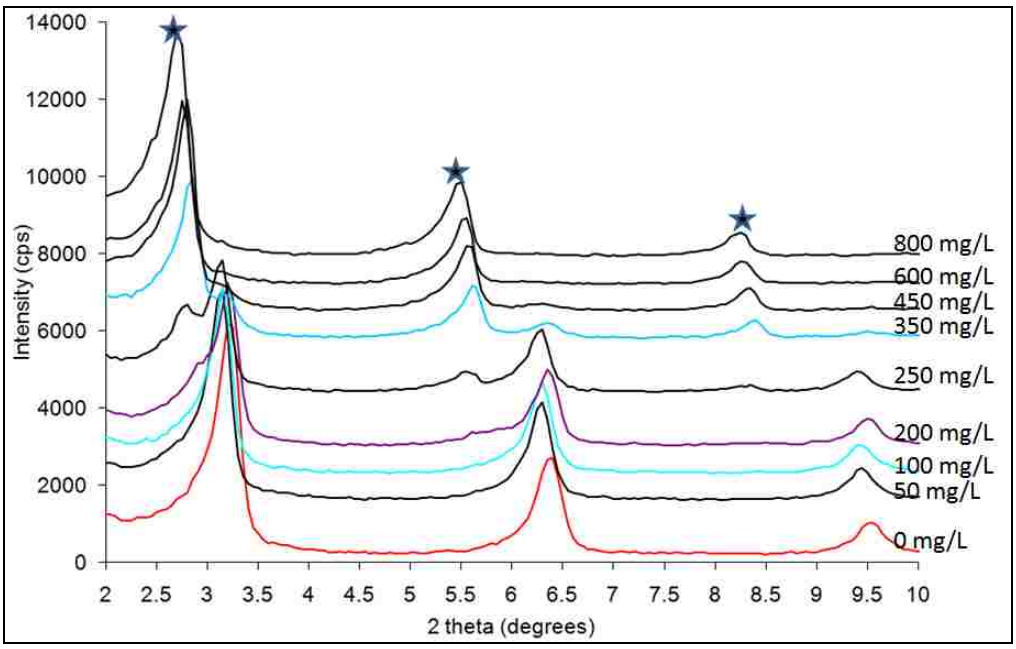

Figure 5.12 XRD patterns of the phases obtained after adsorption of 4-chlorophenol by 0.1 g of ZrP-DHDA in 30 ml of solution at different 4-chlorophenol concentrations. Stars represent the new phase due to 4-chlorophenol intercalation.

Solid materials recovered after the exposure to solutions with 4-chlorophenol concentration lower than 200 mg/L exhibit similar XRD patterns to that of the parent

material. This may suggest that at these concentrations if there is any intercalation of 4-chlorophenol in the interlayer space, it is not significant enough to affect the interlayer distance. However, when the 4-chlorophenol concentration is higher than 200 mg/L, the intercalation process becomes significant and impacts the interlayer distance of the solids which increases from 27.6 Å in [ZrP-DHDA] to 33.7 Å in the new phase [ZrP-DHDA-4-chlorophenol]. The increase in the interlayer space due to intercalation of 4-chlorophenol suggests that 4-chlorophenol is co-intercalated with dimethylhexadecylamine (DHDA) in the zirconium phosphate interlayer space.

The mechanism of chlorophenol intercalation was studied using higher concentrations of chlorophenol as shown in Fig.5.13. It is observed that upon intercalation of chlorophenol, a mixture of phases exist depending on the concentration of chlorophenol. We observed a gradual shift of the *002* peak to lower two theta values as the concentration of chlorophenol increases.

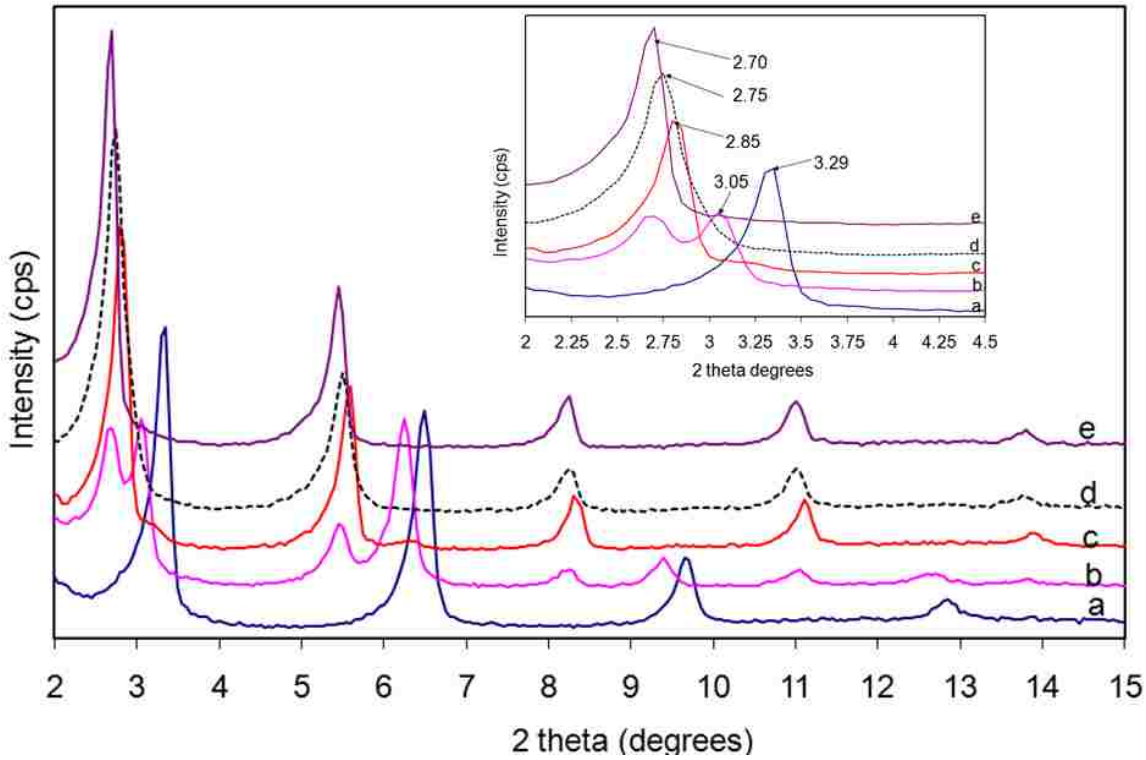

Figure 5.13 X-ray diffraction patterns for ZrP-DHDA (a) the intercalation of 4-chlorophenol in ZrP-DHDA at initial 4-chlorophenol concentration of 0.02 M (b) 0.04 M (c) 0.1 M (d) and 0.2 M (e). The insert shows the first peak (*002*) for the products. The gradual shift to lower 2 theta values is clearly shown in the insert.

This process in which mixtures of phases are obtained at different chlorophenol loadings is similar to the intercalation of amines in zirconium phosphate reported in the literature. It was reported that at low loadings the alkylamine lie parallel to the metal phosphate layers. As the loading increases, the alkylamines assume a more perpendicular orientation.[60,68, 119] We believe that the intercalation mechanism of 4-chlorophenol shown in Fig.5.13 is similar to the intercalation of primary amines in ZrP where a mixture of phases are observed depending on the concentration of 4-chlorophenol.

The intercalation of chlorophenol in butylamine intercalated zirconium phosphate exhibits a different behavior from what is shown in Fig.5.13. The increase in the interlayer spacing for the intercalation of 4-chlorophenol in ZrP-BA is shown in

Fig.5.14. Adsorption of chlorophenol by octylamine intercalated ZrP also show small d-space increases similar to butylamine.

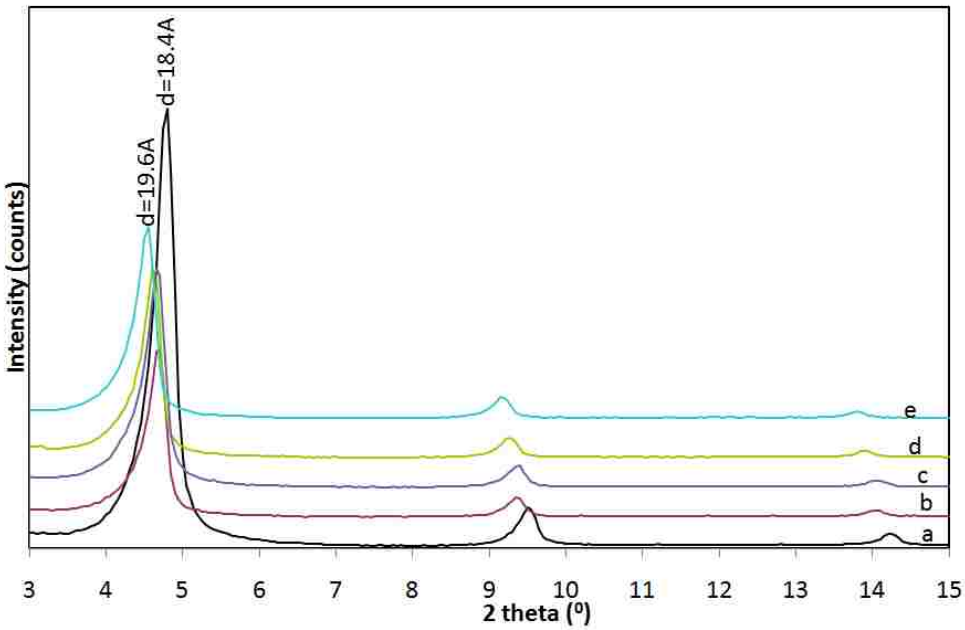

Figure 5.14 X-ray diffraction patterns for ZrP-BA (a) the intercalation of 4-chlorophenol in ZrP-BA at initial 4-chlorophenol concentration of 0.02 M (b) 0.04 M (c) 0.1 M (d) and 0.2 M (e). The insert shows the first peak (*002*) for the products. The gradual shift to lower 2 theta values is clearly shown in the insert.

The difference in the observed interlayer space increase between ZrP-BA and ZrP-DHDA upon intercalation of 4-chlorophenol is attributed to the differences in the arrangement of the alkylamines in the ZrP interlayer space. We reported in Chapter 4, that DHDA molecules form an interdigitated arrangement (see Fig.4.4.) that has more free space than BA molecules that form a bilayer arrangement (see Fig.4.5). We postulate that the arrangement in ZrP-DHDA allows 4-chlorophenol to diffuse easily as opposed to butylamine molecules which form a bilayer system with the molecules more tightly packed in the interlayer space.

5.3.4.1 Intercalation of chlorophenol isomers

In order to study the effect of chlorophenol structure on the adsorption of 4-chlorophenol by ZrP-DHDA, the X-ray diffraction patterns of the isomers of chlorophenol adsorbed in ZrP-DHDA were analyzed. The X-ray diffraction patterns of 4-chlorophenol, 3-chlorophenol and 2-chlorophenol intercalated in ZrP-DHDA are shown in Fig.5.15.

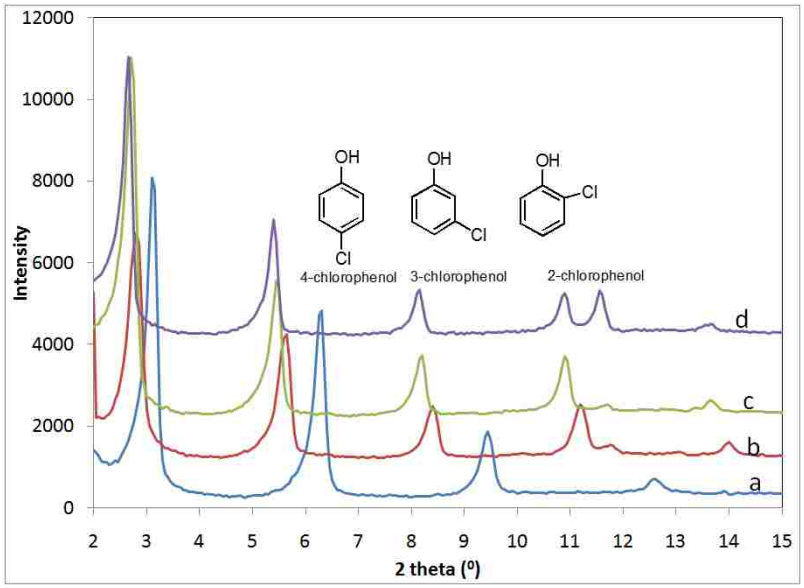

Figure 5.15 Powder XRD patterns for different isomers of chlorophenol. Insert shows the structures of the different isomers. The observed d-spacings are (a) 27.6 A for ZrP-DHDA, (b) 31.5 A for ZrP-DHDA with 2-chlorophenol (c) 32.7 A for ZrP-DHDA with 3-chlorophenol and (d) 33.3 A for ZrP-DHDA with 4-chlorophenol.

As can be observed in Fig. 5.15, the interlayer space increases observed for the intercalation of 2-, 3- and 4-chlorophenol depend on the position of the chlorine atom on the benzene ring. Fig.5.15 shows that the isomer with the largest increase in d-spacing is 4-chlorophenol while 2-chlorophenol has the least increase. A possible explanation is that

the hydroxyl part of 4-chlorophenol binds to the hydrophilic zirconium phosphate layer, while the chlorine atom binds to the more hydrophobic alkylamine part through a possible halogen-bonding interaction with the nitrogen group.[147] The XRD patterns in Fig.5.15 suggest that chlorophenol is co-intercalated with the DHDA molecules in the ZrP inter-layers space. This is because if there was exchange or substitution of the DHDA molecules by chlorophenol, we would expect a phase that is consistent with the size of the chlorophenol alone. The interlayer spaces observed in Fig.5.15 are consistent with the sum of chlorophenol and DHDA molecular size. All experiments in this study were carried out at pH around neutral and the pKa values of the different chlorophenols used are 9.38, 9.02 and 8.48, for para, meta and ortho-chlorophenol respectively.[148] Therefore all the isomers chlorophenol used were in their neutral state, an exchange would only be possible with a cationic chlorophenol.

The adsorption kinetics of the isomers was studied at 27 ^{0}C. This temperature was chosen because the adsorption was found to decrease with temperature. This experiment was carried out to study the effect of the position of chlorine atom on the adsorption kinetics of chlorophenols. Fig.5.16 shows the kinetics of adsorption of 4-chlorophenol, 3-chlorophenol and 2-chlorophenol by ZrP-DHDA at 27 ^{0}C.

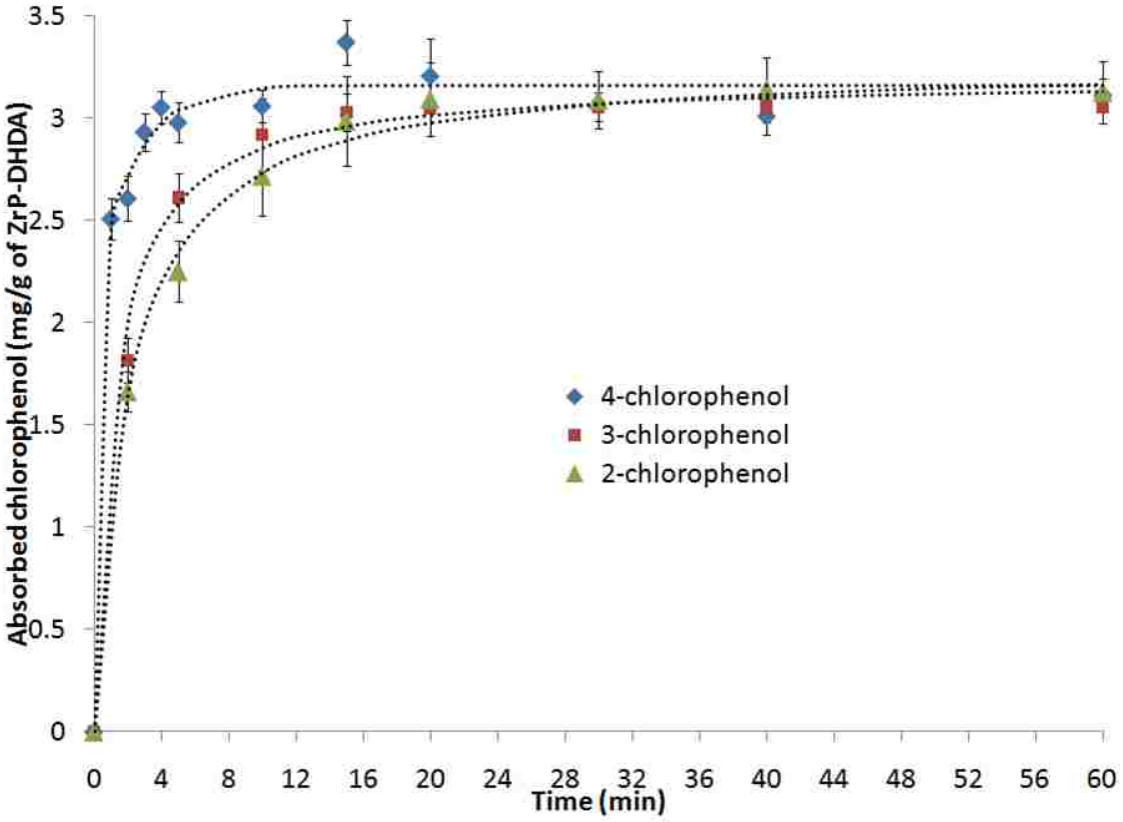

Figure 5.16 Adsorption kinetics of 3 isomers of chlorophenol by ZrP. Error bars represent standard deviation of 3 trials. Dotted lines represent pseudo-second order kinetic model.

The maximum amount of chlorophenol adsorbed for the three isomers is the same within experimental error. However, the rate of adsorption is faster for 4-chlorophenol than for 2-chlorophenol with 3-chlorophenol in the middle. Table 5.8 summarizes the parameters obtained after fitting the experimental data to the pseudo-second order model described by equation 5.6.

Table 5.8 Pseudo-second order kinetic parameters for the adsorption of chlorophenol isomers by ZrP-DHDA

Isomer	$q_{e,\ exp}$	Pseudo-second order				
		$q_{eq,\ cal}$	k_2			
	(mg/g)	(mg/g)	(g/mg min)	R^2	χ^2	ε(%)
4-chlorophenol	3.15	3.19±0.05	1.03±0.05	0.9923	0.1331	3.81
3-chlorophenol	3.18	3.26±0.09	0.81±0.03	0.9972	0.0469	1.08
2-chlorophenol	3.19	3.2±0.2	0.69±0.07	0.9932	0.0233	2.81

The chemical interaction of chlorophenol with ZrP-DHDA was studied using phenol and chlorobenzene. This analysis was carried out to study the role played by the hydroxyl or the chlorine atom in the binding of chlorophenol in ZrP-DHDA. Fig.5.17 shows the X-ray diffraction patterns of chlorobenzene, phenol and chlorophenol intercalated in ZrP-DHDA.

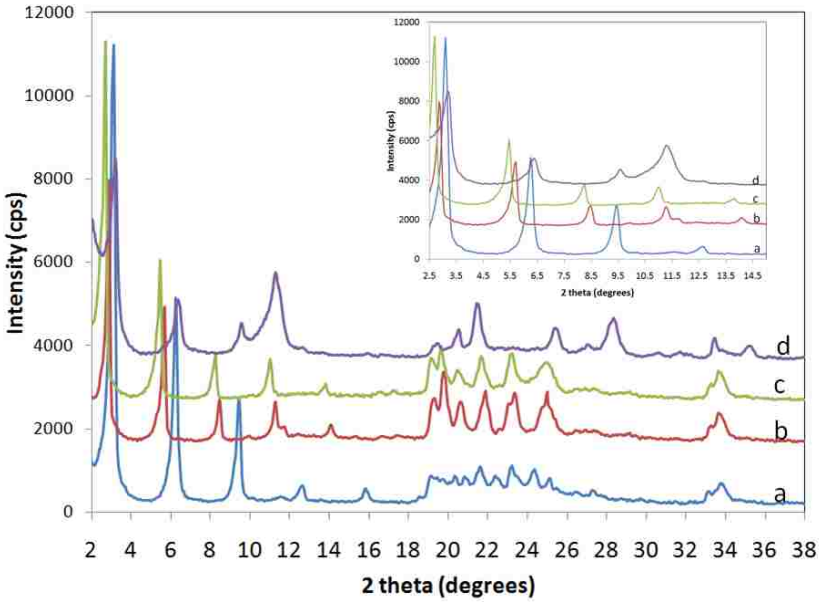

Figure 5.17 powder XRD patterns for ZrP-DHDA (a) intercalated with 0.4 M 4-chlorophenol (b), phenol (c) and chlorobenzene (d). Intercalation of phenol and chlorophenol results in increase in d spacing while chlorobenzene does not show increase in d-spacing.

If size is the main factor contributing to the increase in the interlayer spacing upon intercalation of chlorobenzene or phenol, we expect that both molecules will result in almost the same increases since they are of comparable size. The interlayer-space of ZrP-DHDA increases from 2.76 nm to 31.5 nm upon intercalation of phenol and to 33.6 nm upon intercalation of 4-chlorophenol. However, upon intercalation of chlorobenzene the new phase attributed to chlorobenzene occurs at lower two theta values. The increase in interlayer space upon intercalation of 4-chlorophenol and phenol are consistent with the size of the respective molecules. Chlorobenzene does not show an interlayer space that is consistent with the size of the molecule. This suggests that its binding in the ZrP-DHDA is different from 4-chlorophenol and phenol. We reported in section 4.3.1 that the DHDA molecules in ZrP-DHDA are such that there are unreacted phosphate groups due to the covering effect. We propose that the hydroxyl groups on phenol and chlorophenol can

interact with the phosphate groups of the layers in ZrP through possible hydrogen bonding interactions. The absence of the hydroxyl groups in chlorobenzene suggest that this hydrogen bonding interaction may not be possible with chlorobenzene.

5.3.5 ATR-FTIR analysis

In section 5.3.4, the intercalation of chlorophenol was described as co-intercalation based on the XRD patterns. Co-intercalation of chlorophenol and DHDA in ZrP is confirmed by infrared spectroscopy. Fig.5.18 shows the ATR-FTIR spectra of ZrP-DHDA and 4-chlorophenol intercalated ZrP-DHDA.

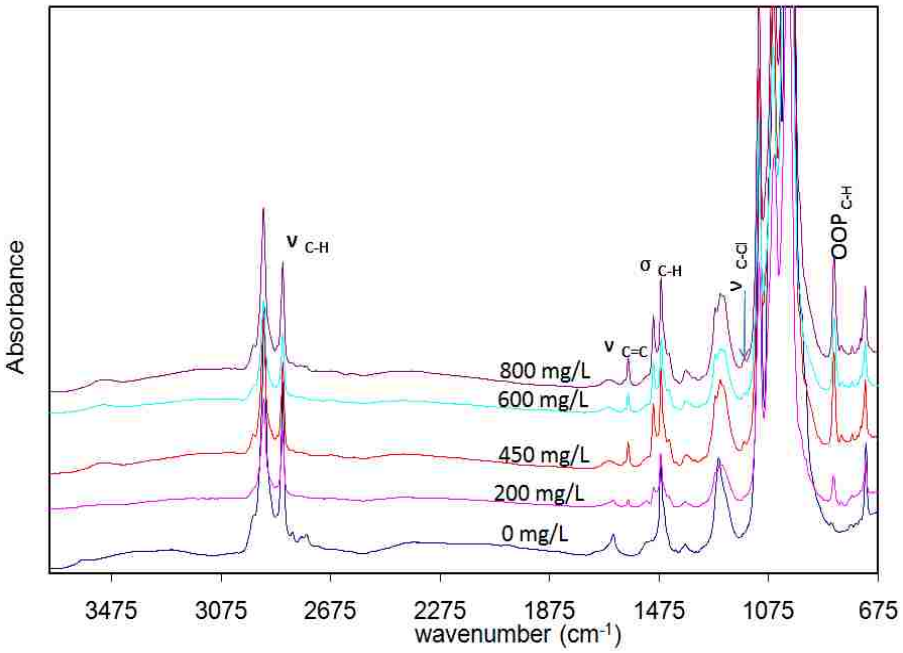

Figure 5.18 ATR-FTIR spectra of phases obtained after adsorption of 4-chlorophenol by 0.1 g of ZrP-DHDA in 30 ml of solution at different 4-chlorophenol concentrations. The co-intercalation of DHDA and chlorophenol is represented by IR bands of both molecules in the products.

Absorption bands due to 4-chlorophenol at 1590 cm^{-1} and 1497 cm^{-1} are assigned to ν C=C ring stretching frequency. The band at 1090 cm^{-1} is assigned to ν C-Cl

stretching frequency and the band at 823 cm^{-1} is assigned to the out of plane bending mode of the ring C-H vibration.[149,150] Fig.5.18 clearly shows that the infrared bands of the parent material are still present after the intercalation of 4-chlorophenol. This confirms that the DHDA and 4-chlorophenol are co intercalated.

5.3.6 Regeneration of ZrP-DHDA

One of the desirable characteristics of an adsorbent is its ability to be used more than once. The negative temperature dependence of the adsorption process suggests that this process involves weak interactions which can be easily reversed. ZrP-DHDA was regenerated by exposing the layered material with chlorophenol in distilled water at 40 ^{0}C. XRD patterns of solid materials contacted in water at different times are shown in Fig.5.19

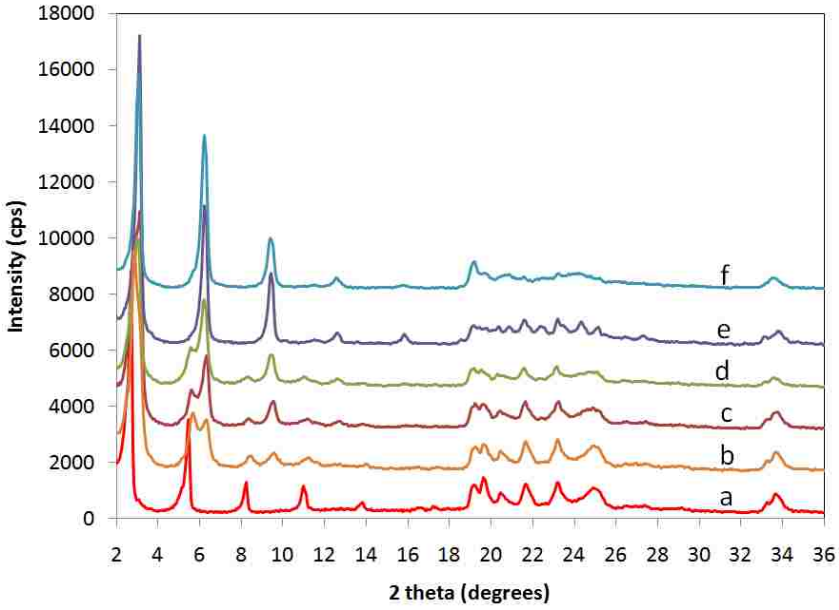

Figure 5.19 XRD patterns of ZrP-DHDA intercalated with 4-chlorophenol after exposing to water for 0 minutes(a), 2 hrs (b), 4 hrs (b), 8 hrs (c) 10 hrs (d) 12 hrs (e) 16 hrs (f).

5.3.7 Conclusions

The affinity of ZrP for 4-chlorophenol was improved by intercalation of dimethylhexadecylamine. ZrP-DHDA can be effectively used for the removal of 4-chlorophenol from aqueous solutions. The removal of 4-chlorophenol from aqueous solution is induced by partitioning of the 4-chlorophenol into the ZrP-DHDA solid as observed from the S type isotherms. Chlorophenol was co-intercalated reversibly in the ZrP-DHDA interlayer space. The amount of chlorophenol adsorbed decreased with increasing temperature. This indicates weak interactions between the adsorbent and the chlorophenol. The sorption kinetics showed a rapid first order step followed by a slow or second order step.

The adsorption kinetics of the isomers of chlorophenol suggest that the adsorption process is faster for the para isomer than for the ortho isomer but the maximum adsorption capacity is independent of the chlorophenol isomer.

6 PROPOSED FUTURE WORK

6.1 Chemical Sensor Development

The diffusion coefficients obtained from ATR-FTIR studies have been proposed as parameters for selecting polymer coatings for surface acoustic wave devices in our lab. With the availability of heated ATR cells in our lab, there are opportunities to study the thermodynamics of diffusion processes using ATR-FTIR spectroscopy. This will provide more information on the interactions of polymers with given analytes. With the ATR flow through cell also available in our lab there are opportunities for monitoring the diffusion of quercetin in a polymer coating simultaneously with frequency response of a polymer coated QCM. This interface will allow us to get more information on the response of a given analyte to a given polymer coating.

It was observed that the detection limit of a QCM sensor was increased by using a BPA-HMTS coating synthesized through a hydrosilation reaction. Hydrosilation reactions have been shown to be effective in synthesizing polymer coatings with desired functional groups. This reaction can be used to synthesize more polymers with varying functional groups. The results in this study show how sensitivity can be improved using BPA-HMTS polymer. However the selectivity of the sensor device has not been explored. Selectivity can be achieved by the use of sensor arrays. It is proposed that by different synthesizing polymers based on the hydrosilation reaction, different responses from the polymers can be used to develop an array of sensors.

6.2 Intercalation of chlorophenol in ZrP-DHDA

We have shown from X-ray diffraction analysis and FTIR spectroscopy results that chlorophenol is co-intercalated with dimethylhexadecylamine in the interlayer space of zirconium phosphate. We have not been able to determine the interaction between the co-intercalated chlorophenol and dimethylhexadecylamine with the zirconium phosphate layers. Preliminary computational calculations using model systems representing ZrP and alkylamines have been performed by Ning Wang, a graduate student in our lab. A protonated alkylamine was modeled using an NH_4^+ ion and the $ZrPO_4$ was modeled using a $H_3PO_4^-$. Calculations were performed using Gaussian 03 using DFT level of theory and a B3LYP method with a 6-31 G* basis set. The enthalpy of reaction for forming [$NH4^+$---$-H_3PO_4^-$] complex is -150.6 Kcal. The enthalpy of reaction for the interaction between the alkylamine and phenol was modeled using the complex [$NH4^+$------ OH-C_6H_4- Cl]. The enthalpy of reaction is -31.38 Kcal. These results suggest that it is highly unlikely that the alkylamine-phosphate bond is broken during the intercalation of chlorophenol. We propose that the arrangement of tertiary amines in the layered zirconium phosphate create pockets of space where the chlorophenol sit without disrupting the alkylamine – phosphate interaction. However, more information can be obtained using molecular dynamic simulations which have proven to be very powerful in complementing experiments especially in exploring the thermodynamic information at molecular level.[151]

6.3 Prospects and Challenges for ZrP-DHDA application

ZrP-DHDA produced in this study has excellent affinity for chlorophenol. It can be potentially used for removing chlorophenol and other organic pollutants from aqueous

solution. However, a few challenges remain to be overcome to make this layered material suitable for commercial scale application. One important point is that powdered sorbents give rise to problems like high pressure drops, high diffusion resistance and difficult particle separation.[5,136] Problems of separation may be solved by palletizing the layered materials and packing the pallets into a column through which the polluted water is allowed to flow. Studies can be done to determine parameters such as the optimum flow rate and the packing density that will allow optimum removal of the pollutant from the flowing solution.

Another way of solving the problem associated with powder sorbents is making thin films of the layered materials. If these films behave as the bulk powders it means with thin films it will be possible to remove pollutants at very low concentrations. Preliminary results obtained indicate that it is possible to fabricate thin films of layered zirconium phosphate and still have the layered structures that are similar with bulk powder samples. Fig. 6.1 shows the X-ray diffraction of a thin film of ZrP deposited on a glass slide.

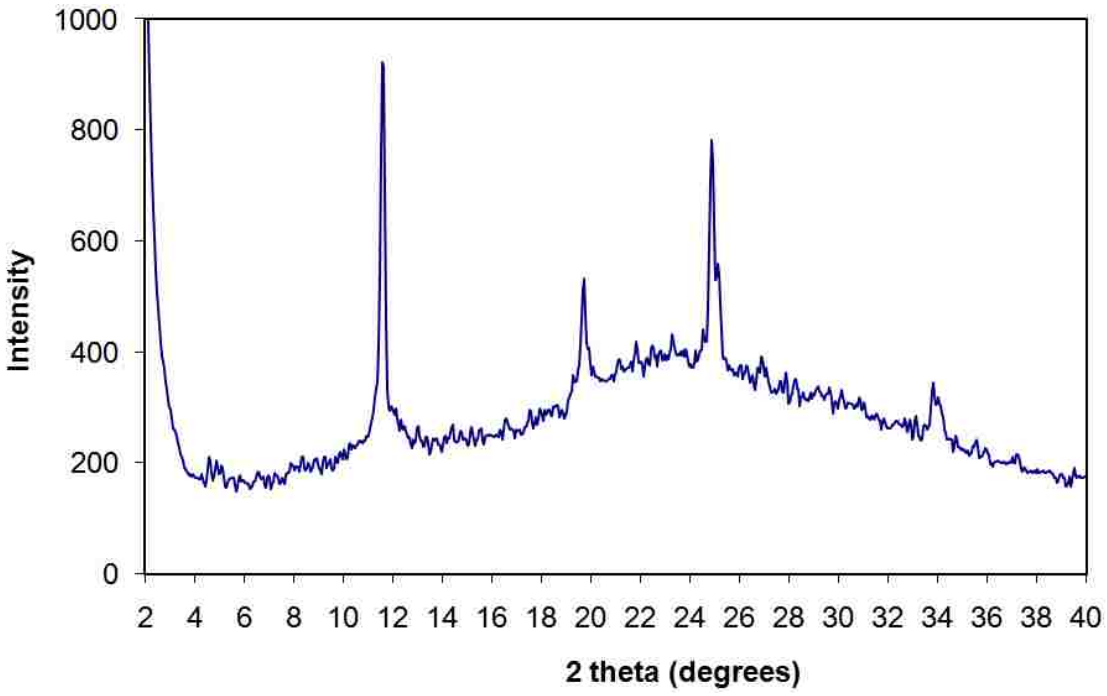

Figure 6.1 X-ray diffraction pattern of a film of ZrP deposited on a glass slide

The broad baseline in Fig.6.1 is due to the glass substrate which has a characteristic peak centered around 24^0 2 theta value. Fig. 6.1 shows that the thin film deposited on the glass slide has a layered structure that is similar to the powder sample. Butylamine was intercalated into layered ZrP coated on a glass slide by suspending a ZrP coated glass slide over a vapor of butylamine. Fig 6.2 shows the X-ray diffraction pattern of a film of ZrP-BA deposited on a glass slide. The XRD pattern for the powder sample is also shown in Fig.6.2.

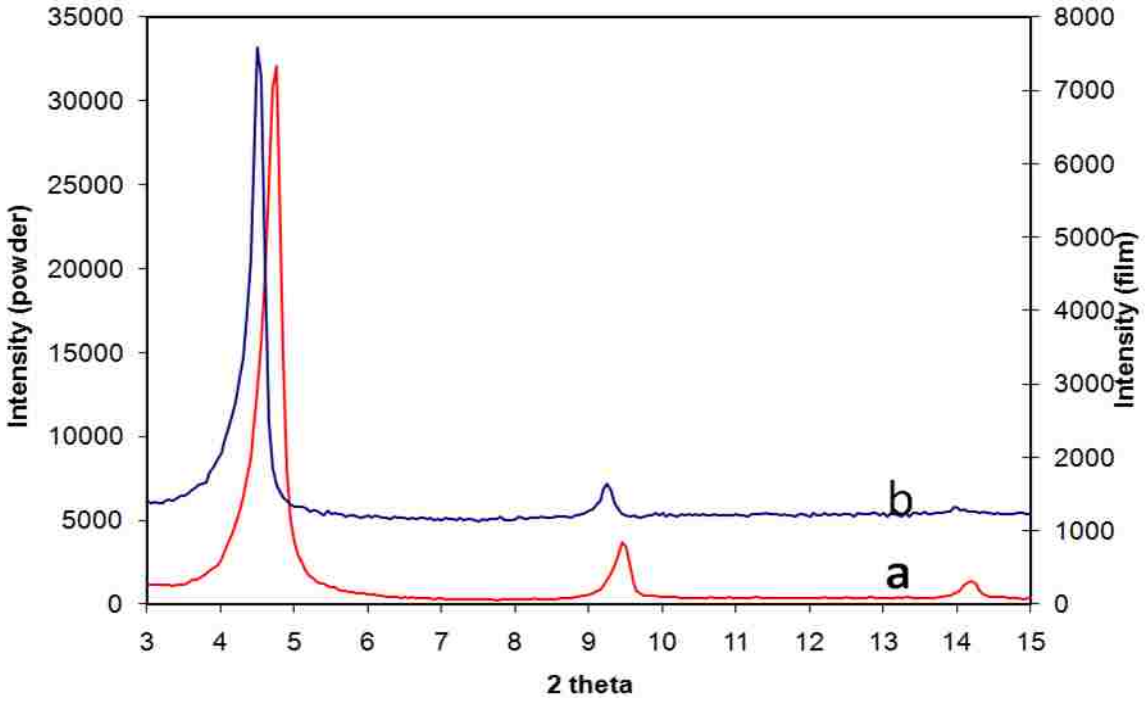

Figure 6.2 X-ray diffraction pattern of ZrP-BA powder (a) film (b) deposited on a glass slide

Attempts to use the film deposited on a glass slide to adsorb chlorophenol were fruitless because the film fell off from the substrate when dipped in solution. An effective way of overcoming this problem is to impregnate the fine powders onto porous sorbents[4]. We propose using polymer films that are stable on glass slides or related substrate and impregnating them with layered zirconium phosphate. We have managed to deposit zirconium phosphate on a glass slide by first dispersing it into polyethyleneimine (PEI), a polymer with amine functional groups that interact with the phosphate groups of the layered zirconium phosphate. Fig.6.3 shows the X-ray diffraction pattern of a film ZrP-PEI film.

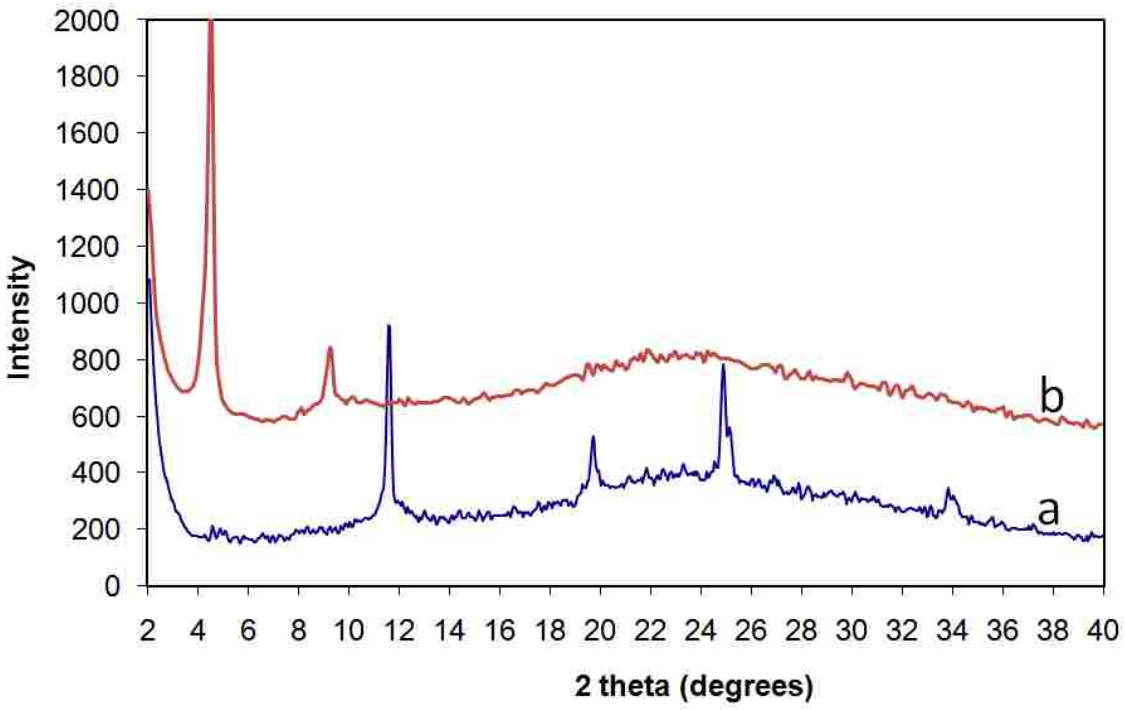

Figure 6.3 X-ray diffraction pattern of ZrP film (a)and ZrP-PEI (b) deposited on a glass slide

The surface morphology of the ZrP-PEI films deposited on glass slide was characterized by atomic force microscopy (AFM). Fig.6.4 shows the AFM image of ZrP-PEI film. The height profile in Fig.6.4b shows that the average height across the distance imaged was 75 nm. Experiments to study the asorption capacity of the film can be carried out by varying the film thicknesses which can be measured using AFM and then studying the effect of film thickness on the amount and kinetics of sorption.

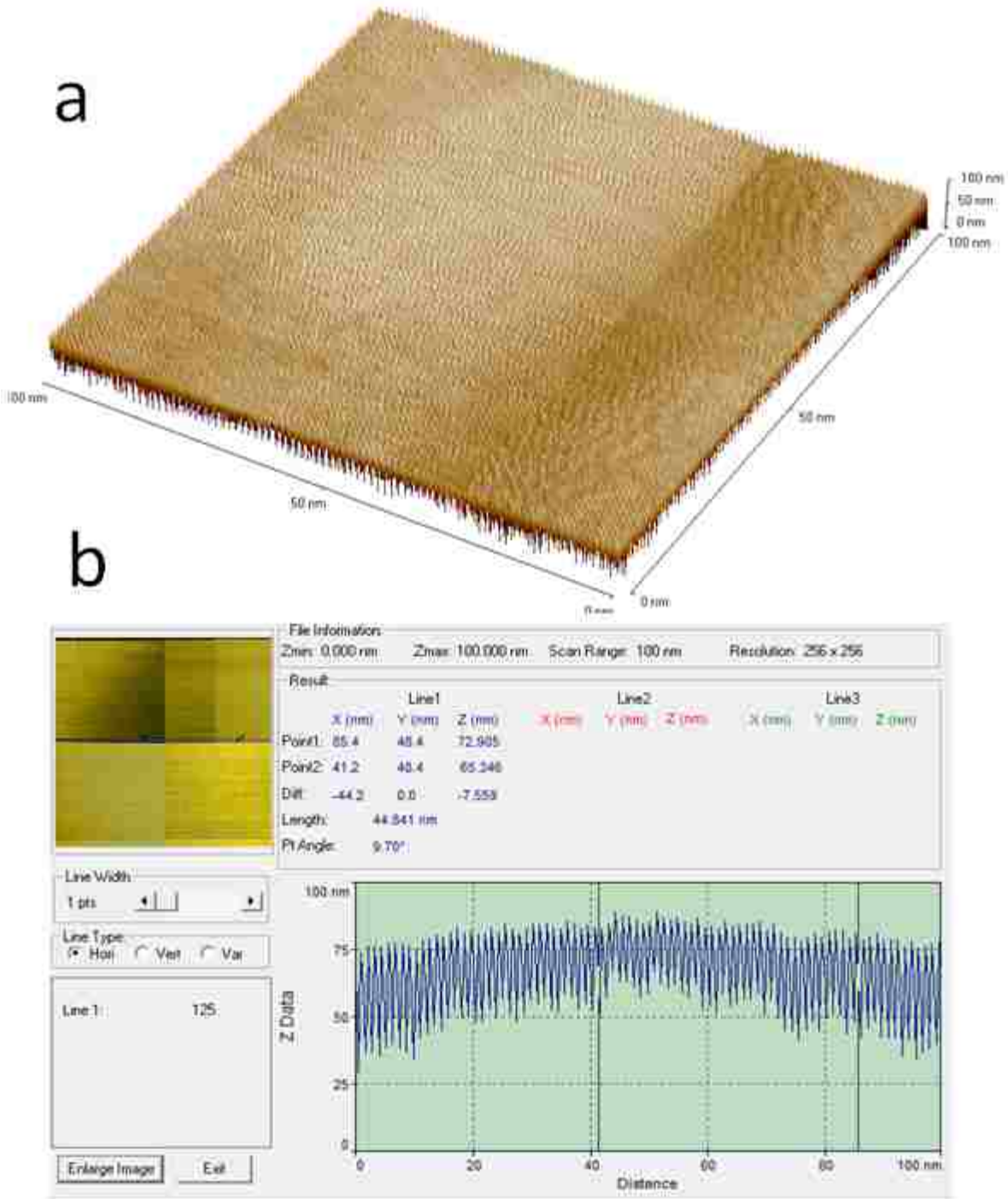

Figure 6.4 Tapping mode AFM image of ZrP-PEI film (a) and height profile of the film (b)

The kinetics of sorption can be studied using thin films and very low concentrations of pollutants. The effect of film thickness can be evaluated using kinetic models as well as diffusion models to determine the mechanism of sorption.

REFERNCES

1. McGill, R. A.; Abraham, H. M.; Grate, J. W. *CHEMTECH* **2009,** *24*, 27-37

2. Xu, X.; Zhang, C.; Zhou, Y. *Journal of Bioactive and Compatible Polymers* **2007,** *22* 195-206.

3. Josse, F.; Bender, F.; Cernosek, R. W. *Anal. Chem.* **2001,** *73*, 5937-5944

4. Jones, Y. K.; Zhonghui Li; Johnson, M. M.; Josse, F.; Hossenlopp, J. M. *IEEE SENSORS JOURNAL* **2005,** *5*, 1175-1184.

5. Goh, K. H.; Lim, T. T.; Dong, Z. *Water Research* **2008,** *42*, 1343-1368

6. Wang, S. L.; Liu, C. H.; Wang, M. K.; Chuang, Y. H.; Chiang, P. N. *Applied Clay Science* **2009,** *43*, 79-85.

7. Lazaridis, N. K.; Asouhidou, D. D. *Water Research* **2003,** *37*, 2875-2882.

8. Zhao, H.; Nagy, K. L. *Journal of Colloid and Interface Science* **2004,** *274*, 613-624.

9. Weber, J. *Physico-Chemical Processes for Water Quality Control*, Wiley Interscience: New York, 1972.

10. Schweiger, T. A. J.; LeVan, M. D. *Ind. Eng. Chem. Res.* **1993,** *32*, 2418-2429.

11. Das, J.; Das, D.; Dash, G. P.; Parida, K. M. *Journal of Colloid and Interface Science* **2002,** *251*, 26-32.

12. Yang, L.; Shahrivari, Z.; Liu, P. K. T.; Sahimi, M.; Tsotsis, T. T. *Ind. Eng. Chem. Res.* **2005,** *44*, 6804-6815.

13. Silbey, R. J.; Alberty, R. A. *Physical Chemistry*, John Wiley&Sons, Inc: New York, 2000

14. Grate, J. W.; Nelson, D. A. *Proceedings of the IEEE* **2003,** *91*, 883-889.

15. Grate, J. W.; Abraham, M. H. *Sens. Actuators. B: Chemical* **1991,** *3*, 85-111.

16. Grate, J. W.; Patrash, S. J.; Abraham, M. H. *Anal. Chem.* **1995,** *67*, 2162-2169.

17. Grate, J. W.; Kaganove, S. N. P. S. J. C. R.; Bliss, M. *Chem. Mater.***1997,** *9*, 1201-1207.

18. Jones, Y. K. Ph D Chemistry Marquette University, 2005.

19. Grate, J. W.; Klusty, M.; McGill, R. A.; Abraham, M. H.; Whiting, G.; Andonian-Haftvan, J. *Anal. Chem.***1992,** *64*, 610-624.

20. Rapp, M.; Reibel, J.; Voigt, A.; Balzer, M.; Bnlow, O. *Sens. Actuators B: Chemical* **2000,** *65*, 169-172.

21. Perez, G. P.; Crooks, R. M. *Anal. Chem.* **2004,** *76*, 4137-4142.

22. Stein, R. S.; Krogh, L. C. *Poymer Science and Engineering: The Shifting Research Frontiers*, National Academy Press: Washington DC, 1994.

23. Sperling, L. H. The Amorphous State, in *Introduction to Physical Polymer Science,* John Wiley & Sons: New York, 2001.

24. Bario, N.; Rapp, M.; Ache, H. J. *Sens. Actuators B: Chemical* **1998,** *46*, 97-103.

25. Hierlemann, A.; Wiemar, U.; Kraus, G.; Gauglitz, G.; Goepel, W. *Sens. Mater.* **1995,** *7* 179-189.

26. Park, J.; Groves, W. A.; Zellers, E. T. *Anal. Chem.* **1999**, *71*, 3877-3886.

27. Grate, J. W.; Kaganove, S. N. *Polymer News* **1999**, *24*, 149-155.

28. Grate, J. W.; Kaganove, S. N.; Nelson, D. A. *Chemical Innov.* **2010,** *30*, 29-37.

29. Guilbault, G. G.; Jordan, J. M. *Critical Review in Anal. Chem.* **1998,** *19*, 1-12

30. Drafts, B. *IEEE TRANSACTIONS ON MICROWAVE THEORY AND TECHNIQUES* **2001,** *19*, 795-802.

31. Yi, F. PhD Chemistry West Virginia University, 2003.

32. Martin, S. J.; Frye, G. C.; Senturia, S. D. *Anal. Chem.* **2002,** *66*, 2201-2219

33. Mirmohseni, A.; Hassanzadeh; V *J. Appl. Polym. Sci.* **2001,** *79*, 1062-1066.

34. Jarrett, M. R.; Finklea, H. O. *Anal. Chem.***1998,** *71*, 353-357.

35. King, W. H. *Anal. Chem.* **1964,** *36*, 1735-1739.

36. Laot, C. M. PhD Viginia Polytechnic Institute and State University, 1997.

37. Laot, C.; .M Master of Science in Chemical Engineering Virginia Polytechnic Institute and State University, 1997.

38. Schuttlefield, J.; Al-Hosney, A.; Zacharia, A.; Grassian, V. H. *Appl. Spectr.***2006,** *61*, 283.
39. Grate, J. W.; McGill, R. A. *Anal. Chem.* **1995,** *67*, 4015-4019.

40. Fieldson, G.; Barbari , T. A. *AIChE.* **1995,** *41*, 795-804.

41. Elabd, Y. A.; Sloan, J. M.; Tan, N. B.; Barbari, T. A. *Macromolecules* **2001,** *34*, 6268-6273.

42. Demirbas, E.; Kobya, M.; Senturk, E.; Ozkan, T. *Water SA.* **2004,** *30*, 533-540.

43. Aksu, Z.; Kabasakal, E. *Separation and Purification Technology* **2004,** *35*(3), 223-240.

44. Bruschini, C. S.; Hudson, M. J. *Progress in Ion Exchange Special Publication-Royal Chemical Society* **1997,** *196* 403.

45. Houghton, J. L.; Quarmby, J. *Current Opinion in Biotechnology* **1999,** *10* 259-262.

46. Khan, A. R.; Al Bahri, T. A.; Al Haddad, A. *Water Research* **1997,** *31*, 2102-2112.

47. Hameed, B. H.; El Khaiary, M. I. *Journal of Hazardous Materials* **2008,** *157*, 344-351.

48. Alekseeva, S.; Bolotin, S.; Tsyupko, T. *Russian Journal of Applied Chemistry* **2007,** *80*, 376-378.

49. Lazaridis, N. K.; Keenan, H. *Journal of Hazardous Materials* **2010,** *173*, 144-150.

50. Chen, D. Z.; Zhang, J. X.; Chen, J. M. *Int. J .Environ. Sci. Tech*. **2010,** *7*, 235-242

51. Oh, J. M.; Biswick, T. T.; Choy, J. H. *J. Mater. Chem.***2009,** *19*, 2553-2563.

52. Majoni, S.; Su, S.; Hossenlopp, J. M. *Polym. Degrad. Stability* **2010,** *95*, 1593-1604.

53. Jimenez-Jimenez, J.; Maireles-Torres, P.; Olivera-Pastor, P.; Rodriguez-Castellon, E.; Jimenez-Lopez, A. *Langmuir* **1997,** *13*(10), 2857-2862.

54. Rozic, M.; Cerjan-Stefanovic, S.; Kurajica, S.; Vancina, V.; Hodzic, E. *Water Research* **2000,** *34,* 3675-3681

55. Chao, Y. F.; Lee, J. J.; Wang, S. L. *Journal of Hazardous Materials* **2009,** *165,* 846-852.

56. You, Y. W.; Zhao, H. T.; Vance, G. F. *Environ. Tech.* **2001,** *22*(12), 1447-1457

57. Chuang, Y. A.; Tzhou, Y. M.; Wang, M. K.; Lieu, C. H.; Chiang, N. P. *Ind.Eng.Chem.Res.* **2008,** *47* 3813-381

58. Jaynes, W. F.; Boyd, S. A. *Soil Sci. Soc. Amer.* **1991,** *55,* 43-48.

59. Lee, S. H.; Song, D. I.; Jeon, Y. W. *Environ. Tech.* **2001,** *22,* 247-254.

60. Clearfield, A.; Tindwa, R. M. *J. Inorg. Nucl. Chem.***1979,** *41* 871-878

61. Clearfield, A.; Kullberg, L.; Oskarsson, A. *The Journal of Physical Chemistry* **1974,** *78,* 1150-1153

62. Naima Bestaoui, N. A. S. A. C. *Mater. Chem.***2006,** *16,* 759-764.

63. Kumar, C. V.; Raju, B. B. *Molecular and Supramolecular Photochemistry,* Marcel Dekker, Inc: New York, 2001

64. Clearfield, A.; Tindwa, R. M. *J. Inorg. Nucl. Chem.***1979,** *41,* 871-878

65. MacLachlan, D. J.; Morgan, K. R. *J. Phys. Chem.* **1990,** *94,* 7656-7661.

66. MacLachlan, D. J.; Morgan, K. R. *J. Phys. Chem.***1992,** *96,* 3458-3464

67. Rodriguez, M. L.; Suarez, M.; Garcia, J. R.; Rodriguez, J. *Solid State Ionics* **1993,** *63-65,* 488-493.

68. Clearfield, A.; Costantino, U. *Comprehensive Supramolecular Chemistry*; Elsevier Science Inc: New York, 1996.

69. Hayashi A; Nakayama, H.; Tsuhako, M. *Bull. Chem. Soc. Jpn.* **2003,** *76* 2315-2319.

70. Rice-Evans, C. A.; Miller, N. J.; Paganga, G. *Free Rad. Bio. Med*. **1996,** *20* 933-956.

71. Moore, W. J. Crystallography, *Basic Physical Chemistry*, Pentice-Hall, Inc: New Jersey, 1983.

72. Hediger, S.; Meier, B. H.; Kurur, N. D.; Bodenhausen, G.; Ernst, R. R. *Chem.Phys. Letter.***1994,** *223,* 283-288.

73. Koes, R.; Verweii, W.; Quattrochio, F. *Trends in Plant Science* **2005,** *10,* 236-242.

74. Cheynier, V. *Am. J. Clin. Nutr* **1994,** *81,* 223S-229S.

75. Scalbert, A.; Williamson, G. *J. Nutr*. **2000,** *130,* 2073S-2085S.

76. Swaroop, A.; Gupta, A.; Sinha, A. *Chromatographia* **2005,** *62,* 649-652.

77. Hertog, M. G.; Kromhout, D.; Aravanis, C.; Blackburn, H.; Buzina, R.; Fidanza, F.; Giampaoli, S.; Jansen, A.; Menotti, A.; Nedeljkovic, S. *Arch. Intern. Med.* **1995,** *155,* 381-386.

78. Formica, J. V.; Regelson, W. *Chem. Toxicol.* **1995,** *33,* 1061-1080.

79. Korkina, L. G.; Afanas'ev, I. B. *Advances in Pharmacology;* Academic Press Inc: New York, 1997.

80. Tambola, A. K.; de Souza, C. D.; Giacomelli, C.; Spinelli, A. *J Braz. Chem. Soc.* **2006,** *17,* 139-146

81. Kanakis, C. D.; Tarantilis, P. A.; Polissiou, M. G.; Diamantoglou, S.; Tajima-Rihai, H. A. *J. Biom. Structure & Dynamics* **2005,** *22,* 719-729.

82. Mishra, B.; Barik, A.; Indira-Priyadarsini, K.; Mohan, H. *J. Chem. Sci.* **2005,** *117,* 641-647.

83. Zandd, R. S. R.; Jenkins, D. J. A.; Diamandis, E. P. *J. Chrom. B* **2002,** *777,* 219-232.

84. Cao, G.; Sofic, E.; Prior, R. *Free Rad. Bio. Med.* **1997,** *22* 749-760.

85. van Acker, S. A.; de Groot, M. J.; van den Berg, D. J.; Tromp, N. M.; Donne-Op den Kelder, G.; van der Vijgh, W. J.; Bast , A. *Chem. Res. Toxicol.* **1996,** *9,* 1305-1312.

86. Arhene, S. A.; O'Brien, N. M. *Nutr. Cancer* **1999,** *34,* 160-166.

87. Horakova, K.; Sovcikova, A.; Seemannova, Z.; Syrova, D.; Busanyova, K.; Drobna, Z.; Ferencik, M. *Free Rad. Bio. Med.* **2001,** *30,* 650-664.

88. Hanasaki, Y.; Ogawa, S.; Fukui, S. *Free Rad. Bio. Med.* **1994,** *16,* 845-850.

89. Tournaire, C.; Croux, S.; Maurette, M. T.; Beck, I.; Hocquaux, M.; Braun, A. M.; Oliveros, E. J. *Photochem. Photobio. B* **1993,** *19,* 205-215.

90. Choi, J. S.; Chung, H. Y.; Kang, S. S.; Jung, M. J.; Kim, J. W.; No, J. K.; Jung, H. A. *Phytother. Res.* **2002,** *16,* 232-235.

91. Yamamoto, N.; Moon, J. H.; Tsushida, T.; Nagao, A.; Terao, J. *Arch. Biochem. Biophys.* **1999,** *372,* 347-354.

92. Van de Woude, P. MSc Wageningen University, 2006.

93. Nishigori, C.; Hattori, Y.; Toyokuni, S. *Antioxid Redox Signal* **2004,** *6,* 570.

94. Storz, P. *Front Biosci* **2005,** *10,* 1881-1896.

95. Pietta, P.; Mauri, P. *Methods in Enzymology Flavonoids and Other Polyphenols,* Academic Press: 2001.

96. Lunte, S. M.; Blankenship, K. D.; Read, S. A. *Analyst* **1988,** *113,* 99-102.

97. Rice-Evans, C. A.; Parker, L. *Flavonoids in Health and Diseases;* Marcel Dekker, Inc: New York, Basel, HongKong, 1988.

98. Lin, X. Q.; He, J. B.; Zha, Z. G. *Sens. Actuators B: Chemical* **2006,** *119,* 608-614.

99. Nuengchamnong, N.; Hermans-Lokkerbol, A.; Ingkaninan, K. *Naresuan University Journal* **2004,** *12,* 25-37.

100. Dickert, F. L.; Schuster, O. *Microchimica Acta* **1995,** *119,* 55-62.

101. Lopez-Avila, V.; Hill, H. H. *Anal. Chem.* **1997,** *69,* 289-306.

102. Sauerbrey, G. Z. *Phys. Verh* **1959,** *155,* 206-222.

103. Cornard, J. P.; Merlin, J. C.; Boudet, A. C.; Vrielynck, L. *Biosepectroscopy* **1997,** *3,* 183-189.

104. Solimani, R. *Biochimical et Biophysica Acta* **1997,** *1336,* 281-294.

105. Sideridou, I. D.; Papanastasiou, G. E. *J. Appl. Polym. Sci.* **2009,** *107,* 1047-1056.

106. Popov, V. Y.; Lavrent'ev, V. V. *J. Appl. Spectr.* **1980,** *32,* 193-198.

107. Xu, J. R.; Balik, C. M. *Appl. Spectr.* **1988,** *42,* 1543-1548.

108. Xu, J. R.; Balik, C. M. *J. Appl. Polym. Sci.* **1989,** *38,* 173-183.

109. Hong, S. U.; Barbari, T. A.; Sloan, J. M. *J. Polym. Sci. Part B: Polym. Phys.* **1998,** *36,* 337-344.

110. Sammon, C.; Yarwood, J.; Everall, N. *Polymer* **2000,** *41,* 2521-2534.

111. Barbari A.T; Elabd, A. Y. *AIChE.* **2001,** *47,* 1255-1262.

112. Sideridou, I. D.; Papanastasiou, G. E. *J.Appl. Polym. Sci.* **2009,** *107,* 1047-1056.

113. Fieldson, G.; Barbari, T. A. *Polymer* **1993,** *34,* 1146-1153.

114. Mensah-Brown, A. K.; Mlambo, D.; Josse, F.; Hossenlopp, J. M. *Proc. IEEE:* **2010**, 232-237.

115. Clearfield, A.; Smith, G. D. *Inorg. Chem.* **1969,** *8,* 431-436.

116. Alberti, G.; Costantino, U. *Intercalation Chemistry,* Academic Press Inc: New York, 1982.

117. Troup, J. M.; Clearfield, A. *Inorg. Chem.* **1977,** *16,* 3311-3314.

118. Yamanaka, S.; Horibe, Y.; Tanaka, M. *J. Inorg. Nucl. Chem.* **1976,** *38,* 323-326.

119. Bestaoui, N.; Spurr, N. A.; Clearfield, A. *J. Mater. Chem.* **2006,** *16,*759-764

120. Menedez, F.; Espina, A.; Trobajo, C.; Rodriguez, J. *Mater. Res. Bull.* **1990,** *25* 1531.

121. Benes, L.; Melanova, K.; Svoboda, J.; Zima, V.; Kincl, M. *Journal of Physics and Chemistry of Solids* **2005,** *68,* 803-807.

122. M. J. Frisch, G. W. Trucks, H. B. Schlegel, G. E. Scuseria, M. A. Robb, J. R. Cheeseman, V. G. Zakrzewski, J. A. Montgomery, Jr., R. E. Stratmann, J. C. Burant, S. Dapprich, J. M. Millam, A. D. Daniels, K. N. Kudin, M. C. Strain, O. Farkas, J. Tomasi, V. Barone, M. Cossi, R. Cammi, B. Mennucci, C. Pomelli, C. Adamo, S. Clifford, J. Ochterski, G. A. Petersson, P. Y. Ayala, Q. Cui, K. Morokuma, N. Rega, P. Salvador, J. J. Dannenberg, D. K. Malick, A. D. Rabuck, K. Raghavachari, J. B. Foresman, J. Cioslowski, J. V. Ortiz, A. G. Baboul, B. B. Stefanov, G. Liu, A. Liashenko, P. Piskorz, I. Komaromi, R. Gomperts, R. L. Martin, D. J. Fox, T. Keith, M. A. Al-Laham, C. Y. Peng, A. Nanayakkara, M. Challacombe, P. M. W. Gill, B. Johnson, W. Chen, M. W. Wong, J. L. Andres, C. Gonzalez, M. Head-Gordon, E. S. Replogle, and J. A. Pople, Gaussian, Inc., Pittsburgh PA, 2003

123. Valvani, S. C.; Yalkowsky, S. H.; Amidon, G. L. *The Journal of Physical Chemistry* **1976,** *80*, 829-835.

124. Clayden, N. J. *J. Chem. Soc., Dalton Trans.* **1987**, 1877-1881.

125. Dines, M. B.; Cooksey, R. E.; Griffith, P. C.; Lane, R. H. *Inorg. Chem.* **1983,** *22*, 1003-1004.

126. Tan, I. A. W.; Ahmad, A. L. H. B. H. *Journal of Hazardous Materials* **2009,** *164*, 473-482.

127. Hollender, J.; Zimmermann, S. G.; Koepke, S.; Krauss, M.; McArdell, C. S.; Ort, C.; Singer, H.; von Gunten, U.; Siegrist, H. *Environ. Sci. Tech.* **2009,** *43*, 7862-7869.

128. Koper, B. O.; Rajagopalan, S.; Winecki, S.; Klabunde, K. J. *Environmental Applications of Nanomaterials : Synthesis, Sorbents and Sensors*; Imperial College Press: London, 2007

129. Alhamed, Y. A. *Journal of Hazardous Materials* **2009,** *170*, 763-770.

130. Cabal, B.; Ania, C. O.; Parra, J. B.; Pis, J. J. *Chemosphere* **2009,** *76*, 433-438.

131. Gonzalez Martin, M. L.; Valenzuela Calahorro, C.; Gomez Serrano, V. *Langmuir* **1991,** *7*, 1296-1298.

132. Hsu, Y. H.; Wang, M. K.; Wang, Y. S.; Pai, C. W. *Applied Clay Science* **2000,** *16*,147-159.

133. Seki, Y.; Yurdakoç, K. *J. Colloid and Interface Science* **2005,** *287*, 1-5.

134. Klumpp, E.; Ortegac, C. C.; Klahrea, P.; Tinoa, F. J.; Yapard, S.; Prtilloc, C.; Stegenc, S.; Queiroloc, F.; Schwuger, M. J. *Colloids Surf. A.* **2004,** *320*, 11.

135. Hsu, Y. H.; Wang, M. K.; Wang, Y. S.; Pai, C. W. *Applied Clay Science* **2000,** *16*, 147-159.

136. Goh, K. H.; Lim, T. T.; Dong, Z. L. *Water Sci. Tech.* **2010,** *61*, 1411-1417.

137. Clearfield, A.; Duax, L. W.; Medina, A. S.; Smith, D.; Thomas, J. R. *J. Phys. Chem.* **1969,** *73*, 3424.

138. Clearfield, A. Zirconium Phosphate, in *Inorganic Ion Exchange Materials*, CRS Press: 1983.

139. Pan, B.; Zhang, Q.; Du, W.; Zhang, W.; Pan, B.; Zhang, Q.; Xu, Z.; Zhang, Q. *Water Research* **2007,** *41*, 3103-3111.

140. Ho, Y. S.; McKay, G. *Process Biochemistry* **1999,** *34* 451-465.

141. Lv, L.; He, J.; Wei, M.; Evans, D. G.; Zhou, Z. *Water Research* **2007,** *41*, 1534-1542.

142. Wilczak, A.; Keinath, T. M. *Water Environ.Res.* **1993,** *65*, 238-244.

143. Giles, C. H.; MacEwan, T. H.; Nakhwa, S. N.; Smith, D. *Journal of the Chemical Society (Resumed)* **1960,** *111*, 3973-3993.

144. Zhao, Z.; Wang, X.; Zhao, C.; Zhu, X.; Du, S. *Journal of Colloid and Interface Science* **2010,** *345*, 154-159

145. Bekbolet, M.; Yenigun, O.; Yueel, I. *Water Air Soil Pollut.* **1999,** *111*, 75.

146. Ebadi, A.; Mohammedzadeh, J. S. S.; Khudiev, A. *Adsorption* **2009,** *15*, 65-73.

147. Riley, K. E.; Murra, J. S.; Politzer, P.; Concha, C. M.; Hobza, P. *Journal of Chemical Theory and Computational Chemistry* **2009,** *5*, 155-163.

148. Fickling, M. M.; Fischer, A.; Mann, B. R.; Packer, J.; Vaughan, J. *J. Amer. Chem. Soc.* **1959,** *81*, 4226-4230.

149. Bardakci, B. *Journal of Arts and Sciences Say›:* **2007,** *7* 13-19.

150. Zierkiewicz, W.; Michalska, D.; Zeegers-Huyskens, T. *The Journal of Physical Chemistry A* **2000,** *104*, 11685-11692.

151. Liu, X.; Lu, X.; Wang, R.; Zhou, H.; Xu, S. *American Mineralogist* **2009,** *94*, 143-150.

152. Zhang, Q.; Jiang, P.; Pan, B.; Zhang, W.; Lv, L. *Ind. Eng. Chem. Res.* **2009,** *48*, 4495-4499.

APPENDICES

APPENDIX A

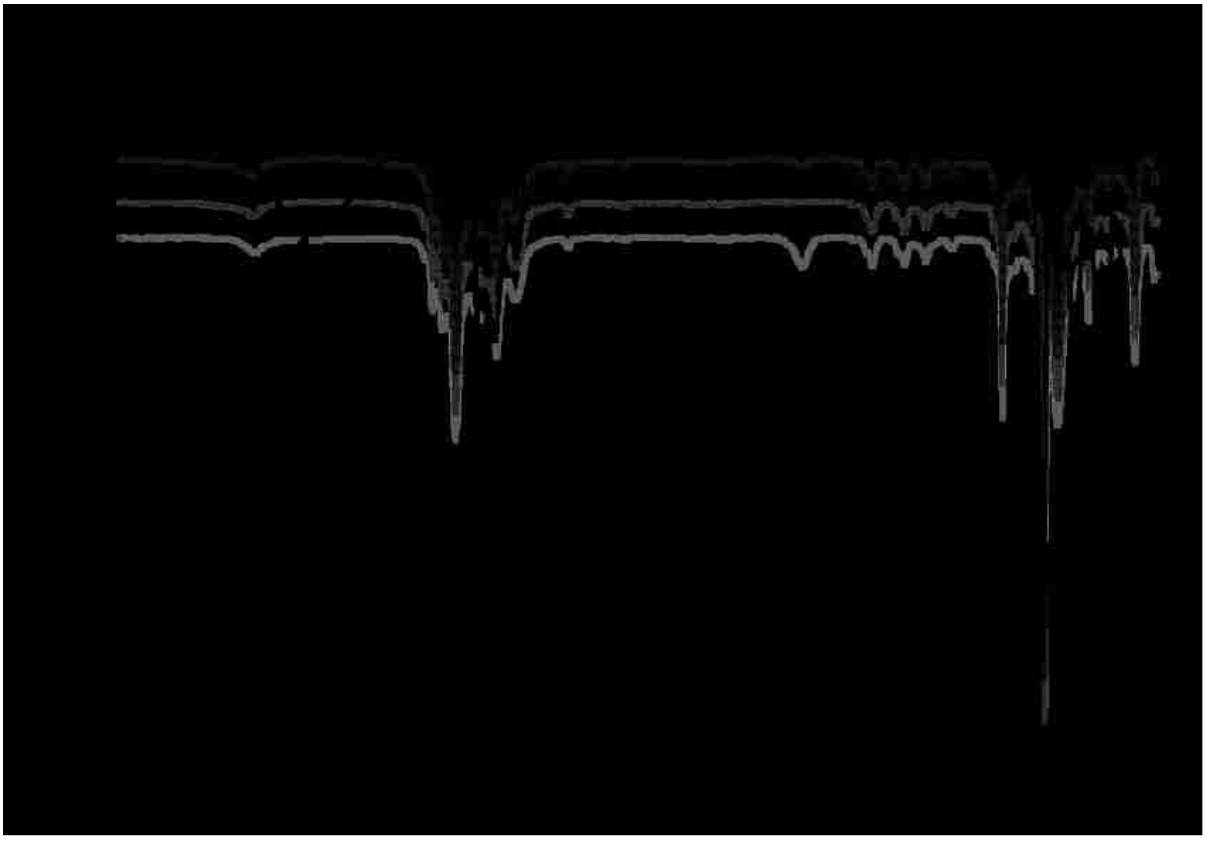

FTIR spectra for the characterization of the functionalization of1,1,3,3,5,5-hexamethyltrisiloxane (HMTS) with 2,2'-diallybisphenol A(BPA) using the hydrosilylation reaction (a) before adding catalyst (b) after adding catalyst and stirring for 20 min (c) after adding excess HMTS and stirring for 20 min (d) final product after evaporation of the solvent

Spectroscopic and physical characteristics of BPA-HMTS.

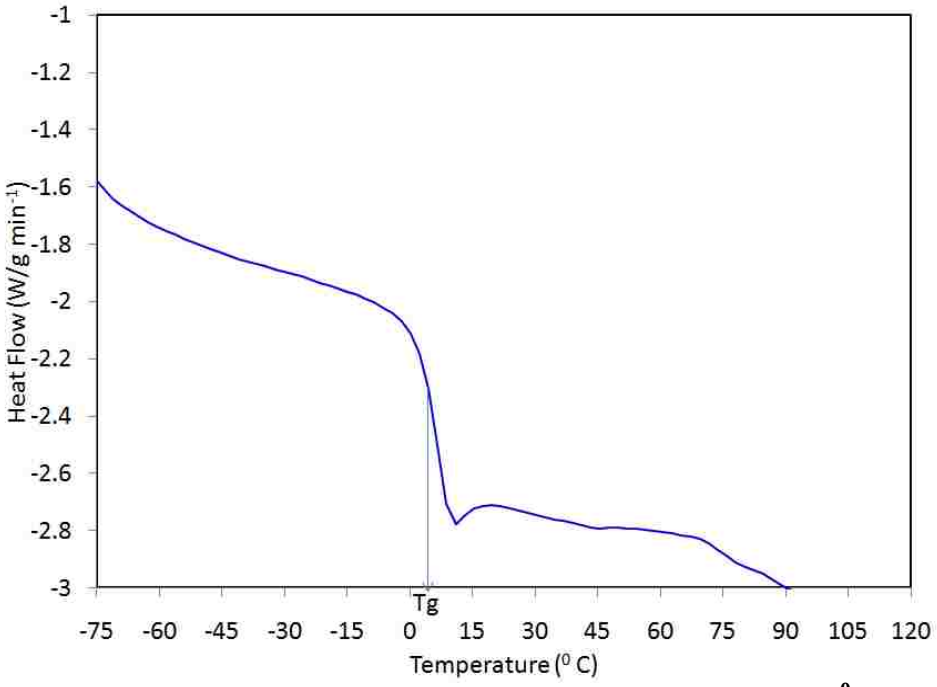

Figure 8.2 DSC trace for BPA-HMTS showing the Tg at 4.95 ^{0} C

The proton and carbon NMR spectra are summarized using peak positions below.

^{1}HNMR (σ 400 MHz, CDCl3) 7.25 (d), 7.08-7,15 (m), 6.69 (m), 5.31 (br), 5.03 (br), 4.6 (s), 3.7 (d), 2.5-2.6 (m), 1.32-1.6 (m), 0.5-0.59 (m), -0.02 – 0.1 (m).

13CNMR (CDCl3) σ 153.8, 133.0, 122.1, 127.9, 128.9, 128.1, 125.6, 124.5.

T_g (DSC) 4.95^{0}C, T_d (TGA) 255^{0}C, ρ 1.15 g/cm^{3}.

T_d is defined as the temperature at which the polymer loses 10 % of its mass under thermal degradation in TGA experiments.

APPENDIX B

Bond lengths of Optimized geometries for quercetin used for calculating IR Frequencies

Bond	B3LYP/6-31	B3LYP/6-31G(d,p)	B3LYP/6-311G(d,p)
O_1-C_2	1.3754	1.3709	1.3698
O_1-C_9	1.3566	1.3863	1.3509
C_9-C_{10}	1.4033	1.4009	1.4127
C_2=C_3	1.3666	1.3643	1.3598
C_3-O_3	1.3546	1.3608	1.3499
O_3-H	0.9771	0.9906	0.9875
C_3-C_4	1.4525	1.447	1.4438
C_4=O	1.2549	1.289	1.2654
C_4-C_{10}	1.4332	1.4299	1.4345
C_{10}=C_5	1.4259	1.411	1.4301
C_5-O_5	1.3398	1.3486	1.3289
O_5-H	0.9831	0.9796	0.9784
C_5-C_6	1.411	1.4078	1.4099
C_6-H	1.0824	1.0803	1.08
C_6=C_7	1.4004	1.3999	1.4008
C_7-O_7	1.3573	1.3509	1.36
O_7-H	0.9643	0.9809	0.9718
C_7-C_8	1.3961	1.3898	1.3901
C_8-H	1.0845	1.1	1.0918
C_8=C_9	1.3904	1.3922	1.3948
C_2-$C_{1`}$	1.4639	1.4807	1.4609
$C_{1`}$-$C_{2`}$	1.4086	1.4011	1.4093
$C_{2`}$-H	1.0864	1.0902	1.0833
$C_{2`}$=$C_{3`}$	1.3834	1.3894	1.3809
$C_{3`}$-$O_{3`}$	1.3522	1.3643	1.3589
O_3-H	0.9733	0.9709	0.9699
$C_{3`}$-$C_{4`}$	1.4267	1.4241	1.4268
$C_{4`}$-$O_{4`}$	1.3533	1.3508	1.3522
$C_{4`}$=$C_{5`}$	1.3822	1.3801	1.3809
$C_{5`}$-H	1.0824	1.0924	1.0898
$C_{5`}$-$C_{6`}$	1.4124	1.4011	1.4092
$C_{6`}$-H	1.0922	1.0933	1.0948

Table 0.1 Quercetin Calculated Frequencies for Quercetin Using Optimized Geometries given in Table 1

B3LYP/6-31		B3LYP/6-31G(d,p)		B3LYP/6-311G(d,p)	
Frequency	Intensity	Frequency	Intensity	Frequency	Intensity
1150.2037	138.6038	1144.7729	139.6128	1140.2366	257.3384
1180.307	46.6268	1182.1005	185.872	1188.7304	90.9693
1181.5713	196.1983	1182.3103	51.5989	1193.8205	141.021
1199.7203	34.6381	1200.6909	53.0773	1199.6984	23.3498
1222.9535	30.3406	1223.4868	72.7173	1219.236	201.2176
1229.6482	335.8478	1228.8619	303.2465	1226.7007	247.7965
1257.1896	235.0755	1255.2349	124.366	1231.4558	1.162
1276.0702	192.2654	1278.3864	182.7349	1268.3024	110.4177
1297.1561	96.0799	1300.6575	158.7992	1278.7015	36.196
1317.1624	5.1211	1315.9332	10.1184	1308.3929	295.1106
1343.5348	271.2183	1341.6477	216.241	1320.8433	256.8611
1355.5272	85.1323	1354.1581	223.0302	1357.3758	365.0214
1371.3763	16.5066	1370.9329	22.2716	1370.1456	284.6888
1387.1064	79.3049	1393.4967	16.2788	1381.2708	97.3168
1414.1028	182.6397	1416.7354	170.3883	1396.9703	19.581
1454.9771	97.2522	1457.1639	124.4931	1417.9066	18.7536
1486.657	79.6328	1491.1758	76.1466	1453.163	178.7863
1511.8539	86.1917	1503.7987	4.8177	1502.896	25.8927
1517.0467	107.5133	1513.3245	194.4148	1509.5824	207.2374
1548.4215	183.6695	1548.1959	203.2137	1537.6554	28.3164
1560.1433	228.8886	1564.0656	155.8778	1553.95	180.3378
1635.5804	72.1997	1635.6092	35.3791	1629.2744	50.1164
1644.1566	97.8647	1641.675	248.2182	1637.9537	118.1799
1657.1038	348.0153	1656.9631	225.6424	1659.5631	336.4691
1668.4153	213.0156	1669.1575	280.895	1665.0035	311.0404
1672.9194	68.4541	1673.2985	26.745	1676.6861	340.0664
1715.5537	420.0941	1715.3065	423.2355	1702.1916	40.4849
3175.3765	19.2301	3177.2115	18.5348	3152.2414	29.788
3198.0795	405.4814	3203.1251	379.7972	3177.4561	8.6816
3206.4296	14.6838	3207.4805	33.9688	3186.1047	4.3154
3212.9436	0.5033	3212.6404	0.8581	3228.7977	1.6396
3230.3915	1.5803	3233.3127	0.659	3255.6002	3.8664
3238.5443	0.8123	3238.3858	0.9447	3490.047	147.005
3778.7041	89.5581	3770.6047	75.4108	3761.5562	90.8809
3782.528	88.0018	3782.4744	102.9259	3776.1142	49.3333
3822.0285	56.7672	3821.9578	58.6601	3790.7177	53.829
3839.6132	108.2107	3839.2358	109.0156	3812.7353	90.558

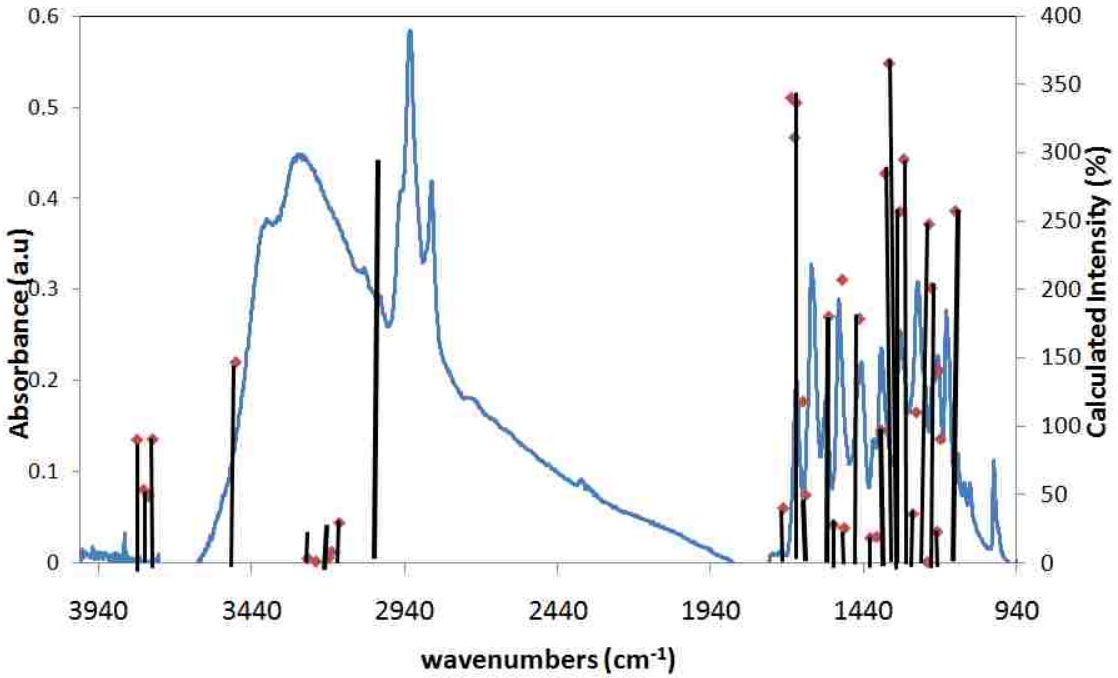

Figure 0.1 Experimental (blue) and calculated (black sticks) spectrum of quercetin. The frequency calculations were carried out using B3LYP/6-31 G* optimized geometry

Optimized geometries of Alkylamines calculated Using B3LYP/6-31G*

Table 0.2 Bond lengths of Dimethylhexadecylamine

N_{15}-C_1	1.4738	C_{12}-H_{13}	1.0929	$C_{22}C_{25}$	1.5299	$C_{34}H_{36}$	1.0918	$C_{46}H_{48}$	1.0919
N_{15}-C_5	1.4738	C_{12}-H_{14}	1.1003	C_{25}-H_{26}	1.0898	C_{34}-C_{37}	1.5421	C_{46}-C_{49}	1.5422
N_{15}-C_9	1.4722	C_{12}-H_{15}	1.1087	C_{25}-H_{27}	1.1091	C_{37}-H_{38}	1.0917	C_{49}-H_{50}	1.0921
C_1-H_2	1.0929	C_{12}-C_{16}	1.5399	C_{25}-C_{28}	1.5384	C_{37}-H_{39}	1.0924	C_{49}-H_{51}	1.0927
C_1-H_3	1.0987	C_{16}-H_{17}	1.0889	C_{28}-H_{29}	1.0931	C_{37}-C_{40}	1.5423	C_{49}-C_{52}	1.5421
C_1-H_4	1.0899	C_{16}-H_{18}	1.0926	C_{28}-H_{30}	1.0911	C_{40}-H_{41}	1.0899	C_{52}-H_{53}	1.0918
C_5-H_6	1.1009	C_{16}-C_{19}	1.5432	C_{28}-C_{31}	1.5471	C_{40}-H_{42}	1.0897	C_{52}-H_{54}	1.0939
C_5-H_7	1.0897	C_{19}-H_{20}	1.0922	C_{31}-H_{32}	1.0921	C_{40}-C_{43}	1.5430	C_{52}-C_{55}	1.5424
C_5-H_8	1.1004	$C_{19}H_{21}$	1.0894	C_{31}-H_{32}	1.0933	C_{43}-H_{44}	1.0917	C_{55}-H_{56}	1.0911
C_9H_{10}	1.0949	C_{19}-C_{22}	1.5386	C_{31}-H_{33}	1.0933	C_{43}-H_{45}	1.0928	C_{55}-H_{57}	1.0914
C_9-H_{11}	1.0924	C_{22}-H_{23}	1.0899	C_{31}-C_{34}	1.5388	C_{43}-C_{46}	1.5423	C_{55}-H_{58}	1.0932
C_9-C_{12}	1.5471	C_{22}-H_{24}	1.1009	C_{34}-H_{35}	1.0922	C_{46}-H_{47}	1.0919		

Table 0.3 Bond Lengths of Dimethyltetradecylamine

N_1-C_2	1.4729	$C_{10}C_{13}$	1.5431	$C_{22}C_{25}$	1.5432	$C_{34}H_{36}$	1.0923	$C_{46}H_{48}$	1.0923
N_1-C_6	1.4729	C_{13}-H_{14}	1.0921	C_{25}-H_{26}	1.0923	C_{34}-C_{37}	1.5429	C_{46}-C_{49}	1.5399
N_1-C_{10}	1.4684	C_{13}-H_{15}	1.0922	C_{25}-H_{27}	1.0919	C_{37}-H_{38}	1.0931	C_{49}-H_{50}	1.0932
C_2-H_3	1.0899	C_{13}-C_{16}	1.5428	C_{25}-C_{28}	1.5412	C_{37}-H_{39}	1.0921	C_{49}-H_{51}	1.0931
C_2-H_4	1.0933	C_{16}-H_{17}	1.0922	C_{28}-H_{29}	1.0924	C_{37}-C_{40}	1.5423	C_{49}-H_{52}	1.5429
C_2-H_5	1.0939	C_{16}-H_{18}	1.0919	C_{28}-H_{30}	1.0923	C_{40}-H_{41}	1.0912		
C_6-H_7	1.0921	C_{16}-C_{19}	1.5428	C_{28}-C_{31}	1.5414	C_{40}-H_{42}	1.0923		
C_6-H_8	1.0924	C_{19}-H_{20}	1.0918	C_{31}-H_{32}	1.0923	C_{40}-C_{43}	1.5423		
C_6-H_9	1.0921	C_{19}-H_{21}	1.0923	C_{31}-H_{32}	1.0921	C_{43}-H_{44}	1.0923		
$C_{10}H_{11}$	1.0919	C_{19}-C_{22}	1.5441	C_{31}-H_{33}	1.0924	C_{43}-H_{45}	1.0928		
C_{10}-H_{12}	1.0899	C_{22}-H_{23}	1.0923	C_{31}-C_{34}	1.5432	C_{43}-C_{46}	1.5438		

Table 0.4 bond lengths of Hexadecylamine

N_1H_{51}	1.0146	C_8-C_{11}	1.0921	$C_{20}H_{22}$	1.5432	$C_{32}H_{33}$	1.0923	$C_{41}C_{44}$	1.0923
N_1-H_{52}	1.0146	$C_{11}H_{12}$	1.0932	C_{20}-C_{23}	1.0923	C_{33}-H_{34}	1.0922	C_{44}-H_{45}	1.0918
N_1-C_2	1.4794	C_{11}-H_{13}	1.0931	C_{23}-H_{24}	1.0921	C_{32}-C_{35}	1.5434	C_{44}-H_{46}	1.0920
C_2-H_3	1.0924	C_{11}-C_{14}	1.5431	C_{23}-H_{25}	1.5432	C_{35}-H_{36}	1.0922	C_{44}-C_{47}	1.5431
C_2-H_4	1.0921	C_{14}-H_{15}	1.0932	C_{23}-C_{26}	1.0924	C_{35}-H_{37}	1.0923	C_{47}-H_{48}	1.0924
C_2-C_5	1.5419	C_{14}-H_{16}	1.0923	C_{26}-H_{27}	1.0919	C_{35}-C_{38}	1.5422	C_{47}-H_{49}	
C_5 -H_6	1.0922	C_{14}-C_{17}	1.5428	C_{26}-H_{28}	1.5428	C_{38}-H_{39}	1.0919	C_{47}-H_{50}	
C_5-H_7	1.0925	C_{17}-H_{18}	1.0925	C_{26}-C_{29}	1.5432	C_{38}-H_{40}	1.0922		
C_5-C_8	1. 5399	C_{17}-H_{19}	1.0922	C_{29}-H_{30}	1.0923	C_{38}-C_{41}	1.5432		
C_8-H_9	1.0918	C_{17}-C_{20}	1.5424	C_{29}-H_{31}	1.0921	C_{41}-H_{42}	1.0922		
C_8-H_{10}	1.0922	C_{20}-H_{21}	1.0919	C_{29}-C_{32}	1.5439	C_{41}-H_{43}	1.0924		

Table 0.5 Bond Lengths of Octylamine

N_1-H_2	1.0144	C_{10}-H_{12}	1.0921	C_{19}-C_{22}	1.5432
N_1-H_3	1.0144	C_{10}-C_{13}	1.5424	C_{22}-H_{23}	1.0919
N_1-C_4	1.4792	C_{13}-H_{14}	1.0919	C_{22}-H_{24}	1.0922
C_4-H_5	1.0923	C_{13}-H_{15}	1.0923	C_{22}-C_{25}	1.5424
C_4-H_6	1.0924	C_{13}-C_{16}	1.5424	C_{25}-H_{26}	1.0920
C_4-C_7	1.5422	C_{16}-H_{17}	1.0924	C_{25}-H_{27}	1.0921
C_7 -H_8	1.0923	C_{16}-H_{18}	1.0918	C_{25}-H_{28}	1.0923
C_7-H_9	1.0923	C_{16}-C_{19}	1.0920		
C_7-C_{10}	1.5414	C_{19}-H_{20}	1.0922		
C_{10}-H_{11}	1.0924	C_{19}-H_{21}	1.0922		

Table 0.6 Bond Lengths of Butylamine

N_1-H_2	1.0146	C_4-C_7	1.5419	C_{10}-H_{12}	1.0922
N_1-H_3	1.0146	C_7-H_8	1.0924	C_{10}-C_{13}	1.5419
N_1-C_4	1.4789	C_7-H_9	1.0922	C_{13}-H_{14}	1.0922
C_4-H_5	1.0922	C_7-C_{10}	1.5414	C_{13}-H_{15}	1.0920
C_4-H_6	1.0920	C_{10}-H_{11}	1.0921	C_{13}-H_{16}	1.0920

APPENDIX C

Table 0.7Experimental and model fitting data for the diffusion of quercetin shown in Fig.3.9

Time(min)	Observed Abs (A_t)	Model (y_o+A*exp(-t/T)	Diff(Calc-Obs)	Diff^2
0	0	-1.2E-05	-1.19754E-05	1.43E-10
4	0.035429	0.035366	-3.37619E-05	1.14E-09
8	0.060795	0.060758	-4.20794E-05	1.77E-09
12	0.079009	0.078982	-0.000117939	1.39E-08
16	0.091484	0.092062	0.000561907	3.16E-07
20	0.101505	0.10145	-5.0414E-05	2.54E-09
30	0.115602	0.114902	-0.000697921	4.87E-07
40	0.120551	0.120773	0.000172803	2.99E-08
60	0.124293	0.124453	0.000152884	2.34E-08
80	0.124834	0.125154	0.00035375	1.25E-07
100	0.124958	0.125287	-0.000512771	2.63E-07
120	0.125	0.125313	0.00021265	4.52E-08

Table 0.8 Experimental and model fitting data for the diffusion of quercetin in PCL shown in Fig. 3.10

t(min)	Observed Abs (A_t)	model (y_o+A*exp(-t/T)	Diff (Obs-model)	Diff^2
0	0	0.010123	0.010123	0.000102
2	0.0139	0.022501	0.008601	7.4E-05
4	0.0382	0.033898	-0.0043	1.85E-05
6	0.0533	0.044392	-0.00891	7.94E-05
8	0.0632	0.054054	-0.00915	8.36E-05
10	0.0706	0.062951	-0.00765	5.85E-05
20	0.0962	0.097915	0.001715	2.94E-06
30	0.1173	0.121055	0.003755	1.41E-05
40	0.1277	0.136371	0.008671	7.52E-05
50	0.1432	0.146507	0.003307	1.09E-05
60	0.1482	0.153216	0.005016	2.52E-05
70	0.1555	0.157656	0.002156	4.65E-06
80	0.1614	0.160595	-0.00081	6.48E-07
90	0.1671	0.16254	-0.00456	2.08E-05
100	0.1718	0.163827	-0.00797	6.36E-05

Table 0.9 Experimental and Model Fitting data for the diffusion of quercetin in PIB shown in Fig.3.11

Time(min)	Observed Abs (A_t)	Model (y_o+A*exp(-t/T)	Diff (Calc-Obs)	Diff^2
0	0	0.0047	0.004678	2.188E-05
4	0.0228	0.0188	-0.00397	1.577E-05
8	0.0320	0.0302	-0.00276	7.594E-06
12	0.0415	0.0394	-0.00205	4.221E-06
16	0.0466	0.0468	0.000259	6.684E-08
20	0.0501	0.0528	0.002105	4.43E-06
40	0.0650	0.0691	0.004158	1.729E-05
60	0.0728	0.0747	0.001962	3.848E-06
80	0.0752	0.0766	0.001429	2.042E-06
100	0.0793	0.0772	-0.00205	4.203E-06
120	0.0794	0.0775	-0.0019	3.626E-06
140	0.0798	0.0775	-0.00185	3.437E-06

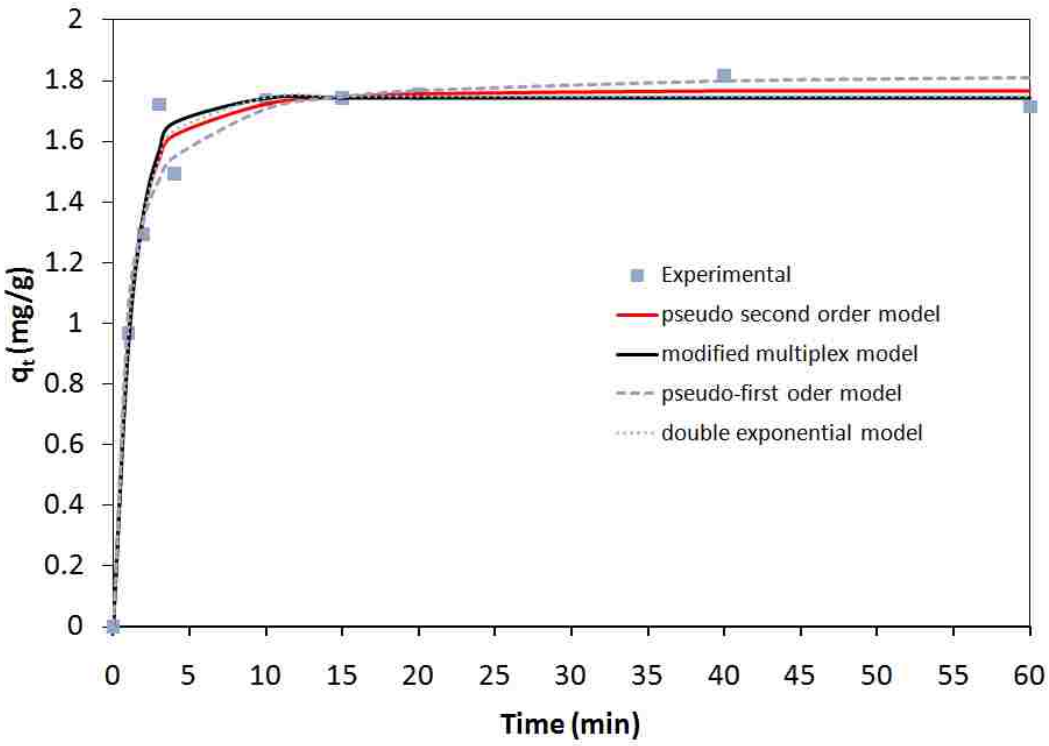

Figure 0.2 Amount of 4-chlorophenol adsorbed by 0.1 g of ZrP-DHDA as afunction of time at 60 ^{0}C. The lines represent the kinetic models used to describe the experimental data

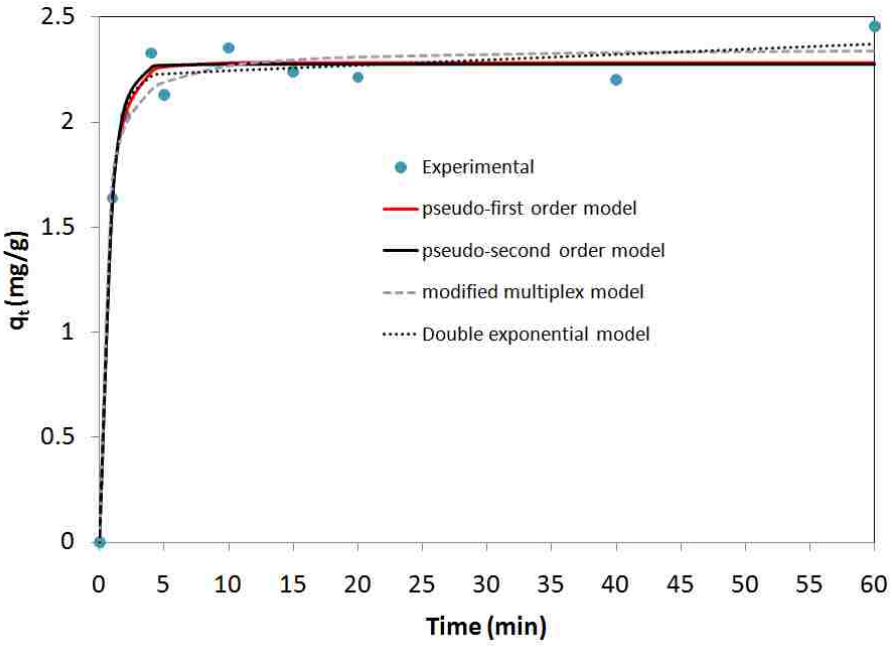

Figure 0.3 Amount of 4-chlorophenol adsorbed by 0.1 g of ZrP-DHDA as a function of time at 50 ^{0}C. The lines represent the kinetic models used to describe the experimental data

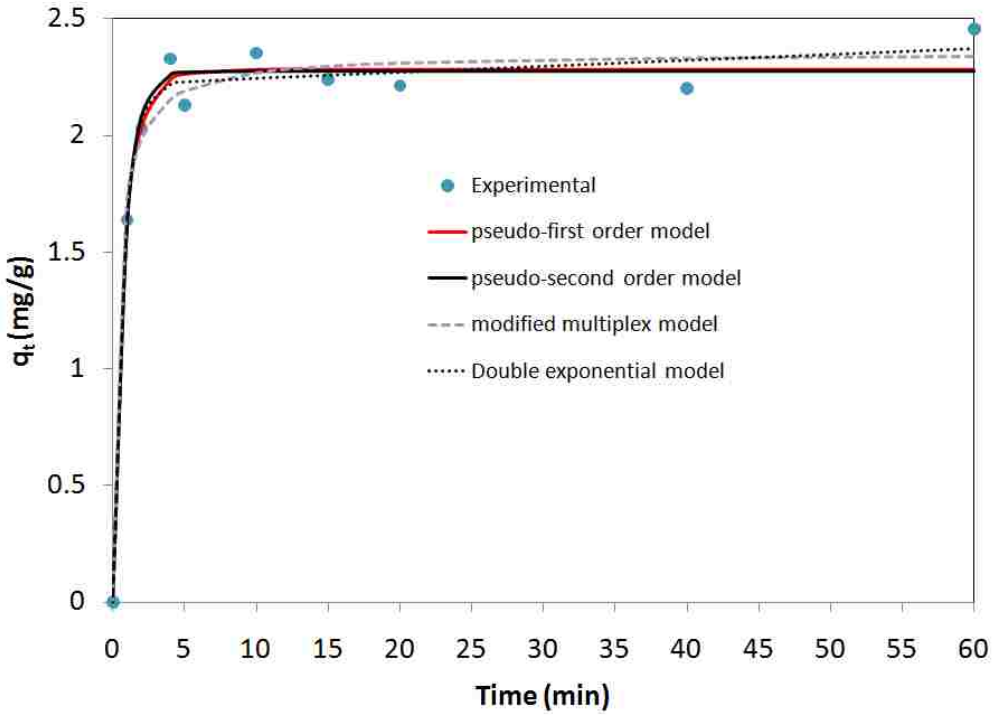

Figure 0.4 Amount of 4-chlorophenol adsorbed by 0.1 g of ZrP-DHDA as a function of time at 40 ^{0}C. The lines represent the kinetic models used to describe the experimental data

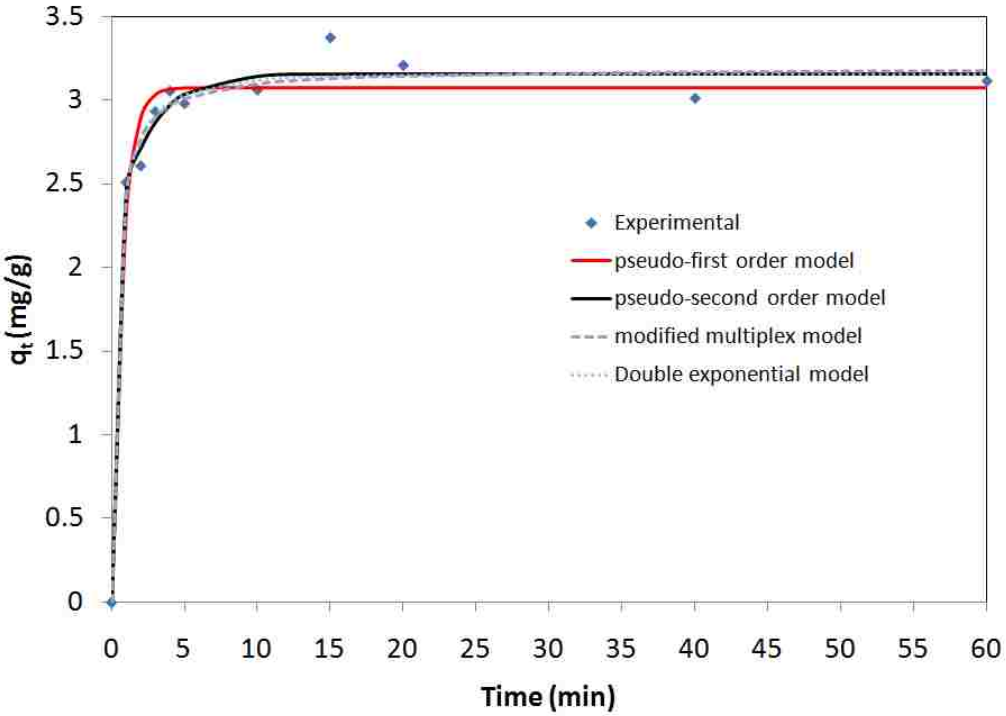

Figure 0.5 Amount of 4-chlorophenol adsorbed by 0.1 g of ZrP-DHDA as a function of time at 27 ^{0}C. The lines represent the kinetic models used to describe the experimental data